INVESTIGATION OF REGENERATIVE AND ALTERNATIVE ENERGY SOURCES FOR ELECTRIFIED PASSENGER VEHICLES

A Thesis

Presented to

The Academic Faculty

By

Carl Thomas Lyles

In Partial Fulfillment

Of the Requirements for the Degree

Master of Science in Mechanical Engineering in the

School of Mechanical Engineering

Georgia Institute of Technology

December 2014

INVESTIGATION OF REGENERATIVE AND ALTERNATIVE ENERGY SOURCES FOR ELECTRIFIED PASSENGER VEHICLES

Approved by:

Dr. Bert Bras, Advisor
School of Mechanical Engineering
Georgia Institute of Technology

Dr. Peter Loutzenhiser
School of Mechanical Engineering
Georgia Institute of Technology

Mr. Joseph Goodman
Research Engineer II
Georgia Tech Research Institute

Date Approved: August 18, 2014

ACKNOWLEDGEMENTS

I would like to express my gratitude to Dr. Bert Bras, whose expertise and direction helped to develop the framework of this thesis, and whose charismatic nature made working on this project a pleasure.

My participation in this project would have not likely been possible without the generous contributions of Ford Motor Company. Thank you to all at Ford who have assisted with this project.

Thanks be to my colleagues Mike Mongeau and Daniel Boston, whose research efforts aided in the development of this thesis.

A special thanks to my parents, Frank and Kathy Lyles. It is your love, support, and guidance that have made me who I am today – a hell of an engineer.

Finally, thank you to all of my friends and family who have been supportive throughout the entirety of this process.

TABLE OF CONTENTS

LIST OF TABLES

LIST OF FIGURES

LIST OF SYMBOLS AND ABBREVIATIONS

α Azimuth of the surface

β - Tilt of the surface

δ - Declination angle

Δt – Change in time

Δx – Change in distance

η – Refraction index

a – Acceleration

A – Amp

AST - Apparent solar time

BEV – Battery electric vehicle

CDF – Cumulative distribution function

CPV – Concentrated photovoltaic

DST - Daylight savings time

E – Energy

ET - Equation of time

F – Force

FS - Finkelstein- Schafer statistic

GHG - Greenhouse gas

H - Hour angle

hr – Hour

HWFET - Highway Fuel Economy Driving Schedule

I – Current

I_D - Direct radiation flux

I_{DN} - Direct normal radiation flux

IR – Infrared

J – Joule

KERS – Kinetic energy recovery system

kg – Kilogram

kWh – Kilowatt hour

LF - Left front

$Long$ - Local longitude

LR – Left rear

LST - Local standard time

$LSTM$ - Local longitude of standard time meridian

m – Mass

m – Meter

mi – Mile

mm – Millimeter

mph - Miles per hour

n - Number of daily readings in a month

N - Day number of the year

$\widehat{N}$ - Surface normal vector

nm – Nanometer

NYCC - New York City Cycle

P – Power

PHEV – Plug-in hybrid electric vehicle

PMMA - Polymethyl methacrylate

PV – Photovoltaic

PV/T - Photovoltaic/thermal

PV/TEG - Photovoltaic/thermoelectric generator

RF – Right front

RR – Right rear

s – Second

$\hat{s}_1$ - Incident ray

$\hat{s}_2$ - Refracted ray

TEG – Thermo-electric generator

TMY – Typical meteorological year

UDDS - Urban Dynamometer Driving Schedule

UV – Ultraviolet

V – Volt

w – Weighting index

W – Work

W – Watt

WS - Weighted sum

v – Velocity

V – Voltage

SUMMARY

The electrification of passenger vehicles has been a step towards the reduction of greenhouse gas emissions by automobiles; however, in the United States many plug-in hybrid electric vehicles (PHEVs) and battery electric vehicles (BEVs) must still be plugged in to a grid that is heavily reliant on the burning of fossil fuels to charge. The goal of this thesis is to investigate how to develop a system capable of fully charging a PHEV using only alternative and/or regenerative energy sources.

In developing such a system, various alternative and regenerative energy sources were investigated with the intent of reaching a specified daily energy goal; sufficient to charge a PHEV. These energy sources were evaluated based upon criteria such as novelty, ability to reach desired daily energy goal, applicability to BEV/PHEV, etc. The primary technological categories considered include but are not limited to regenerative and solar technologies. The evaluation of technologies indicated that a major opportunity lies in solar technologies, and in particular concentrated photovoltaics.

Design alternatives for a concentrated photovoltaic system capable of reaching the desired energy goal are described. The design alternatives utilize Fresnel lenses as a means of concentrating a large area of sunlight onto an array of photovoltaics affixed to a vehicle. Various tracking mechanisms for the concentrating systems have been outlined to meet given design criteria. 3-D ray tracing algorithms have been developed to determine the path of the tracking mechanisms depending upon the time of year and on the geographic location. The same algorithms have been used in conjunction with typical meteorological year data to determine the expected output of the concentrating systems based upon the solar resource and solar angles at a specific place and time.

The findings suggest that a concentrated photovoltaic system designed specifically for charging an electrified vehicle may generate sufficient energy over the course of a day to power a typical driver’s trips. However, for such a concentrating system to be commercially feasible there are still many design challenges to be overcome. Design limitations and implications for further research are discussed.

CHAPTER 1: INTRODUCTION

There currently exists a broad range of electrified passenger vehicles, however the focus of this paper will be on plug-in hybrid electric vehicles (PHEVs) and battery electric vehicles (BEVs). A PHEV is an electrified vehicle which contains both a conventional internal combustion engine and an electric motor. The electric motor of a PHEV is powered by a battery which can be charged by, amongst other means, plugging into a conventional power outlet. The PHEV which will be used in the analyses conducted in this paper is the Ford C-MAX Energi, depicted in Figure 1. For conciseness, the Ford C-MAX Energi will be referred to as the C-MAX for the duration of the paper. As shown in the figure, the C-MAX has a plug which can be used to charge the electric motor's 7.6 kWh propulsion battery. A BEV is similar to a PHEV in that it can be plugged in to charge; however, unlike the PHEV, a BEV does not contain a conventional internal combustion engine. A BEV's only means of propulsion is an electric motor, which is powered by a propulsion battery: typically of larger capacity than that of a PHEV.

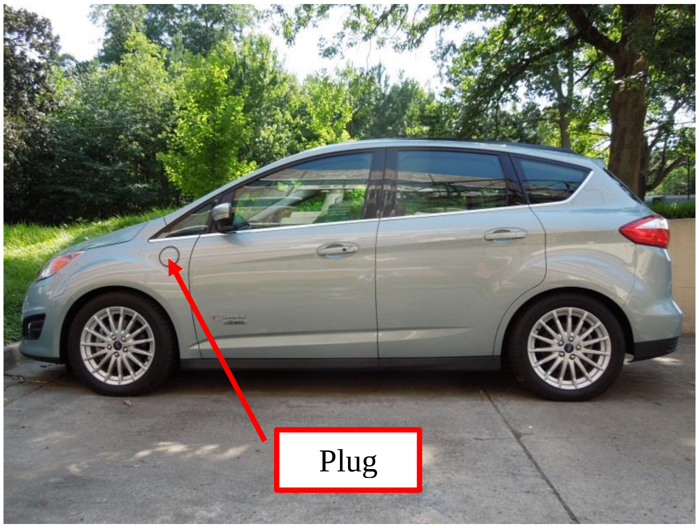

Figure 1. Ford C-MAX Energi Plug-in Hybrid Electric Vehicle

PHEVs and BEVs then have the potential to reduce the greenhouse gas emissions associated with personal transportation by reducing the reliance on the burning of fossil fuels by conventional internal combustion engines as a means of propulsion. However, in the United States many plug-in hybrid electric vehicles (PHEVs) and battery electric vehicles (BEVs) must still be plugged in to a grid that is heavily reliant on the burning of fossil fuels to charge. In 2013, as much as 67% of the electricity generated in the United States was generated by the burning of fossil fuels (U.S.E.I.A. 2013). The goal of this thesis is to identify a means of locally charging individual electrified passenger vehicles using alternative and/or regenerative energy sources. Regenerative energy sources will be considered those which recover energy that would normally be wasted in normal vehicle operation, and alternative energy sources will be considered those which generate electricity from sources auxiliary to normal to vehicle operation.

In developing such a system, various alternative and regenerative energy sources were investigated with the intent of reaching a specified daily energy goal of 7.6 kWh; sufficient to charge a PHEV. These energy sources were evaluated based upon specified criteria. Of upmost importance, the energy sources should be capable of reaching or nearly reaching the specified daily energy goal. If a single technology is not capable of reaching this goal, promising supplementary energy sources may be considered. Following the daily energy capabilities of the technology, it is desired that the energy source utilize the maximum amount of on-vehicle technology as possible. In other words, it is desired that the energy source not generate electricity entirely independent of the vehicle, and that the vehicle be involved in the electricity generation as much as possible. Also of high importance is the applicability of the technology to both PHEVs and BEVs. Although the primary focus of this research is to reach a daily energy goal sufficient to charge a PHEV, the technology should also be applicable and ideally scalable to the energy requirements of a BEV. It is also desired that the technology be a novel application of an established technology. In other words, the energy sources should be proven technologies and not technologies still in the research and development stages. That said the implementation of the technologies should be innovative.

The primary technological categories considered include but are not limited to regenerative and solar technologies. Regenerative braking and similar kinetic energy recovery technologies are already implemented on many PHEVs and BEVs, and therefore do not represent novel technologies and will not be considered in this study. Regenerative shock absorbers present an emerging technology of particular interest as they have the potential to be a simple retrofit to almost any existing vehicle. An analysis of the potential energy recoverable by regenerative shock absorbers on a realistic drive cycle is conducted in Chapter 4: Regenerative Shock Absorbers.

Waste heat recovery and other thermal regenerative technologies, although very promising to PHEVs, were not considered in this study as they are not well suited to BEVs - which lack an internal combustion engine. Regenerative technologies involving piezoelectrics and similar technologies, like the piezoelectric vibration energy harvesting tire system described by (Singh, Bedekar et al. 2012), were initially considered, but quickly discounted due to their extremely low power output. A colleague also investigated the feasibility of adding a small wind turbine to the turbulent wake a vehicle, and determined that the energy required to transport the mass of the turbine outweighed the energy generated. The energy required to transport the added mass of any technology added to a vehicle is an important metric to consider in evaluating the performance of a technology, and this effect is explored further in Chapter 3: Drive Cycle Energy Analysis of Adding Mass to a Vehicle.

Today’s solar photovoltaic technologies are capable of achieving higher efficiencies than ever before and as a result photovoltaics are becoming increasingly feasible as a supplementary energy source for electrified passenger vehicles. An investigation of the energy recoverable by the addition of photovoltaics to the body panels of a passenger vehicle is conducted in Chapter 5: Solar Power. The investigation of solar technologies will not include concentrated solar thermal technologies. In addition, high efficiency multi-junction photovoltaic cells, although becoming increasingly popular in commercial applications will not be considered in this study by request of the research sponsor. Finally, hydrogen and other types of fuel cells will not be considered in this study.

The investigation of technologies indicated that a major opportunity lies in solar technologies, and in particular concentrated photovoltaics. Design alternatives for a concentrated photovoltaic system capable of reaching the desired energy goal are described in Chapter 6: Concentrated Photovoltaics. The design alternatives utilize Fresnel lenses as a means of concentrating a large area of sunlight onto an array of photovoltaics affixed to a vehicle. Various tracking mechanisms for the concentrating systems have been outlined to meet the stated design criteria. 3-D ray tracing algorithms have been developed to determine the path of the tracking mechanisms depending upon the time of year and on the geographic location. The same algorithms have been used in conjunction with typical meteorological year data to determine the expected output of the concentrating systems based upon the solar resource and solar angles at a specific place and time.

The findings suggest that a concentrated photovoltaic system designed specifically for charging an electrified vehicle may generate sufficient energy over the course of a day to power a typical driver’s trips. The ability of the system to reach the daily energy goal is however dependent on several factors, including geographic location, time of year, and weather. For such a concentrating system to be commercially feasible there are still many design challenges to be overcome. Design limitations and implications for further research are discussed in Chapter 8: Recommendations and Future Work.

CHAPTER 2: LITERATURE REVIEW

2.1 Sustainability assessment of PHEVs and BEVs

Prior work has identified that charging PHEVs and BEVs with low-carbon renewable energy can significantly reduce the life cycle greenhouse gas (GHG) emissions of the vehicle when compared to conventional internal combustion engines and to PHEVs charged using conventional and theoretical utility electricity generation mixtures.

Faria, Moura et al. (2012) conducted a sustainability assessment of electric vehicles as a personal mobility system using a well-to-wheel life cycle assessment. It was demonstrated that the reduction in GHG emissions of PHEVs and BEVs is directly related to the source of the electricity used to charge the vehicles. Although there are nearly zero GHG emissions by renewable energy sources in operation, there are still indirect emissions related to the manufacture, installation, etc. of the energy source. These emissions are estimated to be 10-25 gCO_2/kWh for wind and hydro and 30-100 gCO_2/kWh for solar PV. In comparison, the emissions resulting from the burning of fossil fuels is estimated to be 600-1200 gCO_2/kWh. It was concluded that considerable impact can be made on the reduction of GHG emissions by utilizing renewable energies to charge PHEVs and BEVs.

Duvall (2007) conducted an environmental assessment of PHEVs using a well to wheel life cycle assessment. It was shown that a PHEV with a 20 mile electric range reduces GHG emissions by 28% to 67% as compared to a conventional internal combustion engine vehicle with a fuel economy of 24.6 miles per gallon regardless of the electricity supply. It was also demonstrated that the reduction in GHG emissions of PHEVs and BEVs is directly related to the mix of electricity sources used to charge the vehicles. In considering fourteen distinct power plant technologies, it was shown that PHEVs recharged by low- and non-emitting generation technologies emitted the lowest level of GHGs per mile.

In a report on the transitions to alternative transportation technologies, the National Academies Press concluded that PHEVs with a 40 mile range would not contribute to a significant reduction in GHG emissions unless the electricity used to charge them is generated using a low emission source like renewables, nuclear, or fossil fuel plants with a carbon capture system (NAP 2010).

Samaras and Meisterling (2008) conducted a life cycle assessment of GHG emissions from PHEVs considering vehicle and battery production and the use phase of the vehicle. It was shown that using electricity generated by the average mixture of sources in the United States, or 670 gCO_2/kWh, resulted in life cycle GHG emissions from a PHEV 32% lower than that of a conventional internal combustion engine vehicle. For a low-carbon energy generation mixture, including renewables, nuclear, and coal with carbon capture systems and with GHG emissions of 200 gCO_2/kWh, the life cycle GHG emissions of a PHEV were 51-63% lower than that of a conventional internal combustion engine vehicle.

Lipman and Delucchi (2010) conducted an overview of studies pertaining to the expected GHG reductions by BEVs, PHEVs, and fuel cell vehicles. They found that when compared to conventional vehicles BEVs have the potential to reduce GHG by 20-50% when charging with a typical United States energy generation mixture, and by up to 90% when charging with renewable or nuclear power sources.

Charging PHEVs and BEVs with low-carbon renewable energy is of course not the only means of reducing the life cycle GHG emissions of the vehicles. Another popular method is to increase the operating efficiency of the vehicle. While such efforts are beyond the scope of this research, it is worth noting that considerable research is being done in this area. Optimized power management strategies demonstrate the potential to considerably reduce the amount of energy wasted during vehicle operation, thereby improving operating efficiency. For additional literature on optimized power management strategies, see references: (Bauer, Suchaneck et al. 2014), (Dib, Chasse et al. 2014), (Hannan, Azidin et al. 2012), (He, Xiong et al. 2012), (Hou, Ouyang et al. 2014), (Khayyam and Bab-Hadiashar 2014), (Neubauer, Brooker et al. 2013), (Nüesch, Wang et al. 2014), (Payri, Guardiola et al. 2014), (Shams-Zahraei, Kouzani et al. 2012), (Sciarretta, Serrao et al. 2014), (Sousa, Vale et al. 2014), (Torres, Gonzalez et al. 2014), (Tribioli, Barbieri et al. 2014), (Trovão, Pereirinha et al. 2013).

2.2 Regenerative Technologies for PHEVs and BEVs

While adding additional low-carbon renewable energy sources to the national energy mixture would be one solution to reducing the GHG emissions associated with charging electrified passenger vehicles, there are many complications to doing so that are beyond the scope of this study. As previously stated, the purpose of this study is to identify a means of locally charging individual electrified passenger vehicles using alternative and/or regenerative energy sources. Many efforts have been made in developing alternative and regenerative methods of adding charge to electrified passenger vehicles.

Prior work has been done to develop shock absorbers capable of recovering energy that would otherwise be lost as heat in traditional shock absorbers.

Kang-Min, Hyung-Jo et al. (2007) developed a shock absorber which utilizes a linear electromagnetic induction device capable of generating up to 800 mW with an excitation amplitude and frequency of 15 mm and 3 Hz respectively. (Chao and Wei-Hsin 2012), (Choi, Seong et al. 2009), and (Bogdan 2014) have all developed similar energy-harvesting shock absorbers which utilize linear electromagnetic induction to generate electricity.

Li, Zhu et al. (2014) have developed a shock absorber which utilizes a hydraulic generator to generate electricity by converting the linear motion of fluid in the damper to oscillatory motion which drives the generator. For an optimized load resistance of 7.5 Ohms and a excitation frequency and amplitude of 2 Hz and 8 mm respectively, the experimental prototype was capable of capturing a peak instantaneous power of 248.8 W and a mean power of 114.1 W. (Chuan and Peter 2013) (Fang, Guo et al. 2013), and (Levant 2013) have developed similar devices.

Zhongjie, Lei et al. (2013) developed a shock absorber which mechanically converts the linear motion of the shock absorber to electricity using a generator, rack and pinion, and specially designed mechanical-motion rectifier. The experimental prototype was demonstrated to achieve a peak power of 104.3 W and an average power of 40.4 W with a 30 Ohm load and an excitation frequency and amplitude of 3 Hz and 5 mm, respectively. Zhang, Cao et al. (2012) proposed a similar system involving active energy-regenerative controllers for DC-motor-based suspension.

2.3 Alternative Renewable Energy Sources for PHEVs and BEVs

In addition to regenerative methods, alternative renewable energy sources have also been investigated. The concept of a solar powered vehicle has been around for many years. Competitions like the World solar Challenge have been around since the 1980’s to test the performance of vehicles specially design to run on only solar power (Challenge 2014). There has however been very little attention given to vehicle integrated PV in the literature.

Letendre (2007) provided a brief overview of the approaches to using solar energy to power vehicles. The first approach being vehicles designed for solar-powered car competitions, like the aforementioned World Solar Challenge, which are not intended for commercial applications. The second approach being commercial scale developments of vehicle integrated PV.

Rizzo (2010) demonstrated that 25% of a typical drivers' daily energy demands in the United Kingdom may be met by vehicle integrated PV.

Keshri, Bertoluzzo et al. (2014) perform an experimental evaluation of the performance of an electric city car with an integrated PV panel.

Giannouli and Yianoulis (2012) conducted a study on the incorporation of PV systems as an auxiliary power source for hybrid and electric vehicles. Their findings suggest that the most important factors to consider in selecting PV cell type for vehicular applications are PV cost and efficiency. They go on to propose that monocrystalline PV is the most cost-effective cell type.

G. Coraggio (2010) developed a self-tracking solar roof to increase the efficacy of PV on solar assisted vehicles while they are parked. For additional publications on the design see references: (Coraggio 2011) and (Rizzo 2013).

Huang, Tzeng et al. (2005) describes an intelligent vehicle ventilation system capable of running off a vehicle integrated PV array. PV array specifications were not provided as the focus of the study was on the ventilation system.

Adinolfi (2008) conducted a study on the design of a hybrid solar vehicle, taking into account the performance, fuel consumption, weight, and cost of the components; however the study lacked any conclusive results.

2.4 Conclusion

Previous studies have identified that charging PHEVs with low-carbon renewable energy sources can reduce the life cycle GHG emissions of the vehicle by up to 67% when compared to conventional internal combustion engines. Charging BEVs with low-carbon renewable energy sources can reduce the life cycle GHG emissions of the vehicle by up to 90% when compared to conventional internal combustion engines. In reviewing prior work, regenerative shock absorbers demonstrate the potential to recover an appreciable amount of power under controlled scenarios, but little work has been done to determine the energy recoverable by such systems under a realistic drive cycle. Vehicle integrated solar photovoltaics have received very little attention in the literature, and most studies do not address the energy recoverable by such systems.

CHAPTER 3: DRIVE CYCLE ENERGY ANALYSIS OF ADDING MASS TO A VEHICLE

3.1 Modeling the Energy Requirements of Adding Mass to a Vehicle

In adding a regenerative or alternative energy source to a vehicle, the energy that is recaptured or generated should at a very minimum be equal to the energy expended in transporting the energy source. If this condition is not met, the addition of the energy source will result in a net loss in energy transfer. In order to determine the energy expenditure resulting from the addition of mass to a vehicle a parametric study was conducted for several EPA dynamometer drive schedules. In the study, the energy required to transport 2 kg, 5 kg, and 10 kg masses was calculated for the Urban Dynamometer Driving Schedule (UDDS), Highway Fuel Economy Driving Schedule (HWFET), New York City Cycle (NYCC), and the US06 drive schedule, which is characterized as high acceleration aggressive driving.

The energy required to transport the masses was determined by calculating the work that must be done by the vehicle in order to accelerate the masses. The work done to decelerate the masses was neglected; however, in a vehicle equipped with regenerative braking some of the energy required to decelerate the masses may be recovered. In this way the study represents a worst case scenario. By applying classical mechanics, the work, W necessary to accelerate an object of mass, m at a constant rate, a over a distance, Δx is

$$W = ma\Delta x \tag{1}.$$

The (EPA 2013) provides drive schedules containing the vehicle velocity at one second intervals. With this information, the distance traveled by the vehicle in a one second interval can be calculated by

$$\Delta x = (v_f^2 - v_i^2)/\, 2a \tag{2}$$

where, v_f is the vehicle's velocity at the current time step, v_i is the vehicle's velocity at the previous time step, and since the velocities are provided at one second intervals, the acceleration a is simply the difference between v_f and v_i. The distance traveled by the vehicle in a one second interval along with the corresponding acceleration can then be substituted into Equation 1 to find the instataneous energy consumption in Joules for a given mass, m.

3.2 Results and Discussion

A sample of the energy consumption calculations for the UDDS is provided in Table 1. The vehicle speed in miles per hour (mph) is the EPA provided velocity of the vehicle at a particular instant in time. For the purposes of calculation, this value is converted in meters per second (m/s). Acceleration is the time derivative of velocity, and since the vehicle velocities are provided on one second intervals, the vehicle's acceleration between to concecutive time steps can be determined as the diffence in the current time step's velocity and the previous time step's velocity. The acceleration between two consecutive time steps is assumed to be constant. Using the current time step velocity, the previous time step velocity, and the calculated acceleration, the distance traveled by the vehicle between the two time steps can be calculated using Equation 2. Finally, the energy necessary to accelerate a given mass, m, at a rate, a, over a distance Δx, is calculated using Equation 1.

Table 1. Example of UDDS Energy Consumption Calculations

DRIVE CYCLE	UDDS						
					Energy Consumed (J)		
Time (s)	Vehicle Speed (mph)	Vehicle Speed (m/s)	dv/dt (m/s^2)	Displacement (m)	10 kg mass	5 kg mass	2 kg mass
⋮	⋮	⋮	⋮	⋮	⋮	⋮	⋮
21.00	3.00	1.34	1.34	0.67	8.99	4.50	1.80
22.00	5.90	2.64	1.30	1.99	25.79	12.89	5.16
23.00	8.60	3.84	1.21	3.24	39.12	19.56	7.82
24.00	11.50	5.14	1.30	4.49	58.24	29.12	11.65
25.00	14.30	6.39	1.25	5.77	72.18	36.09	14.44
26.00	16.90	7.55	1.16	6.97	81.06	40.53	16.21
27.00	17.30	7.73	0.18	7.64	13.67	6.83	2.73
28.00	18.10	8.09	0.36	7.91	28.30	14.15	5.66
⋮	⋮	⋮	⋮	⋮	⋮	⋮	⋮

The UDDS and the corresponding instantaneous energy consumption for the three different masses considered are plotted below in Figure 2 and Figure 3 respectively. The UDDS is a 1369 second, or 22.8 minute long schedule, during the course of which 10,559 meters is traversed, and 1.2, 2.9, and 5.8 Wh is consumed in transporting the 2, 5, and 10 kg masses respectively. A typical driver may traverse a distance of 37 miles, or 59546 meters over the course of a day, and as such would require 6.6, 16.4, and 32.9 Wh to transport the 2, 5, and 10 kg masses respectively.

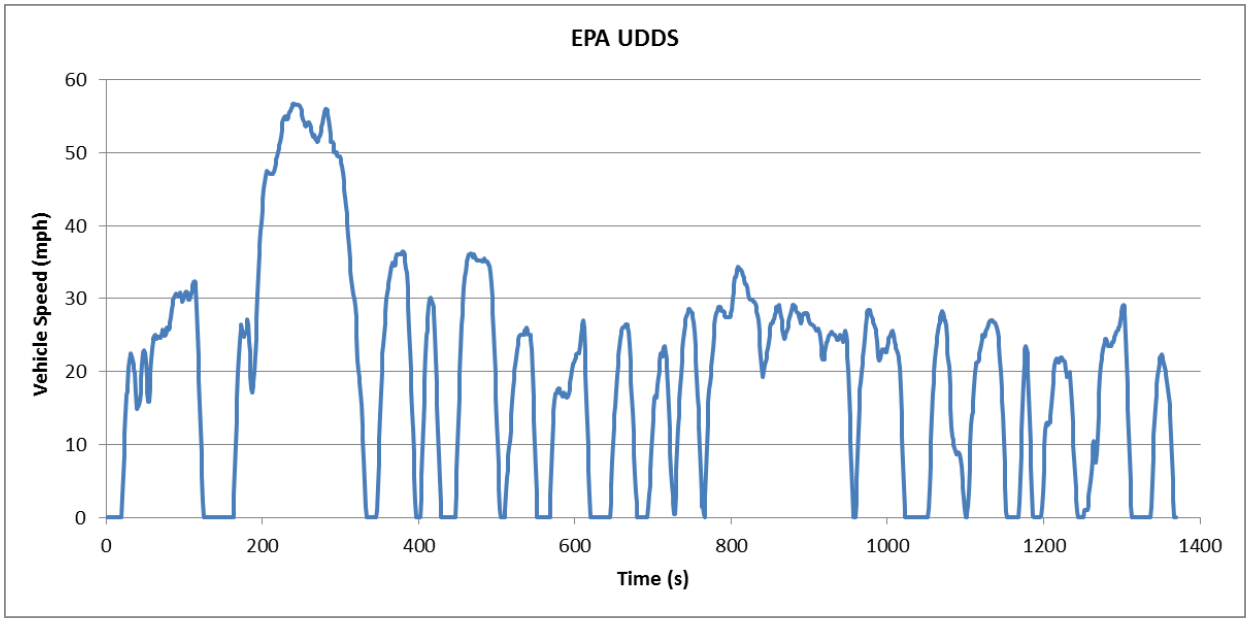

Figure 2. Urban Dynamometer Driving Schedule

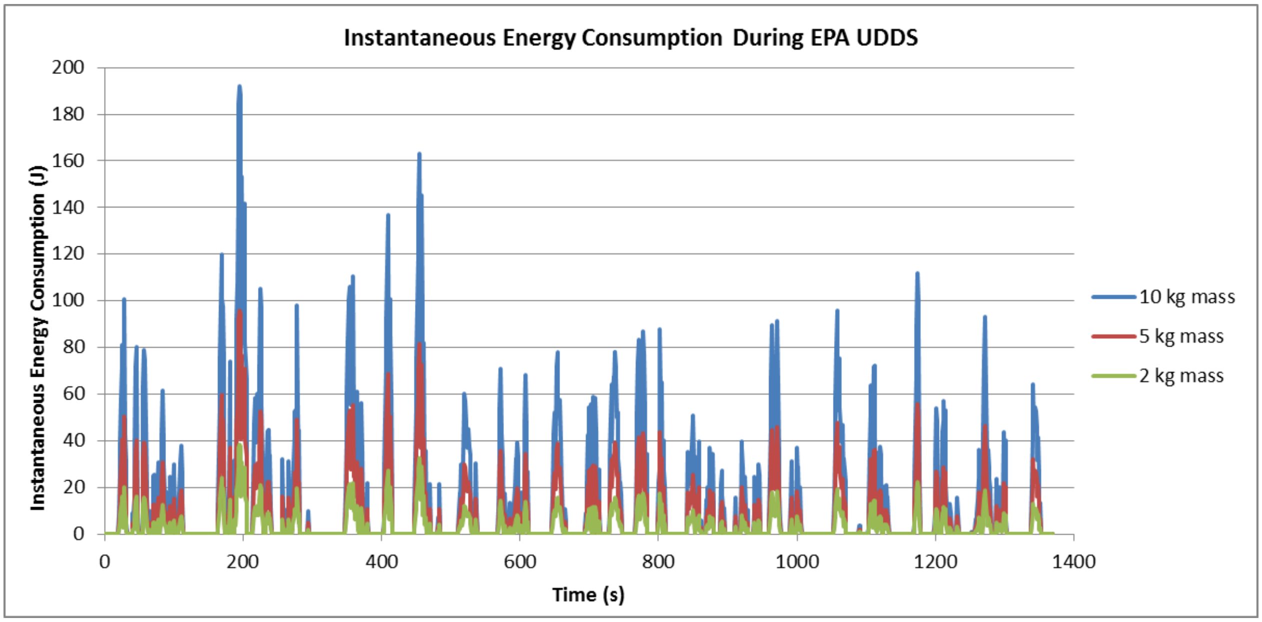

Figure 3. Energy Consumption During EPA UDDS

The HWFET and the corresponding instantaneous energy consumption for the three different masses considered are plotted below in Figure 4 and Figure 5 respectively. The HWFET is a 765 second, or 12.75 minute long schedule, during the course of which 13,535 meters is traversed, and 0.65, 1.6, and 3.2 Wh is consumed in transporting the 2, 5, and 10 kg masses respectively. A typical driver may traverse a distance of 37 miles, or 59546 meters over the course of a day, and as such would require 2.8, 7.1, and 14.2 Wh to transport the 2, 5, and 10 kg masses respectively.

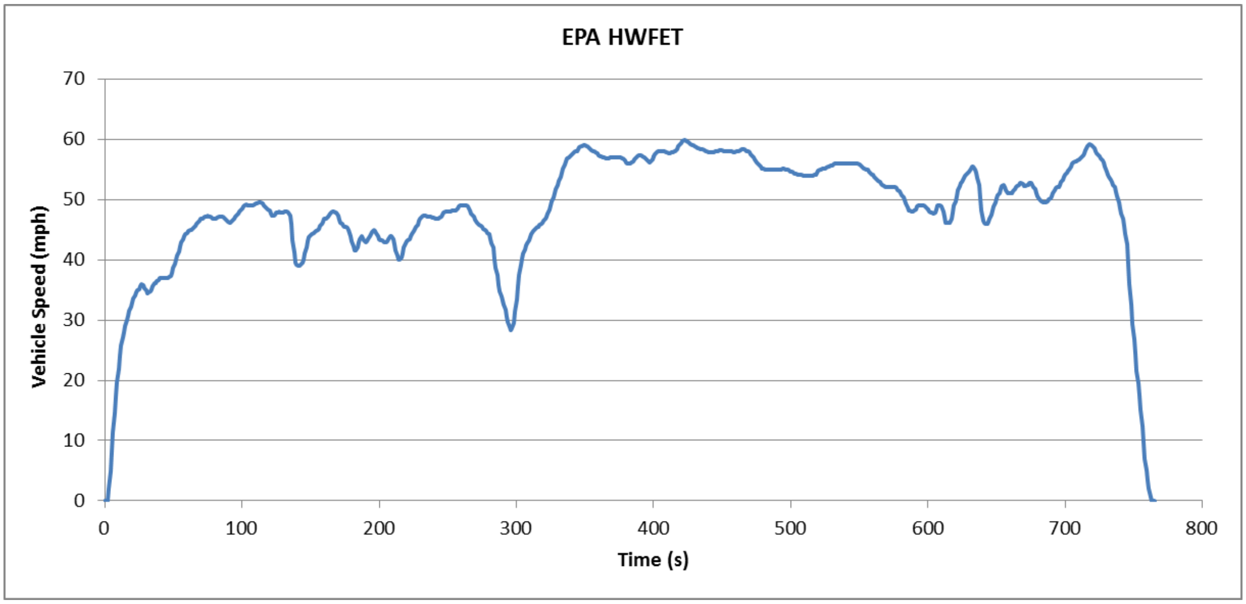

Figure 4. Highway Fuel Economy Driving Schedule

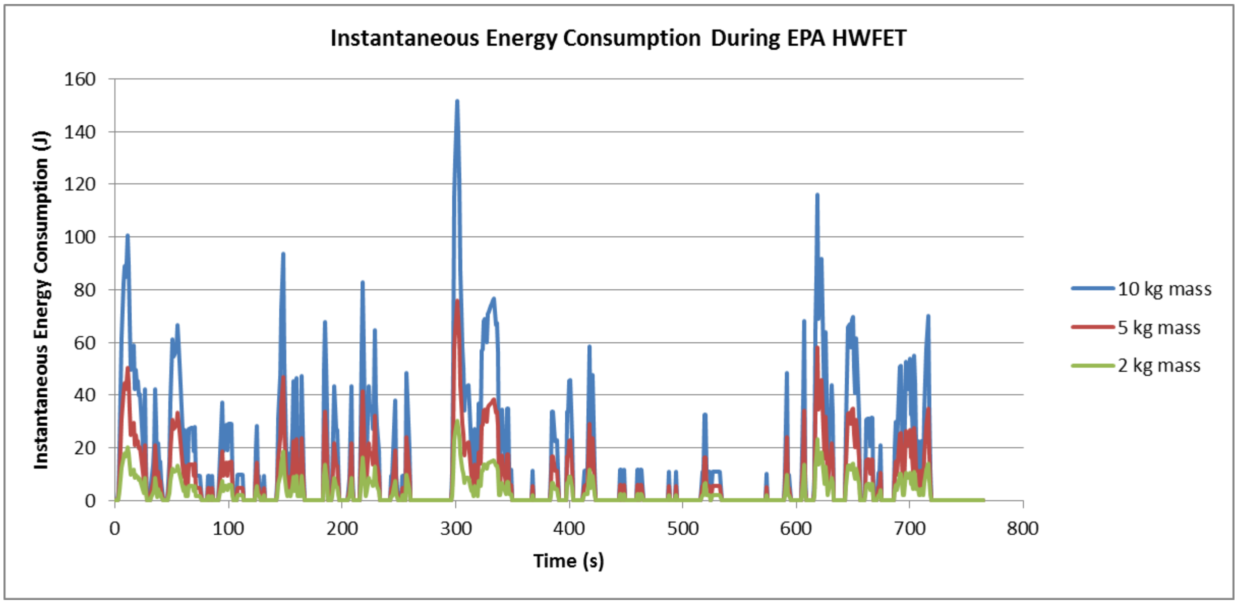

Figure 5. Energy Consumption During EPA HWFET

The NYCC and the corresponding instantaneous energy consumption for the three different masses considered are plotted below in Figure 6 and Figure 7 respectively. The NYCC is a 598 second, or 9.97 minute long schedule, during the course of which 1842 meters is traversed, and 0.33, 0.81, and 1.6 Wh is consumed in transporting the 2, 5, and 10 kg masses respectively. A typical driver may traverse a distance of 37 miles, or 59546 meters over the course of a day, and as such would require 10.5, 26.3, and 52.6 Wh to transport the 2, 5, and 10 kg masses respectively.

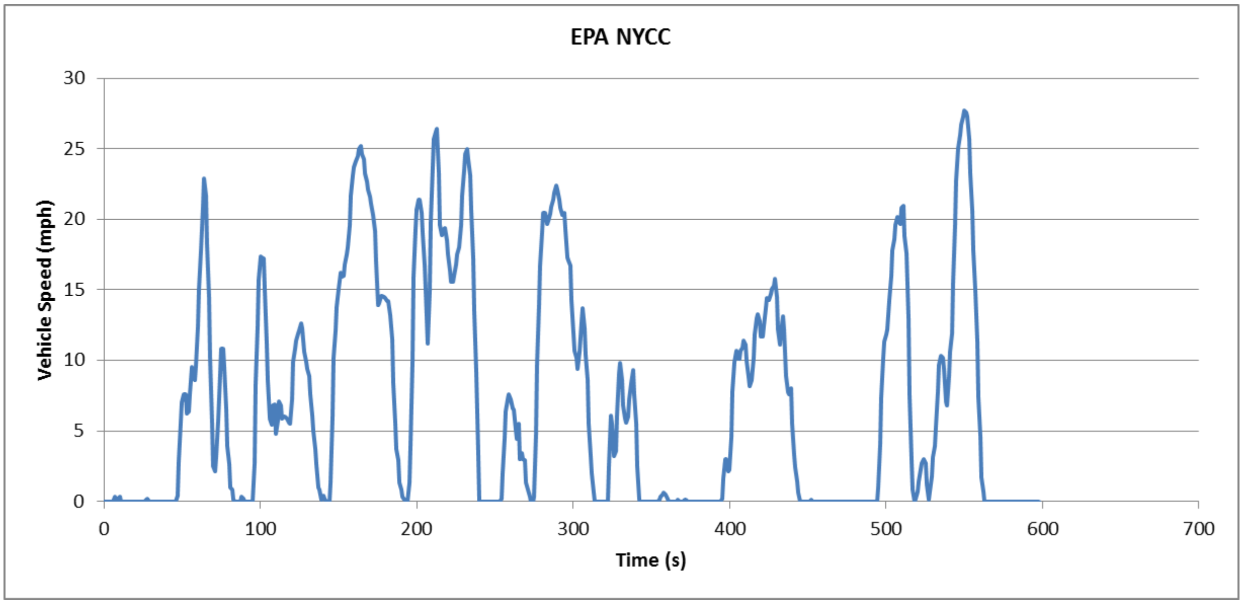

Figure 6. EPA New York City Driving Schedule

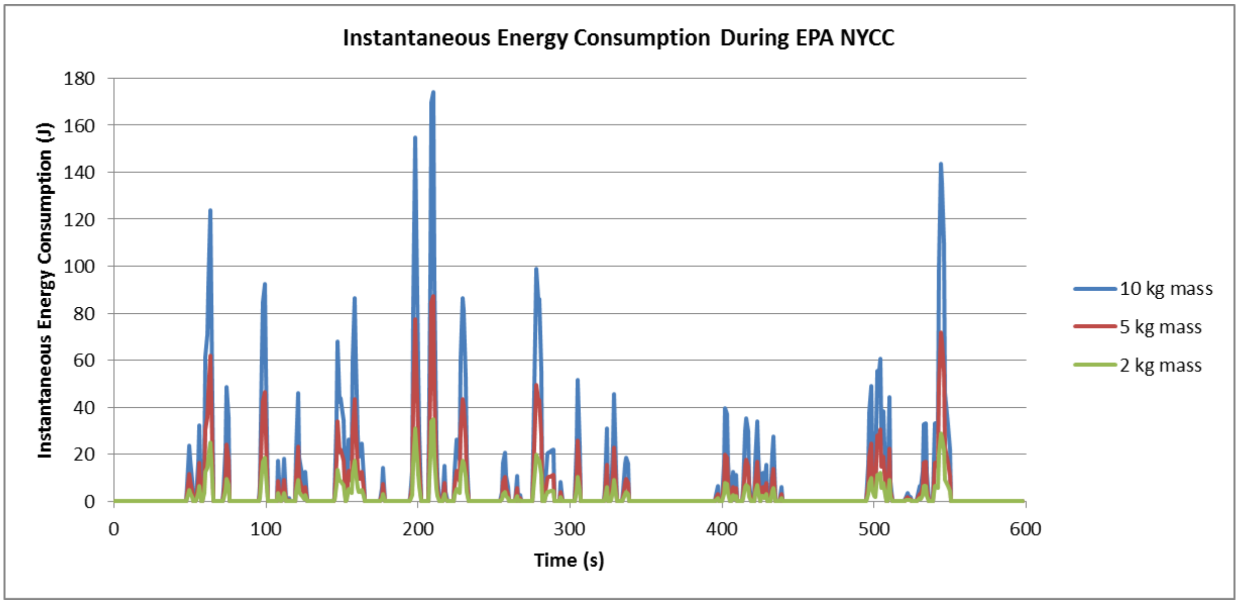

Figure 7. Energy Consumption During EPA NYC Driving Schedule

The US06 drive schedule and the corresponding instantaneous energy consumption for the three different masses considered are plotted below in Figure 8 and Figure 9respectively. The US06 drive schedule is a 600 second, or 10 minute long schedule, during the course of which 11935 meters is traversed, and 1.5, 3.8, and 7.5 Wh is consumed in transporting the 2, 5, and 10 kg masses respectively. A typical driver may traverse a distance of 37 miles, or 59546 meters over the course of a day, and as such would require 7.5, 18.8, and 37.6 Wh to transport the 2, 5, and 10 kg masses respectively.

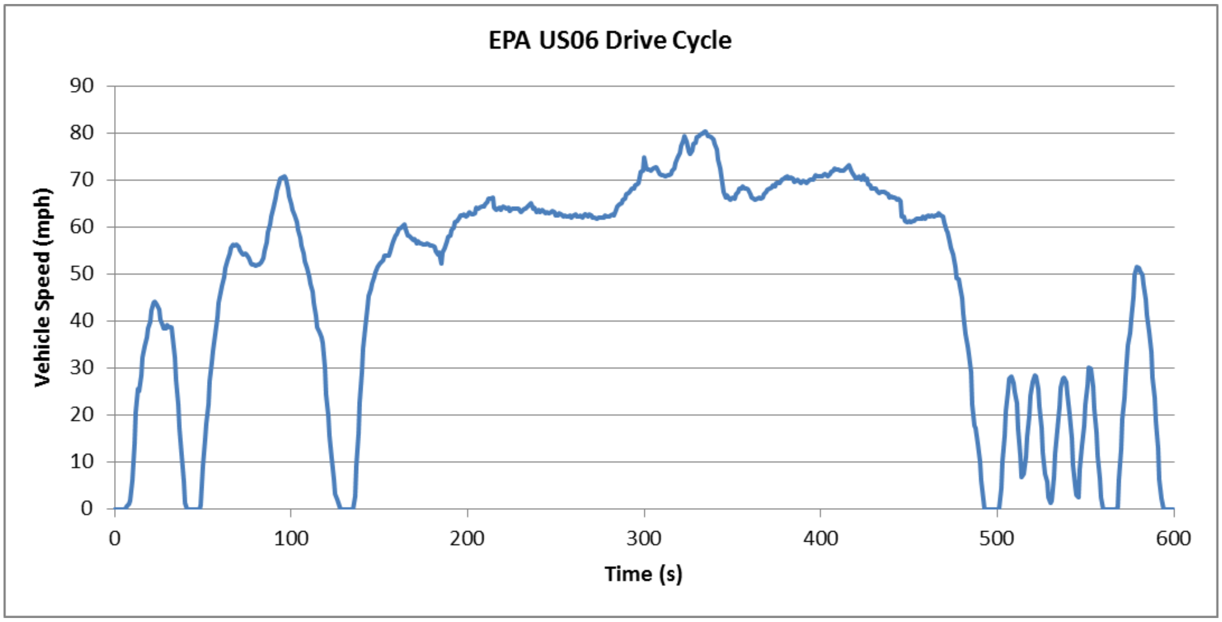

Figure 8. EPA US06 Driving Schedule

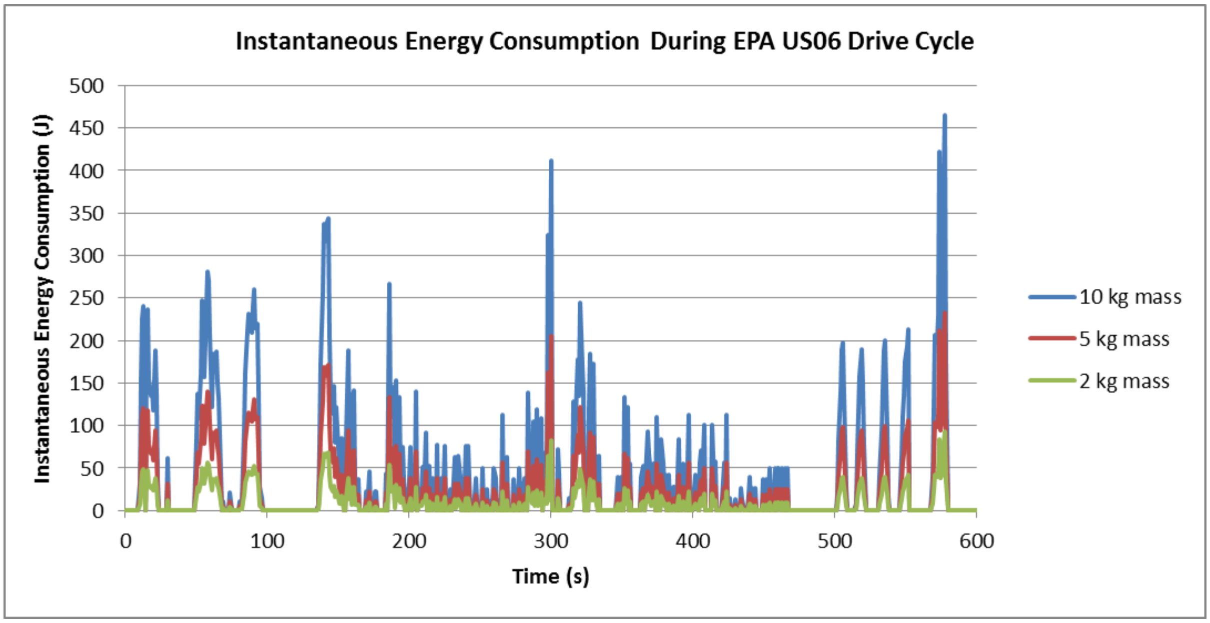

Figure 9. Energy Consumption During EPA US06 Driving Schedule

Table 2. Energy Required to Transport 2, 5, and 10 kg masses for Several EPA Drive Cycles

	Energy Consumed During Cycle (Wh)			**# of Cycles for Average Trip**	**Energy Consumed During Average Trip (Wh)**		
	2 kg	**5 kg**	**10 kg**		**2 kg**	**5 kg**	**10 kg**
UDDS	1.2	2.9	5.8	5.6	6.6	16.4	32.9
HWFET	0.65	1.6	3.2	4.4	2.8	7.1	14.2
NYCC	0.33	0.81	1.6	32.3	10.5	26.3	52.6
US06	1.5	3.8	7.5	5.0	7.5	18.8	37.6

While the findings of this study only apply to the three specific masses considered, the same process may be applied with any given mass in order to determine the energy requirement of the added mass for an average daily trip.

CHAPTER 4: REGENERATIVE SHOCK ABSORBERS

4.1 Technology Overview

Shock absorbers are designed to dampen the spring oscillations in a vehicle suspension, thus improving ride quality and vehicle handling. This can be accomplished in a number of manners, the majority of which can be simplified to a simple damper. A simple damper is effectively a cylinder containing a viscous fluid such as oil and a piston with small orifices, through which the viscous fluid can flow. The simple damper is able to dissipate kinetic energy resulting from the displacement of the piston as thermal energy via viscous friction. As shown in Figure 10, when a force is applied to the piston, the linear motion of the piston forces the viscous fluid through the small orifices in the piston. The viscous fluid resists the motion of the piston, and energy is dissipated as heat due to the friction of the fluid shearing as it is forced through the orifices.

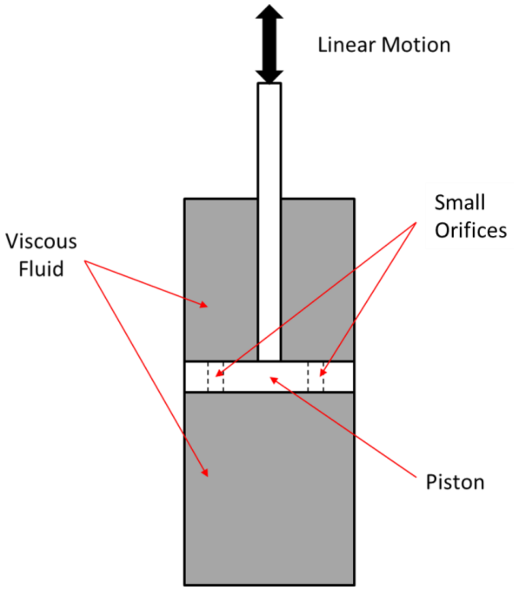

Figure 10. Simple Damper

The premise behind regenerative shock absorbers is to capture the energy that is wasted as heat in traditional shock absorbers. The following outlines a simple model devised to determine the maximum theoretical energy that could be recovered by regenerative shock absorbers applied to a C-MAX. In determining the maximum theoretical energy recoverable, it can be more easily decided whether or not regenerative shock absorbers present a viable means of obtaining the daily energy goal, and whether or not further investigation should be conducted.

4.2 Determining the Energy Available in C-MAX Shock Absorbers for a Realistic Drive Cycle

The work done by the shock absorbers in dissipating kinetic energy as heat with a lower exergy during a given trip represents the theoretical maximum energy that could be recovered by regenerative shock absorbers during the same trip. In actuality the energy recovered by a regenerative shock absorber would be reduced due to efficiency losses; however, for a preliminary understanding of whether or not sufficient energy is available in the shock absorbers to reach the daily energy goal, the theoretical maximum will be adequate. To determine the maximum theoretical energy, Adams, a multi-body dynamics software from MCS software, was used to model the C-MAX suspension and collect the upper linkage forces and positions relative to the lower linkage. Using this information the energy, E_i, dissipated between two consecutive time steps of length, Δt = 0.05 seconds or 0.0000138 hours is determined by

$$E_i = P_i * \Delta t \tag{3}.$$

Here, P_i is the instantaneous power dissipated, calculated as

$$P_i = F_i * V_i \tag{4}$$

where F_i is the upper linkage force and V_i is the relative velocity of the upper linkage. The relative velocity of the upper linkage can be determined using the relative change in upper linkage position, Δx_i, and the time step, Δt, by

$$V_i = \frac{\Delta x_i}{\Delta t} \quad (5).$$

The total energy dissipated during a trip can then be determined by summing the energy dissipated at each time step.

4.3 Drive Cycle Composition

In order to quantify the energy that could be regenerated in a typical trip, a realistic drive cycle was created with input from Ford Motor Company. The drive cycle created is designed to represent a trip that a typical driver might take to work every day, and involves a combination of different road surfaces and vehicle speeds. The road surfaces used in the model were developed by Ford, and are designed to replicate the surface conditions and contours experienced on actual roads. The road surfaces included in the model are:

- Brushed Concrete
- Coarse Road
- FEC Ride Road
- DeSoto

Brushed concrete represents a smooth road with few large amplitude – low frequency undulations. The coarse road represents a road with an aggregate surface and few large amplitude – low frequency undulations. The FEC ride road represents a smooth road with some larger amplitude undulations, and the DeSoto road is a combination of the FEC ride road and the coarse road. The upper linkage position of the LF shock absorber on some of the road surfaces considered in this analysis are provided in Figure 11, Figure 12, and Figure 13.

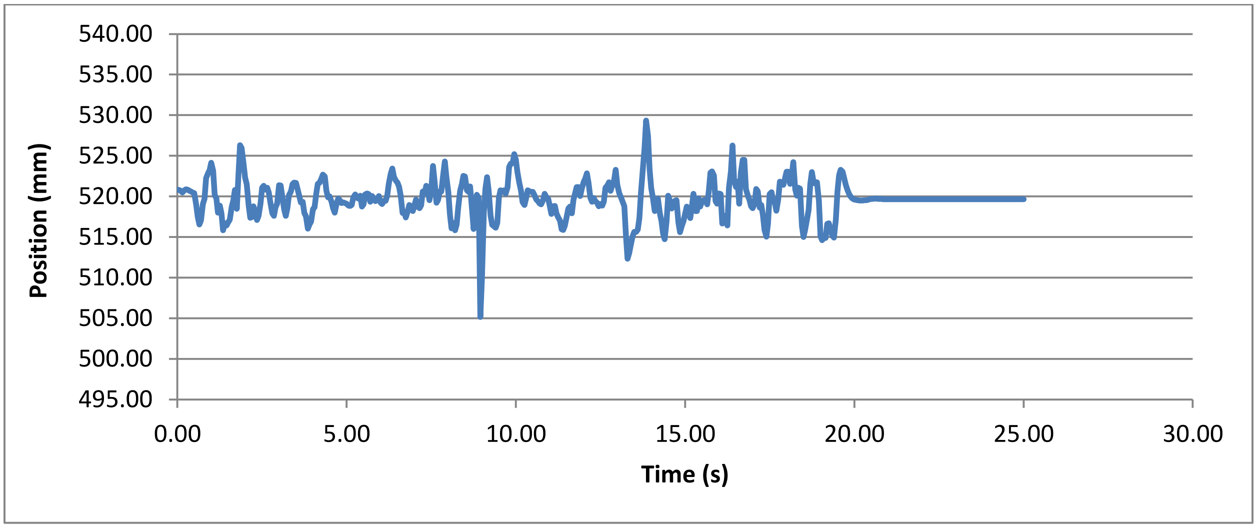

Figure 11. Upper Linkage Position of LF shock at 30 mph on Brushed Concrete

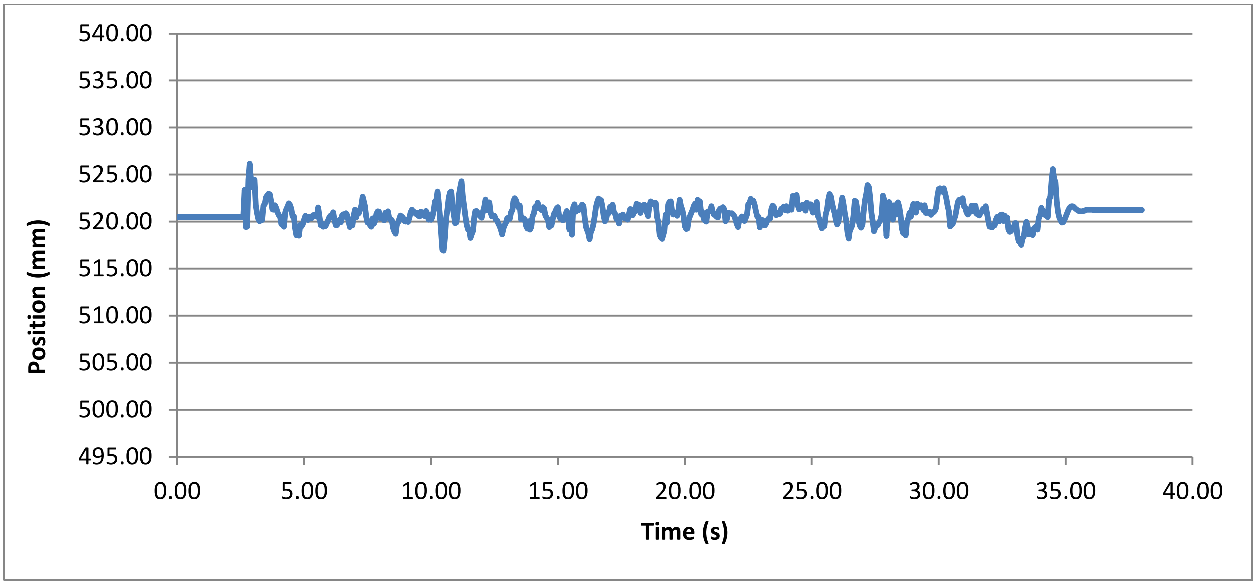

Figure 12. Upper Linkage Position of LF shock at 40 mph on Coarse Road

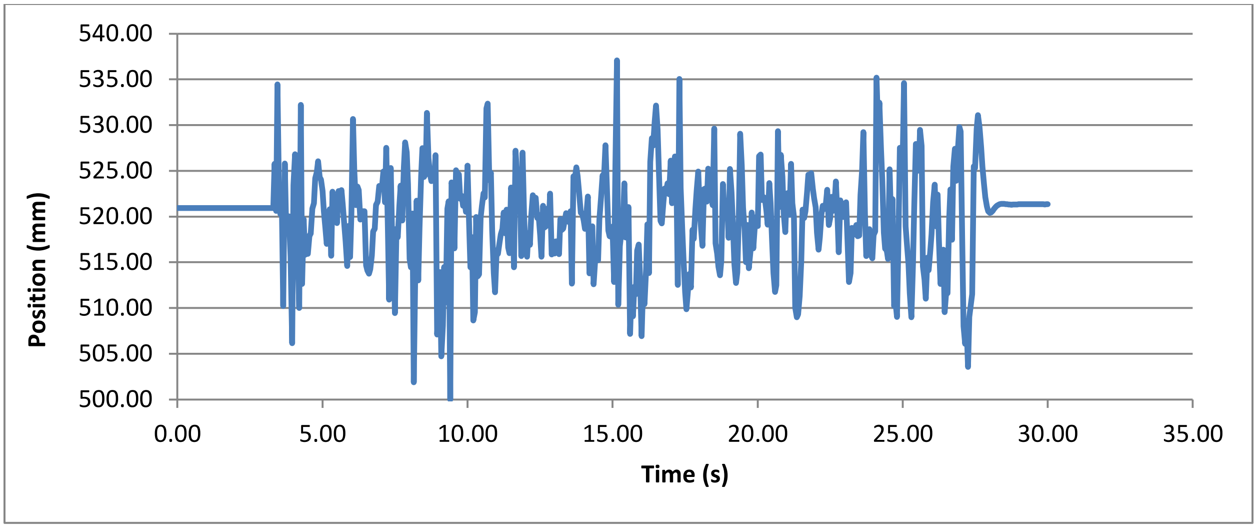

Figure 13. Upper Linkage Position of LF shock at 50 mph on DeSoto Road

In creating a realistic drive cycle, the average daily trip was assumed to be 37 miles. Of the 37 miles, 4 miles were assumed to be spent on coarse road at 30 miles per hour (mph), 1 mile was assumed to be spent on DeSoto road at 40 mph, and 10, 12, and 10 miles were assumed to be spent on brushed concrete at 30, 50, and 70 mph, respectively. The sample road surfaces used in the model cover only a short pass on each respective road type, and as a result it was necessary to use multiple passes over each road type to reach the assumed distance on each road. A breakdown of the drive cycle, including the total number of passes on each road surface necessary to cover the modeled drive cycle is shown below in Table 3.

Table 3. Drive Cycle Composition

	Assumed Mileage per Road Surface (mi)	Total Time Spent on Road Surface (hrs)	Single Pass Time Duration (s)	Miles for Single Pass (mi)	# of Passes Required for Assumed Mileage	Rounded # of Passes	Percent of Time Spent on Road Surface
Coarse road, 30mph	4	0.1372	38	0.317	12.63	13.00	7.74
DeSoto, 40mph	1	0.0250	30	0.333	3.00	3.00	1.79
Brushed concrete, 30mph	10	0.3333	25	0.208	48.00	48.00	28.57
Brushed concrete, 50mph	12	0.2375	15	0.208	57.60	57.00	33.93
Brushed concrete, 70mph	10	0.1436	11	0.214	46.75	47.00	27.98
Total	37	0.8767	N/A	N/A	N/A	168.00	100.0

Using the drive cycle outlined in Table 3, the velocity, instantaneous power dissipated, and energy dissipated by the upper linkage of each shock was calculated using Equations 5, 4, and 3 respectively. A sample tabulation for the left front (LF) shock on brushed concrete at 30 mph is provided in Table 4.

Table 4. Sample Calculations for Left Front Shock on Brushed Concrete at 30mph

Time (s)	Position (mm)	Velocity (m/s)	Force (N)	Instantaneous Power (W)	Energy (Wh)
⋮	⋮	⋮	⋮	⋮	⋮
1.90	525.96	-0.0073	381.32	2.77	0.0000
1.95	524.03	-0.0385	215.85	8.30	0.0001
2.00	522.29	-0.0348	231.79	8.07	0.0001
2.05	521.51	-0.0156	308.30	4.82	0.0001
2.10	518.91	-0.0519	414.36	21.52	0.0003
2.15	517.36	-0.0311	226.74	7.06	0.0001
⋮	⋮	⋮	⋮	⋮	⋮

4.4 Results and Discussion

The end goal of this analysis is to determine the energy recoverable by each shock absorber on a realistic drive cycle. Given that the time step of the model is very small, 0.05 seconds or 0.0000138 hours, the recoverable energy at each time step is also very small. As a result, in reviewing the output of the model it is more intuitive to observe the power dissipated by the damper at each time step. The profile of the instantaneous power dissipated by the LF shock on a single pass of brushed concrete at 30 mph is provided in Figure 14. The average power dissipated by the LF shock in a single pass of brushed concrete at 30 mph is 3.42 W and the energy recoverable is 0.0238 Wh.

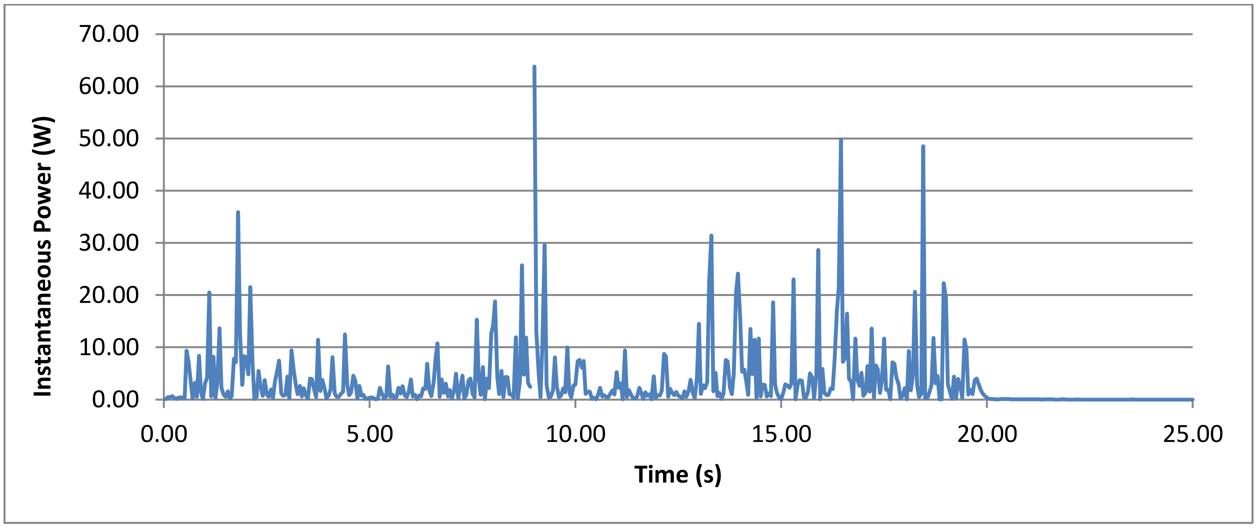

Figure 14. Instantaneous Power Output per Pass for LF Shock on Brushed Concrete at 30mph

The profile of the instantaneous power dissipated by the LF shock on a single pass of brushed concrete at 50 mph is provided in Figure 15. The average power dissipated by the LF shock in a single pass of brushed concrete at 50 mph is 9.05 W and the energy recoverable is 0.0378 Wh.

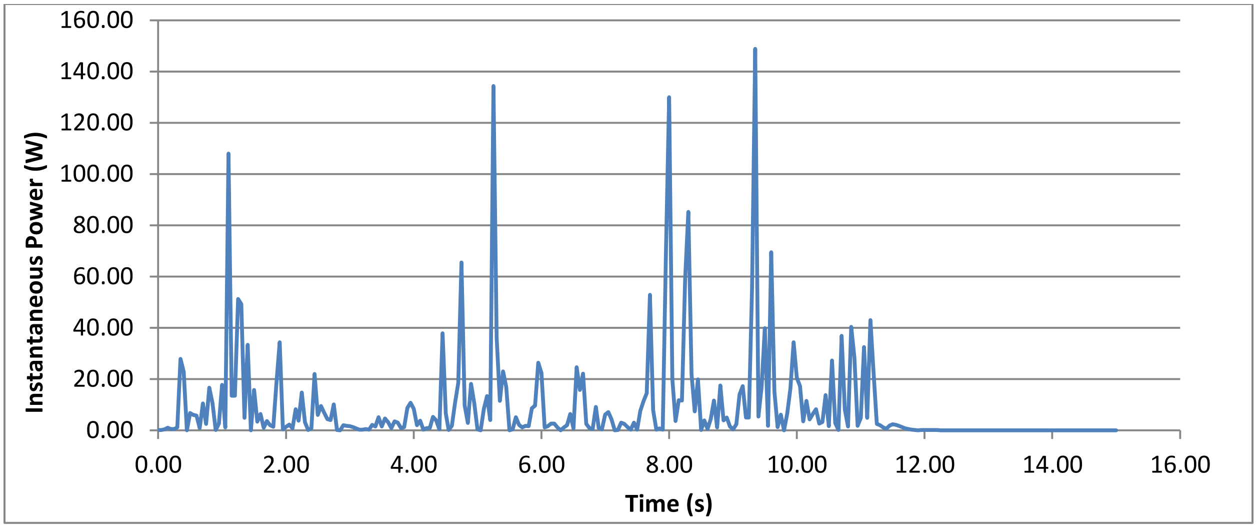

Figure 15. Instantaneous Power Output per Pass for LF Shock on Brushed Concrete at 50mph

The profile of the instantaneous power dissipated by the LF shock on a single pass of brushed concrete at 70 mph is provided in Figure 16. The average power dissipated by the LF shock in a single pass of brushed concrete at 70 mph is 20.13 W and the energy recoverable is 0.0615 Wh.

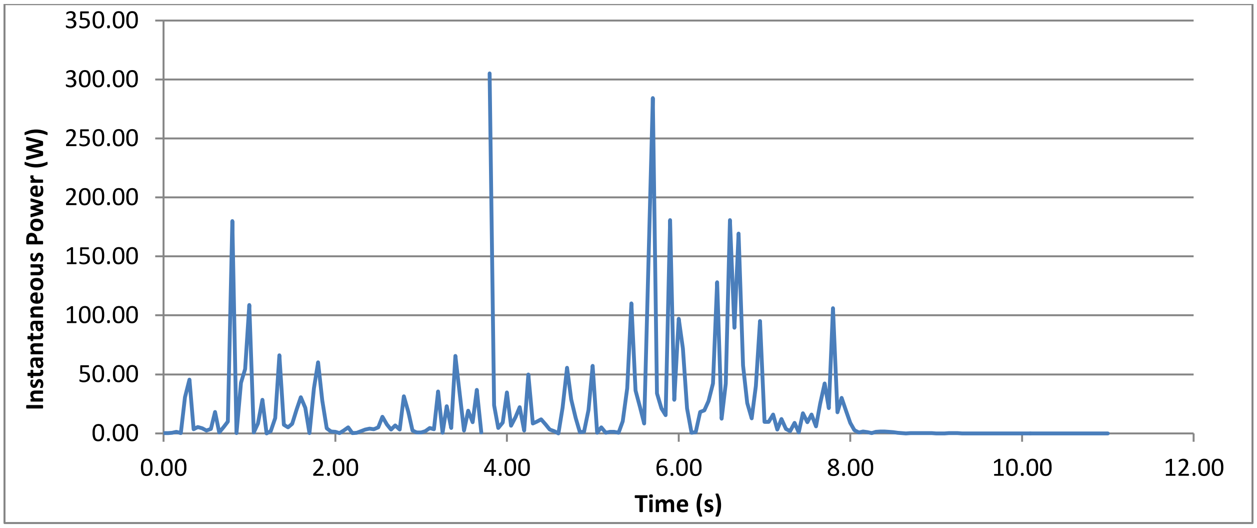

Figure 16. Instantaneous Power Output per Pass for LF Shock on Brushed Concrete at 70mph

The profile of the instantaneous power dissipated by the LF shock on a single pass of coarse road at 30 mph is provided in Figure 17. The average power dissipated by the LF shock in a single pass of coarse road at 30 mph is 1.59 W and the energy recoverable is 0.0168 Wh.

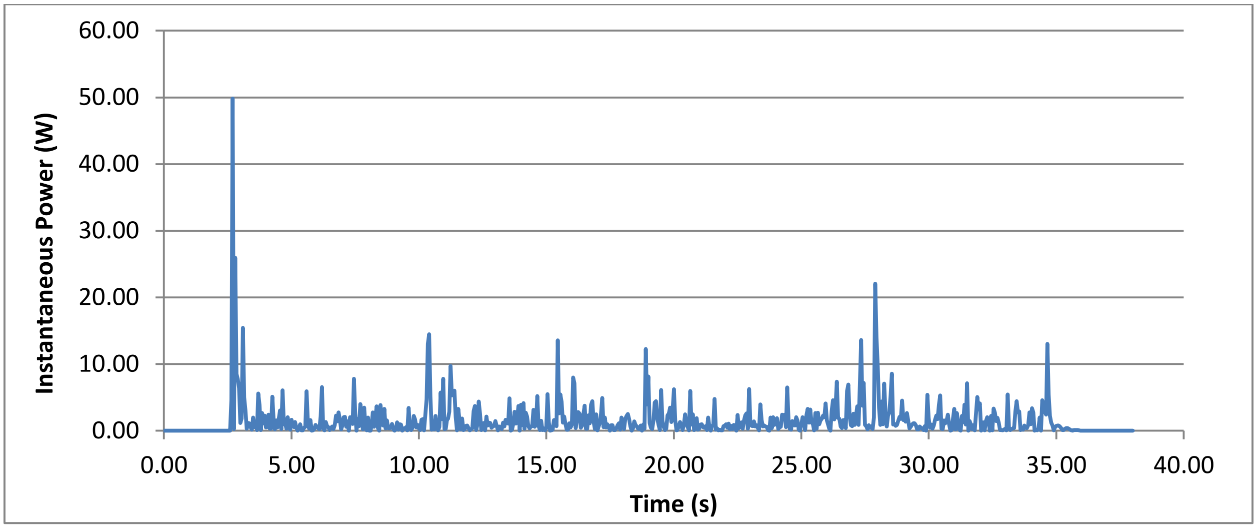

Figure 17. Instantaneous Power Output per Pass for LF Shock on Coarse Road at 30 mph

The profile of the instantaneous power dissipated by the LF shock on a single pass of DeSoto at 40 mph is provided in Figure 18. The average power dissipated by the LF shock in a single pass of DeSoto at 40 mph is 28.33 W and the energy recoverable is 0.2365 Wh.

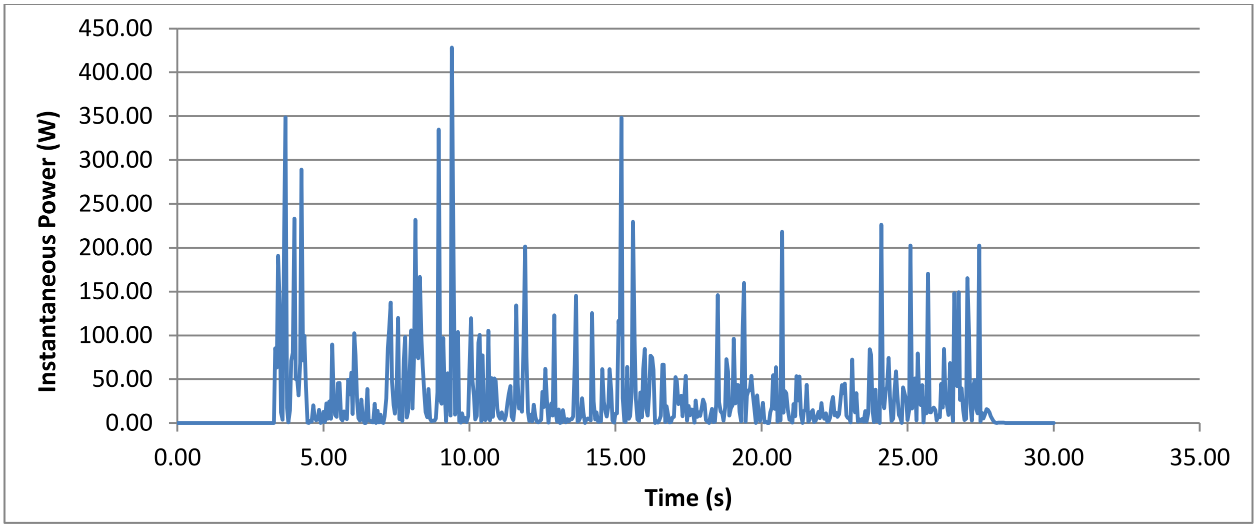

Figure 18. Instantaneous Power Output per Pass for LF Shock on DeSoto Road at 40 mph

Additional figures depicting the profiles of the instantaneous power dissipated by the right front (RF), left rear (LR), and right rear (RR) shocks for the various modeled vehicle velocities and road profiles are provided in the Appendix A. The average instantaneous power dissipated by each of the shocks on a single pass of each road surface modeled is summarized below in Table 5. Likewise, the recoverable energy from each of the shocks on a single pass of each road surface modeled is summarized in Table 6. Using this information in conjunction with the total number of passes on each road surface necessary to cover the modeled drive cycle from Table 3, the total recoverable energy for the entire trip can be determined.

Table 5. Average Instantaneous Power (W) for Single Pass of Modeled Road Surfaces

	Brushed Concrete @ 30mph	Brushed Concrete @ 50mph	Brushed Concrete @ 70mph	Coarse Road@ 30mph	FEC Ride Road @ 50mph	DeSoto Road @ 40mph
LF	3.42	9.05	20.13	1.59	43.17	28.33
RF	2.74	9.63	19.66	1.33	41.50	30.25
LR	2.97	9.83	17.37	1.03	34.77	25.51
RR	1.65	6.07	12.65	1.06	33.18	29.41
Total	10.79	34.57	69.81	5.02	152.63	113.51

Table 6. Recoverable Energy (Wh) per Pass of Modeled Road Surfaces

	Brushed Concrete @ 30mph	Brushed Concrete @ 50mph	Brushed Concrete @ 70mph	Coarse Road@ 30mph	FEC Ride Road @ 50mph	DeSoto Road @ 40mph
LF	0.024	0.038	0.062	0.017	0.289	0.24
RF	0.019	0.040	0.060	0.014	0.28	0.25
LR	0.021	0.041	0.053	0.011	0.23	0.21
RR	0.012	0.025	0.039	0.011	0.22	0.25
Total	0.075	0.15	0.21	0.053	1.02	0.95

The total recoverable energy for the entire trip is equal to the summation of the product of the total recoverable energies on each road surface and the total number of passes required on each respective road surface. The tabulation of the total energy recoverable on each road surface for the modeled drive cycle is carried out in Table 7. The total energy recoverable by all four shocks for the modeled drive cycle is then the summation of each of the total energies recoverable on each road surface, or 25.41 Wh.

Table 7. Total Energy Recoverable on Each Road Surface for Modeled Drive Cycle

	Brushed Concrete @ 30mph	Brushed Concrete @ 50mph	Brushed Concrete @ 70mph	Coarse Road @ 30mph	DeSoto Road @ 40mph
# of Passes	48	57	47	13	3
Energy/ Pass (Wh)	0.075	0.14	0.21	0.053	0.95
Total Energy (Wh)	3.60	8.24	10.04	0.69	2.84

Since 25.41 Wh only represents 0.3% of the daily energy goal of 7.6 kWh it is safe to make the conclusion that for a typical daily trip length over a typical drive cycle regenerative shock absorbers, when applied to a C-MAX, do not possess the capability of making any significant energy contributions to the daily energy goal, and therefore will not be investigated further.

CHAPTER 5: SOLAR POWER

5.1 Technology Overview

Photovoltaics (PV) are used to directly convert incident solar radiation into electricity. This is achieved through the use of semi-conductors, or more specifically a p-n junction. When photons of a specific energy are absorbed by the semi-conductor material, an electron-hole pair is created. The energy of the photon required for the generation of an electron-hole pair is dependent on the band gap of the semi-conductor material. Photons with an energy greater than or equal to the band gap energy will be absorbed by the material and create an electron-hole pair. Photons with an energy less than the band gap energy will not be absorbed by the semi-conductor and will pass through the material. Finally, photons with an energy much greater than the band gap energy will be absorbed by the material, but will only contribute to heating the material. When an electron-hole pair is created, the p-n junction serves to keep the electron and hole separated by means of an electric field.

Under open circuit conditions, light-generated electron-hole pairs, or carriers begin to accumulate in the material, with electrons accumulating in the n-type junction and holes accumulating in the p-type junction. This accumulation generates an electric field opposite to that of the p-n junction, while at the same time generating an electric potential difference across the junction. The reduction in electric field across the junction allows for the forward bias diffusion current of the junction to flow more easily, and an equilibrium is reached where the light induced current is equal to the forward bias diffusion current. If the circuit is closed, carriers again begin to accumulate on either side of the junction, and the light-generated carriers flow through the external circuit. The current through the external circuit is then proportional to the intensity of light incident on the cell. For an extensive overview of solar power generation using PV see reference (Singh 2013).

5.2 Types of Photovoltaics

Considerable work is being done to advance PV technologies in the areas of material selection, material design, and manufacturing techniques. Today, there are numerous types of PV technologies available, of which, these can be divided into four main categories; namely:

- Crystalline Silicon Cells
- Thin-Film Technologies
- Multi-Junction Cells
- Emerging Technologies

Figure 19 depicts a recent history of best research-cell efficiencies for each of the PV technology categories. The figure shows that crystalline silicon cells have attained efficiencies as high as 27.6%, thin-film technologies have attained efficiencies as high as 20.3%, multi-junction cells have attained efficiencies as high as 43.5%, and emerging PV technologies have attained efficiencies as high as 11.4% (Kurtz 2012).

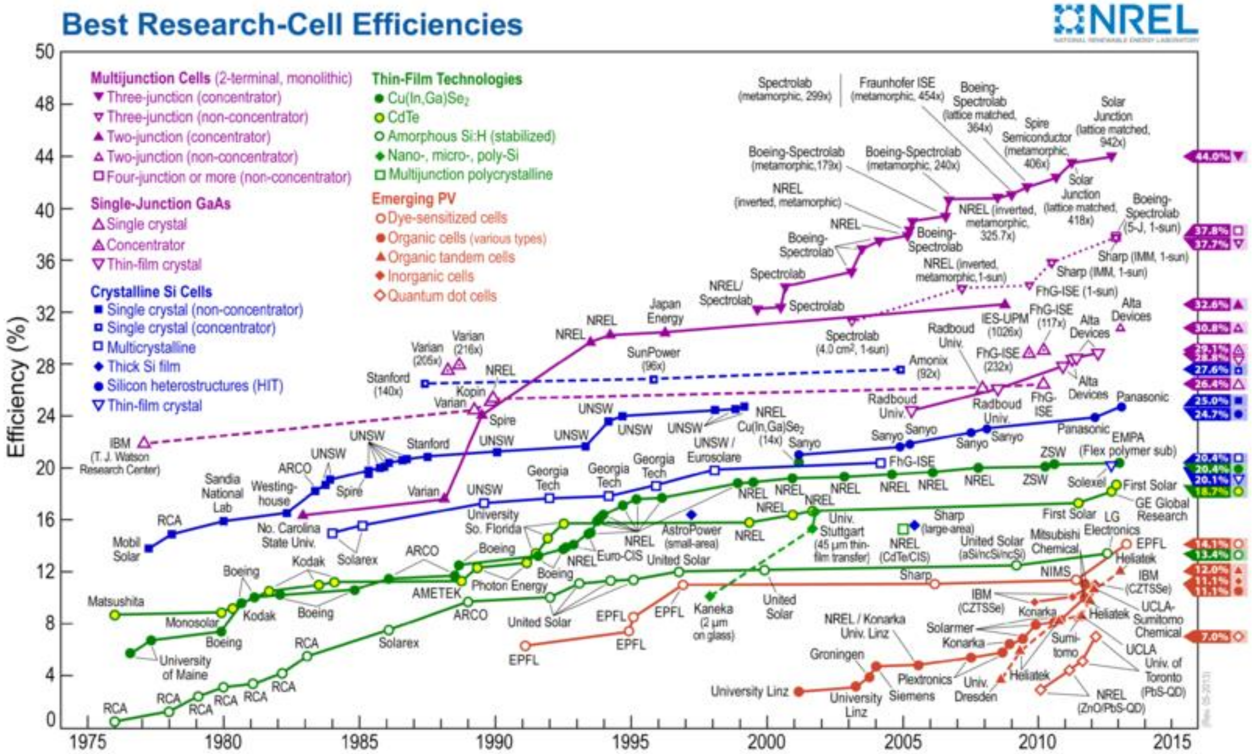

Figure 19.Best Research-Cell Efficiencies (Kurtz 2012)

Crystalline silicon cells can be further divided into monocrystalline silicon cells and polycrystalline silicon cells. Monocrystalline cells tend to be more expensive due to the difficulty of the manufacturing process required to produce them. The cost is not without reward however, as the efficiency of monocrystalline cells is high. Premium commercially available cells can have efficiencies of 23%. These same cells also have a low temperature coefficient, with a reduction in power of 0.3% for every degree Celsius above 25°C. Due to the high cost of monocrystalline PV cells, their application is best suited when the maximum power per unit area is desired. Polycrystalline PV cells are generally less expensive than monocrystalline PV cells due to the less complicated manufacturing process required in producing them. Typical efficiencies of commercially available polycrystalline PV cells range from 13 – 15%, with premium cells being as high as 17%. The temperature coefficient of these cells is typically on the order of 0.4-0.5%/°C (Kalogirou 2014).

Thin-Film PV encompasses a broad spectrum of technologies; including but not limited to, amorphous silicon, Cadmium Telluride, and Copper Indium Gallium Selenide. Amorphous silicon cells are easy to manufacture, as such they have a low associated cost. The typical efficiency of amorphous silicon cells is only 6 -7 %, but the temperature coefficient is very low at -0.2%/°C. Additionally, amorphous silicon cells are capable of better absorbing wavelengths in the blue portion of the spectrum, allowing for better performance in cloudy conditions (Kalogirou 2014). Other predominant thin-film technologies have similarly low cost and temperature coefficients, as well as low efficiencies – on the order of 10% (Kalogirou 2014).

Multi-junction cells consist of multiple layers of semi-conductor material each with a band gap optimized to capture a specific portion of the solar spectrum. The materials with the highest band gap are placed in the uppermost layers, so as to allow photons with an energy lower than the band gap to pass through to the lower layers. The efficiencies of such cells are on the order of 30 – 40%; however, due to their prohibitively high cost, they are generally only used in high concentration PV systems. Concentrating PV systems will be discussed in greater detail later in this paper. Finally, emerging PV technologies generally include PV technologies made from organic materials and also those technologies utilizing environmentally friendly manufacturing techniques. The majority of these technologies are only produced in laboratories and generally have very low efficiencies.

The focus of this investigation will be on monocrystalline PV. As previously stated, premium commercially available cells can have efficiencies of 23%, and are best suited for applications where the maximum power per unit area is desired. Many efforts are being made to increase the efficiency of monocrystalline PV. One such initiative is that of the U.S. Department of Energy, known as the SunShot Initiative. The program provides support for collaborative research efforts working towards advancing the cell efficiency of monocrystalline PV. Research groups under the initiative are striving to reach cell efficiencies of 26.5 – 29% (DOE 2014).

5.3 Modeling One Sun PV Panel Production

A Matlab function, UnitPanelProduction.m was written to calculate the energy generated by a 1 square meter PV panel given the following input conditions:

- Time of year (Month)
- GPS location (City)
- PV efficiency (PVEff)
- Azimuth of PV panel face (PVDirection)
- Angle of PV panel from horizontal (PVAngle)

The function begins by loading the GPS data for the selected city and the weather data for the selected city and month. The weather data is a typical meteorological year (TMY) data file which is used to determine the typical solar resource available at a given location at a given time of year. TMY data will be discussed in greater detail in the following section. The GPS and weather data are used by solar.m to determine the radiative flux incident on a 1 square meter panel oriented at the azimuth angle specified by ‘PVDirection’ in degrees from north and at an angle from horizontal specified by ‘PVAngle’. The determination of the radiative flux incident on an inclined surface will be discussed in a later section. The Matlab function right_hand_side.m then uses the radiative flux incident on the PV panel to determine the energy generated by the panel over the desired time step using the input PV efficiency and an additional assumed wiring efficiency of 93%. Finally, sim_steps.m is used to size the output 'EnergyMap' which contains the energy at each time step of each day for the selected month. The function structure including inputs to the main function, the main function output, data files called, and sub-functions called is illustrated in Figure 20.

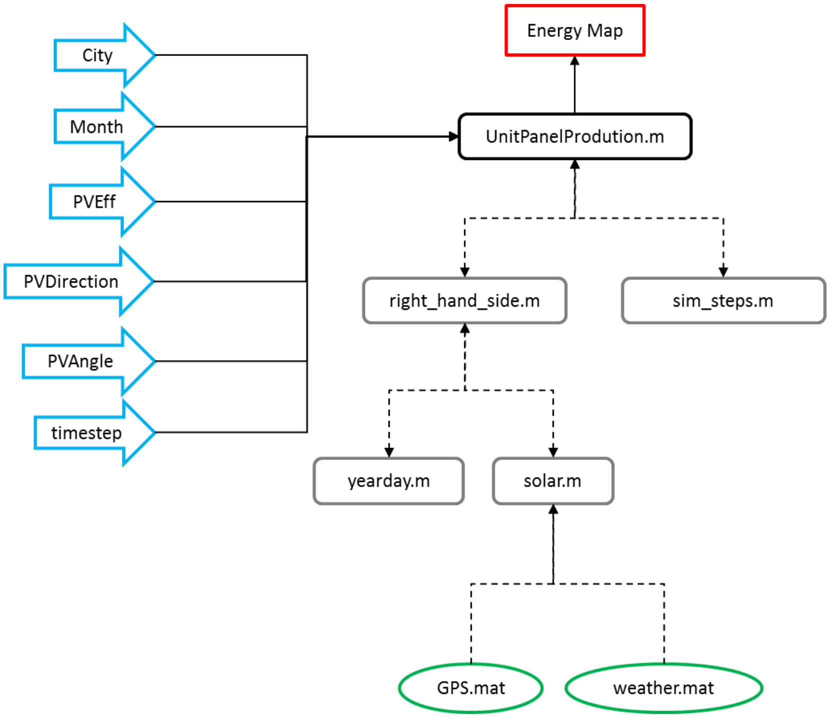

Figure 20. One Sun Matlab Model Code Structure

5.4 TMY Data

The TMY data set provides a long term characterization of particular meteorological values at a specific location at an hourly temporal resolution. This data is commonly used in modeling renewable energy conversion systems, and in particular – solar energy systems. The TMY data set was originally developed in 1978 by Sandia National Laboratories using long-term weather and solar data collected at 248 locations across the U.S. over the period of 1952-1975. The TMY data set has since been updated twice to now include data collected at 1400+ locations over the period of 1976-2005. This most up to date TMY is referred to as the TMY3 data set. To generate the TMY, an empirical method, known as the Sandia Method, is used to select the most typical months in the data set for each month of the year. The methodology in selecting the most typical months is described below; taken from chapter 2.1 of the User's Manual for TMY3 Data Sets (Wilcox 2008)

The Sandia method selects a typical month based on nine daily indices consisting of the maximum, minimum, and mean dry bulb and dew point temperatures; the maximum and mean wind velocity; and the total global horizontal solar radiation. Final selection of a month includes consideration of the monthly mean and median and the persistence of weather patterns. The process may be considered a series of steps.

Step 1 - For each month of the calendar year, five candidate months with cumulative distribution functions (CDFs) for the daily indices that are closest to the long-term (30 years for the NSRDB) CDFs are selected. The CDF gives the frequency of occurrence of values that are less than or equal to a specified value of an index. Candidate monthly CDFs are compared to the long-term CDFs by using the following Finkelstein- Schafer (FS) statistics (Finkelstein and Schafer 1971) for each index.

$$FS = \frac{1}{n}\sum_{i=1}^{n} \Delta CDF_i \tag{6}$$

where ΔCDF_i is the absolute difference between the long-term CDF and the candidate month CDF and n is the number of daily readings in a month. Because some of the indices are judged more important than others, a weighted sum (WS) of the FS statistics is used to select the five candidate months that have the lowest weighted sums.

$$WS = \sum w_i FS_i \tag{7}$$

where w_i is the weighting for index and FS_i is the FS statistic for index. Weighting values for the FS statistics are shown in the table below.

Table 8. Weighting Values for FS Statistics (Wilcox 2008)

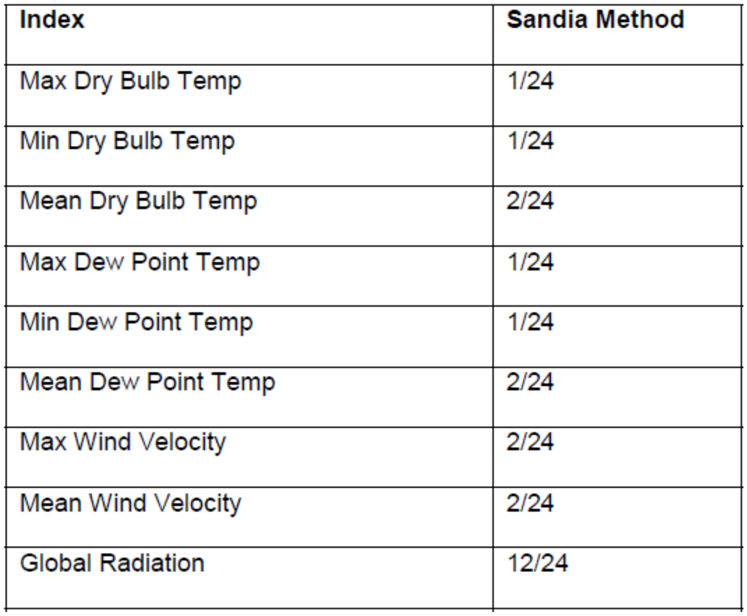

Index	**Sandia Method**
Max Dry Bulb Temp	1/24
Min Dry Bulb Temp	1/24
Mean Dry Bulb Temp	2/24
Max Dew Point Temp	1/24
Min Dew Point Temp	1/24
Mean Dew Point Temp	2/24
Max Wind Velocity	2/24
Mean Wind Velocity	2/24
Global Radiation	12/24

Step 2 - The five candidate months are ranked with respect to closeness of the month to the long-term mean and median.

Step 3 - The persistence of mean dry bulb temperature and daily global horizontal radiation are evaluated by determining the frequency and length of runs of consecutive days with values above and below fixed long-term percentiles. For mean daily dry bulb temperature, runs above the 67th percentile (consecutive warm days) and below the 33rd percentile (consecutive cool days) were determined. For global horizontal radiation, the runs below the 33rd percentile (consecutive low radiation days) were determined. The persistence criteria excludes the month with the longest run, the month with the most runs, and the month with zero runs. The persistence data are used to select from the five candidate months the month to be used in the TMY. The highest-ranked candidate month from Step 2 that meets the persistence criteria is used in the TMY.

Step 4 - The 12 selected months were concatenated to make a complete year and discontinuities at the month interfaces were smoothed for 6 hours each side using curve fitting techniques.

By selecting the months with CDFs most similar to the long term CDF, the ‘typical’ or long-term behavior of a particular location is captured. In doing so, the extreme cases at a particular location are not reflected in the TMY data set. As such, in using the TMY data set to model the expected energy production of a concentrated solar power system, the modeled energy production will be what can be expected as ‘typical’ over the 10+ year life of the vehicle. If extreme cases or worst-case scenarios are to be considered, other means of modeling a location’s irradiance will need to be implemented.

5.5 One Sun Model Results

The one sun vehicle tests were conducted in Atlanta, Georgia during the months of June and July. For the one sun vehicle tests, three 0.4 square meter PV panels with a rated efficiency of 23% were fixed to the roof of a vehicle, and the vehicle was parked in full sunlight over four test periods of one day each. Further details regarding the one sun vehicle tests are discussed in the following sections. Prior to running the one sun vehicle tests, the Matlab model UnitPanelProduction.m was run to determine the expected daily energy generation of the individual panels. In order to as closely represent the actual test conditions as possible, the model was run with the following conditions as inputs:

- Month: June and July
- City: Atlanta, GA
- PVEff: 21.5%
- PVDirection: N/A (horizontal flat plate)
- PVAngle: 0°

Although the roof mounted PV panels actually have a slight 2-D curvature, for the purposes of modeling, the panels will be treated as horizontal flat plate collectors. The modeled panel efficiency was lowered from the rated panel efficiency of 23% to account for a small thermal derate during operation. The wiring efficiency is a conservative estimate recommended by an expert at a leading PV manufacturer.

The model was run for each month with a time step of 5 minutes. Since the model is designed to calculate the energy generated by a one square meter panel, the energy at each time step was scaled to the area of the actual panel, 0.4 square meters, by multiplying each energy value by 0.4. The daily energy generation values for each day of each month, as predicted by the Matlab model, were then used to produce the daily energy generation CDFs depicted in Figure 21 and Figure 22. As shown in Figure 21 and Figure 22, the expected daily energy generation range and average are very similar for the months of June and July. On average, approximately

0.5 kWh per panel can be expected in the months of June and July. A typical high-end daily energy generation may be near 0.6 kWh and a typical low-end daily energy value may be near 0.2 kWh. Again, since the model relies of TMY data to generate these values, the range does not reflect actual extremes, but rather what may be considered as typical over a long period of time.

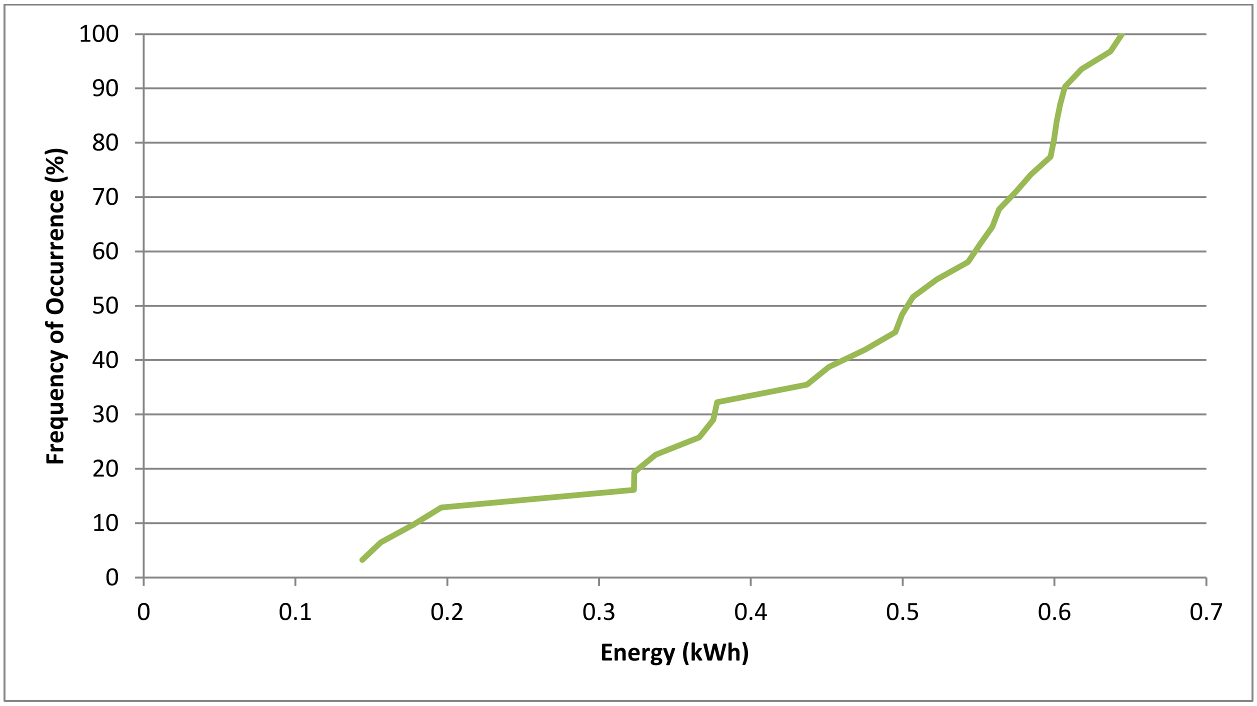

Figure 21. Modeled Energy Generation CDF for June in Atlanta

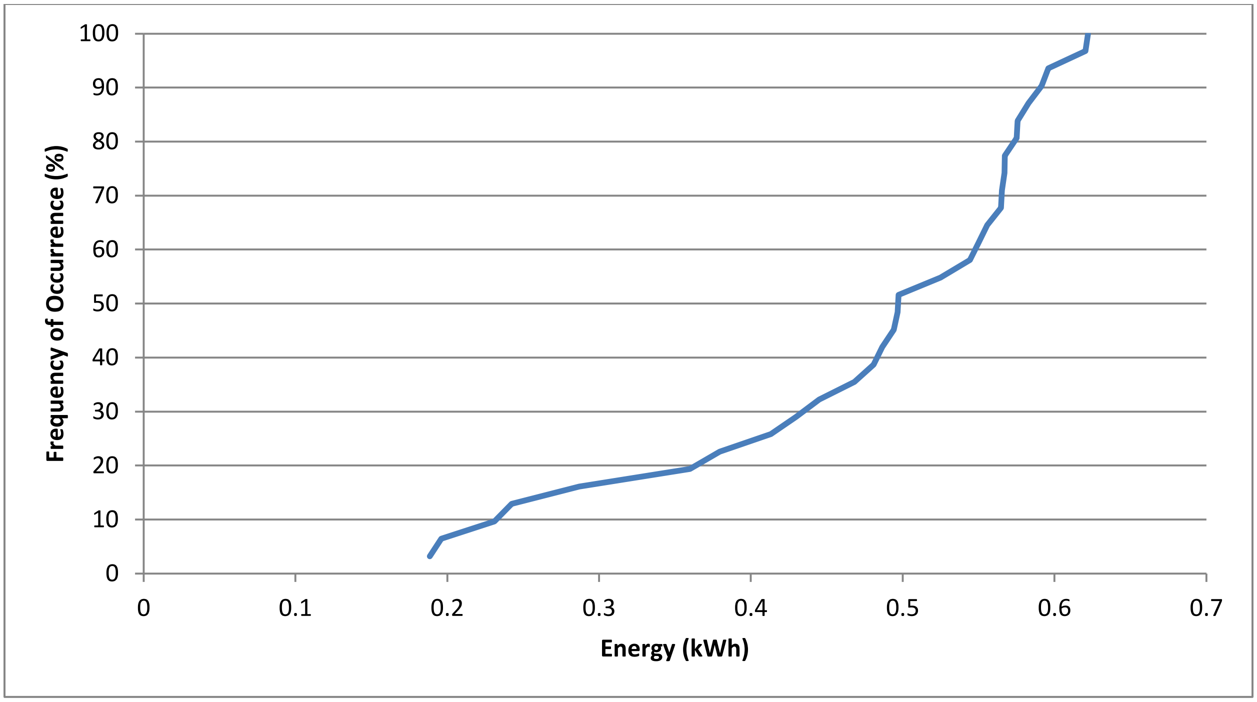

Figure 22. Modeled Energy Generation CDF for July in Atlanta

5.6 One Sun Testing Apparatus and Procedure

For the one sun testing a vehicle with three roof-mounted PV panels, as shown in Figure 23, was parked 9:00 AM to 5:00 PM in a location that would receive full and uninterrupted sunlight throughout the day. As shown in Figure 24, the PV panels were wired independently to three separate Phocos CIS-MPPT (20A) Industrial Solar Charge Controllers, and used to charge a 12V battery bank consisting of 3 Leoch LPG12-100 12V 96Ah Batteries connected in parallel. The voltage of the PV panels was logged at one minute intervals using a Lascar EL-USB-3 Voltage USB Data Logger with a measurement range of 0 to 30 VDC, an internal resolution of 50 mV, and an accuracy of plus or minus 1 percent. The current of the PV panels was measured using an Extech Instruments Model CA250 400A AC/DC Current Clamp-on Multi-meter Adaptor with an output of 10mV/Amp on the 0 to 40A range and with an accuracy of plus or minus 2.5 percent plus 0.1 A. Current measurements were logged at one minute intervals using a Lascar EL-USB-ACT Current/Voltage Data Logger with a range of 0 to 1000 mVDC, a measurement resolution of 250μV, and an accuracy of 2 percent. Global horizontal irradiance was measured at 15 minute intervals using an Eppley Precision Pyranometer.

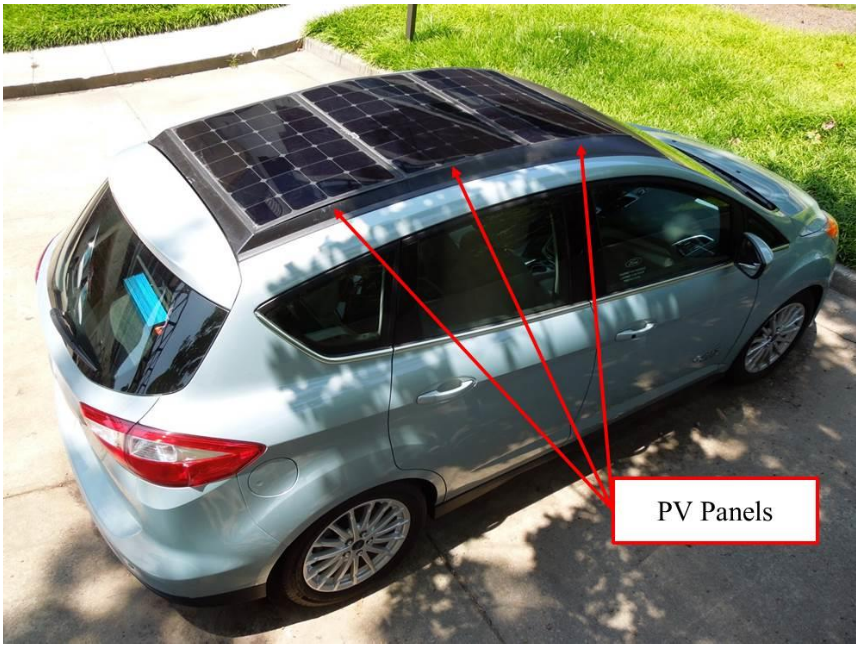

Figure 23. Vehicle with Three Roof-Mounted PV Panels

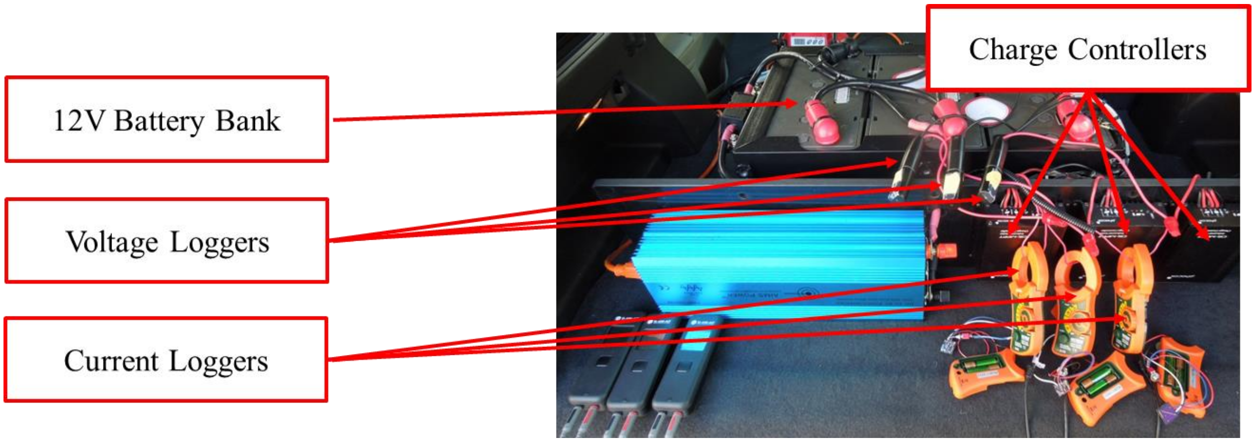

Figure 24. One Sun Testing Apparatus

5.7 One Sun Testing Results and Discussion

The current and voltage measurements were used to calculate the instantaneous power, P_i, in Watts, at time step, i, using the following equation

$$P_i = I_i V_i \tag{8}$$

Here, I_i is the current, in Amps, at time step i and V_i is the voltage, in Volts at time step i. The instantaneous power is plotted with respect to time for panels 1, 2, and 3 with the rear of the vehicle facing north in Figure 25, Figure 26, and Figure 27 respectively. Using the instantaneous power, the energy in Watt-hours captured by the panels during the test period can be calculated as

$$\frac{\sum_{i=1}^{n} P_i \, \Delta t}{60 \text{ min/hr}} \tag{9}$$

where Δt is the time step, 1 minute in the case of this experiment. For the test conducted with the rear of the vehicle facing north, 509.2Wh, 482.1Wh, and 485.3Wh were generated over the period of 9:00 – 17:15 by panels 1, 2, and 3 respectively. Instantaneous power figures for the remainder of the one sun testing are provided in Appendix B, and the energy captured by each of the panels during the remainder of the one sun tests is summarized in Table 9.

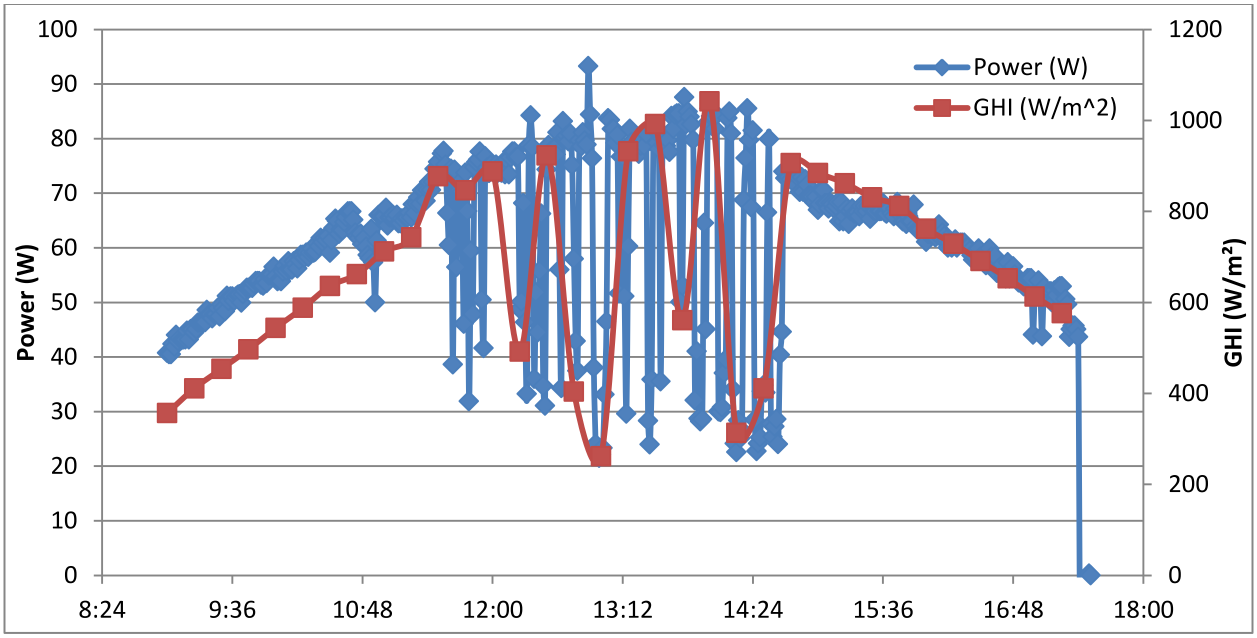

Figure 25. Instantaneous Power and GHI Incident on Panel 1 for Rear of Vehicle Facing North

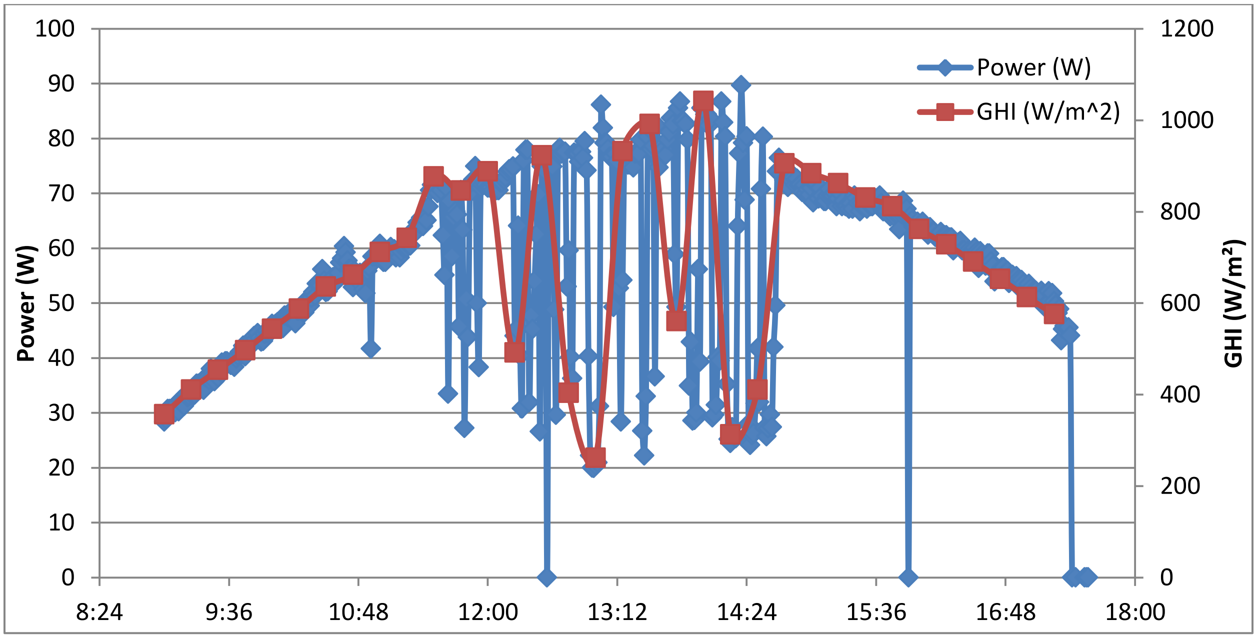

Figure 26. Instantaneous Power and GHI Incident on Panel 2 for Rear of Vehicle Facing North

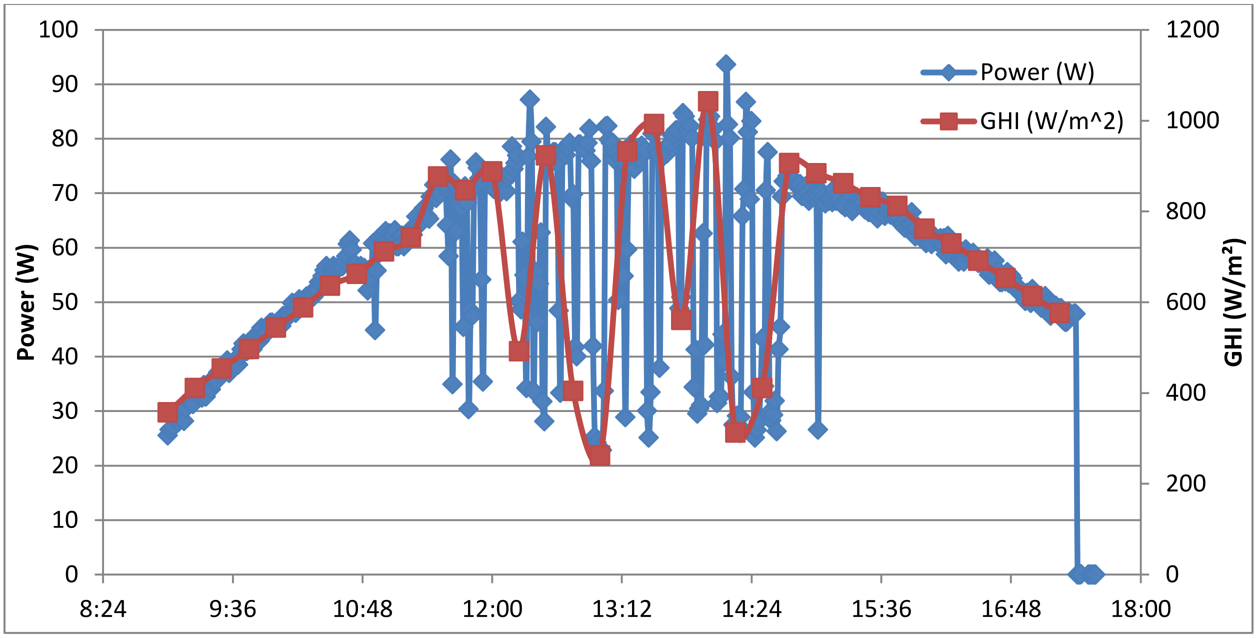

Figure 27. Instantaneous Power and GHI Incident on Panel 3 for Rear of Vehicle Facing North

Also included in the instantaneous power figures is the solar resource available to the panels during the test period, in terms of GHI measured in Watts per meter squared. As previously mentioned, the PV panels are assumed to be horizontal flat plate collectors. In making this assumption, the operating efficiency of the panels can be determined by dividing the instantaneous power at a given time step by the solar power incident on a horizontal flat plate at the same time step. The GHI can be used to determine the solar power incident on a horizontal flat plate by multiplying the GHI by the area of the solar panel in meters squared, or $0.4m^2$. The calculated operating efficiencies for panels 1, 2, and 3 with the rear of the vehicle facing north are plotted in Figure 28. Efficiency figures for the remainder of the one sun testing are provided in Appendix B, and the average efficiency of the panels during the remainder of the one sun tests is summarized in Table 9.

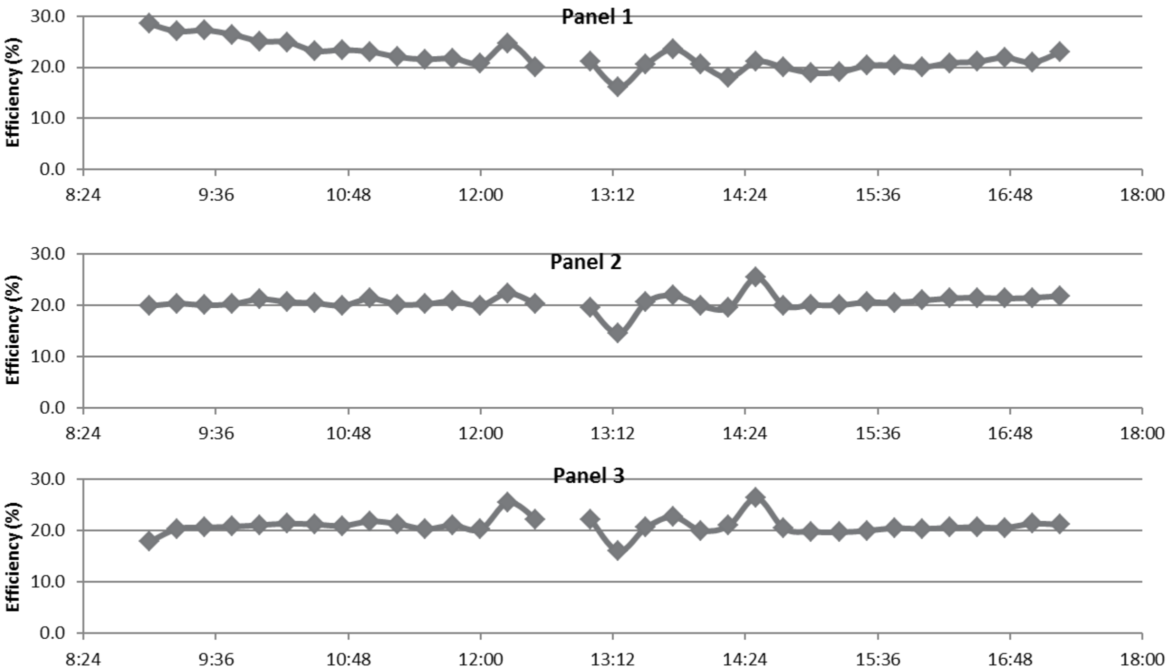

Figure 28. Experimental Panel Efficiencies for Rear of Vehicle Facing North

Table 9. Summary of One Sun Orientation Testing Results

	Panel 1	**Panel 2**	**Panel 3**	**Summary**
North	Energy: 0.509 kWh Insolation: 2771.6 W/m²/Test Full Day Energy: 0.613 kWh	Energy: 0.482 kWh Insolation: 2771.6 W/m²/Test Full Day Energy: 0.581 kWh	Energy: 0.485 kWh Insolation: 2771.6 W/m²/Test Full Day Energy: 0.584 kWh	Avg. Efficiency: 21.2% Model Efficiency: 19.995% 83% of Solar Resource during Test
South	Energy: 0.326 kWh Insolation: 2593.9 W/m²/Test Full Day Energy: 0.441 kWh	Energy: 0.343 kWh Insolation: 2593.9 W/m²/Test Full Day Energy: 0.464 kWh	Energy: 0.370 kWh Insolation: 2593.9 W/m²/Test Full Day Energy: 0.5 kWh	Avg. Efficiency: 19.2% Model Efficiency: 19.995% 74% of Solar Resource during Test
East	Energy: 0.478 kWh Insolation: 3073.6 W/m²/Test Full Day Energy: 0.569 kWh	Energy: 0.499 kWh Insolation: 3073.6 W/m²/Test Full Day Energy: 0.594 kWh	Energy: 0.499 kWh Insolation: 3073.6 W/m²/Test Full Day Energy: 0.594 kWh	Avg. Efficiency: 21.5% Model Efficiency: 19.995% 84% of Solar Resource during Test
West	Energy: 0.338 kWh Insolation: 2335.6 W/m²/Test Full Day Energy: 0.428 kWh	Energy: 0.309 kWh Insolation: 2335.6 W/m²/Test Full Day Energy: 0.391 kWh	Energy: 0.341 kWh Insolation: 2335.6 W/m²/Test Full Day Energy: 0.432 kWh	Avg. Efficiency: 20.1% Model Efficiency: 19.995% 79% of Solar Resource during Test

The ‘Full Day Energy’ value shown in Table 9 is the energy that could be expected of the PV panel based upon the energy actually collected by the panel over the test period and the percentage of the daily insolation available during the test period. As shown in Figure 29, the percentage of the daily insolation available during the test period was determined by comparing the GHI that was available during the test period to the GHI that was available over the entire day. For the test day shown in Figure 29, 83% of the daily insolation was captured during the test period. Assuming that the average panel efficiency remains constant, the energy that could be expected of the PV panel over the entire day is then equal to the actual energy collected by the panel over the test period divided by the percentage of the daily insolation available during the test period. An example of this calculation is shown below for panel 1 and the rear of the vehicle facing north

$$Full\ Day\ Energy = \frac{Actual\ Energy}{\%\ Solar\ Resource\ During\ Test} = \frac{0.509\text{kWh}}{0.83} = 0.613\text{kWh}$$

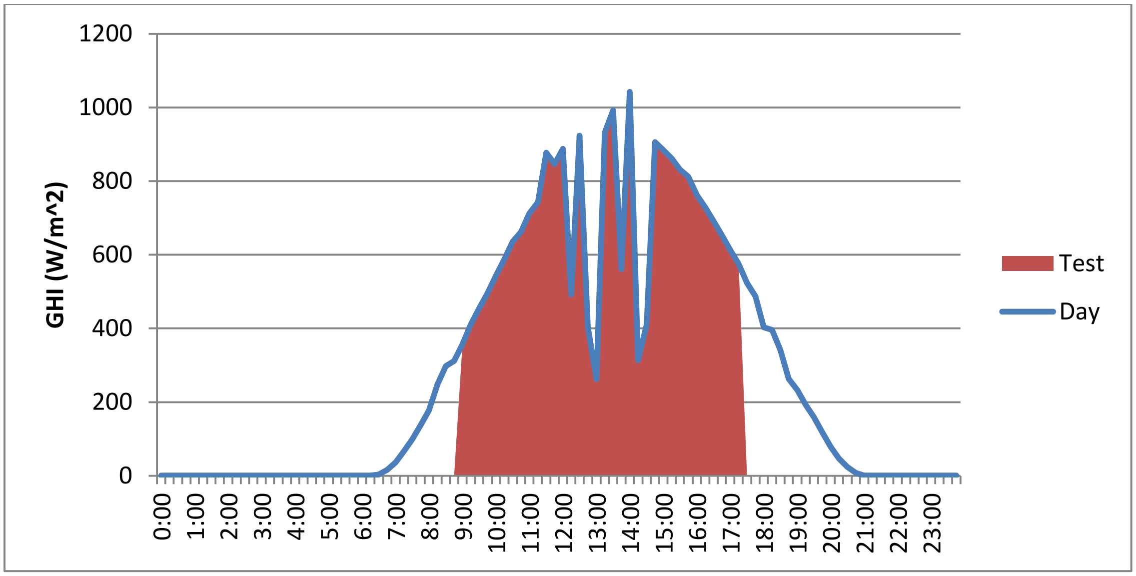

Figure 29. GHI Available During Test with Respect to GHI Available over Entire Day for Rear of Vehicle Facing North

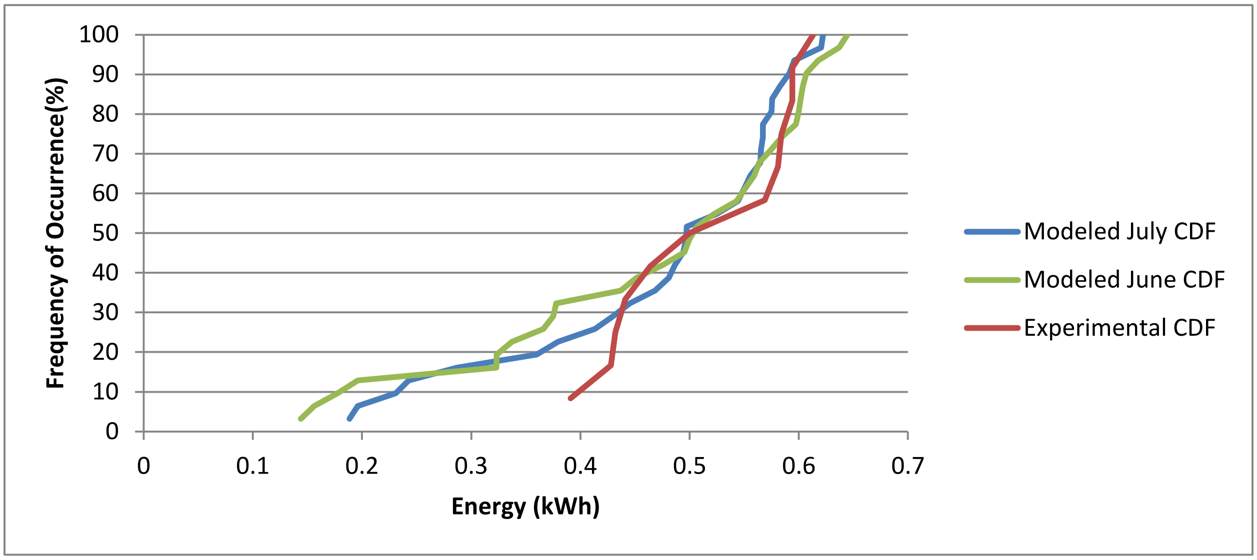

Figure 30. Comparison of Experimental and Modeled Daily Energy CDFs

The full day energy values for each of the panels and each of the test scenarios shown in Table 9 were then used to generate the experimental CDF shown in Figure 30. The experimental daily energy CDF is plotted alongside the modeled daily energy CDF for June and July, as the tests were conducted in the months of June and July. As shown in the figure, for all values above 50% frequency of occurrence, the experimental and modeled CDFs correlate very well with one another. The modeled daily energy for the month of June is distributed around 1.51 kWh, with approximately 59% of the data lying above the average of 1.40 kWh. The modeled daily energy for the month of July is distributed around 1.49 kWh, with approximately 63% of the data lying above the average of 1.42 kWh. The experimental daily energy for tests run in June and July is distributed around 1.5 kWh, with approximately 52% of the data lying above the average of 1.55 kWh.

The deviation on the low-end daily energy values is due to the testing requirements of the vehicle. As of yet, the vehicle has not been fully waterproofed, and as a result testing could not be performed in rainy weather or if there was a significant chance of rain. As a result of testing in only fair weather or partly cloudy conditions, the experimental CDF demonstrates higher low-end daily energy values. This being taken into consideration, it can be said that the modeled results and experimental results are in good agreement. Since the model is based on TMY data, the expected energy generation for different months of the year and locations across the nation may then be assessed using the U.S. Solar Radiation Resource maps provided by the National Renewable Energy Laboratory, which are also based on TMY data (NREL 1992).

A final aspect to be taken into consideration is the energy requirement due to the effect of the added mass of the PV array. Each of the PV panels used on the vehicle weighs 3.0 lbs, or 1.4 kg, with encapsulation. There are three PV panels on the roof of the vehicle, which equates to 9lbs, or 4.1 kg. The Phocos MPPT industrial charge controller weighs 1.1 kg, bringing the total weight of the system to approximately 5 kg. The weight of the batteries is neglected, as in a real system the panels would be used to charge the pre-existing vehicle battery. In the study conducted in Chapter 3 on the effect of adding mass to the vehicle it was determined that a 5 kg mass would require 7.1-26.3 Wh for a typical drivers' daily trips. The high end daily energy requirement of the additional 5 kg mass only accounts for 1.7% of the average experimental daily energy that was generated in the months of June and July.

5.8 Covering Additional C-MAX Body Panels in PV

The large body panels of the C-MAX's exterior represent a large surface area that could potentially be used to capture energy from incident solar radiation. It has already been shown that three 0.4 square meter PV panels on the roof of the C-MAX are capable of generating on average 0.5 kWh each per day or 1.5 kWh total per day during the summer in Atlanta, Georgia. By utilizing the area of additional large body panels, the potential energy recoverable may be considerably higher. For this reason, a model was developed to determine the energy produced by a C-MAX with the following body panels covered in PV:

- Rear doors
- Front doors
- Hood
- Windshield.

Obviously, the windshield cannot be covered while the vehicle is being driven; however, recent studies of C-MAX driving behavior have indicated that average drivers spend only 10% of the day driving (Boston 2014). If it is assumed that drivers will do their best to park the vehicle in full sunlight for the remaining 90% of the day, and that a deployable PV array to cover the windshield while parked could be developed, there is still a considerable amount of energy that could be captured.

Measurements were taken by hand in order to determine the approximate surface areas of each of the body panels to be modeled. In calculating the surface areas, some simplifications were made to account for some of the more complex geometries. As shown in Figure 31, the area of the hood was approximated as a trapezoid, using the width of the hood at the front of the car, the width of the hood at the rear of the hood, and the length of the hood along the length of the vehicle to calculate the area.

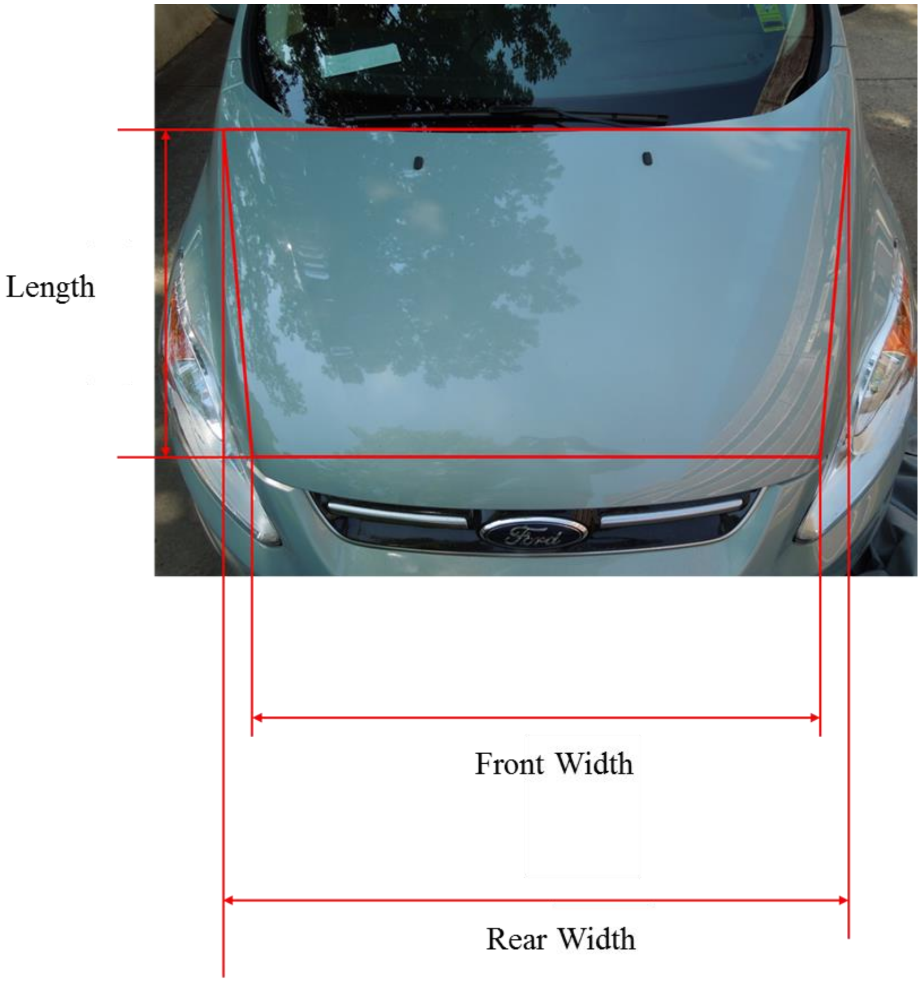

Figure 31. Hood Area Approximation

As shown in Figure 32, the area of the rear door was approximated as a rectangle using the smallest dimension at the base of the door and the height of the door as the width and height of the rectangle respectively.

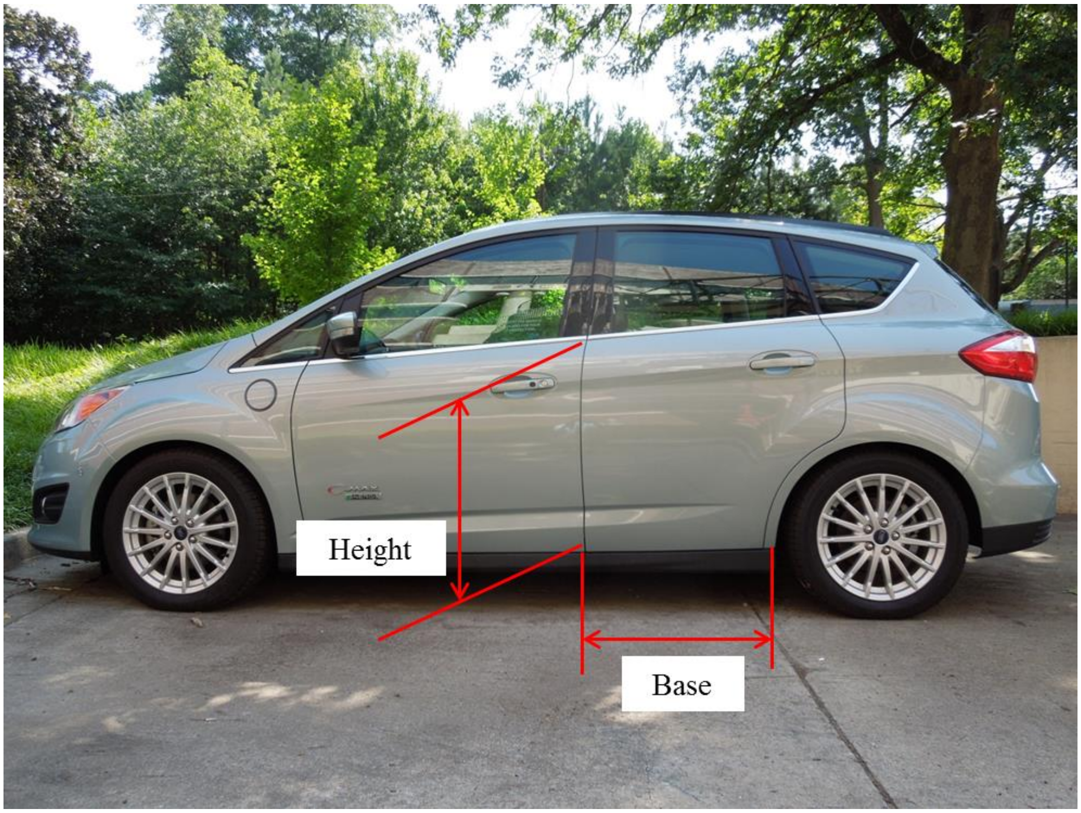

Figure 32. Rear Door Area Approximation

All other areas were approximated as rectangles using the smallest measured dimensions for length and width to allow for a conservative estimate. The approximate surface areas of each of the body panels to be modeled are as follows:

- Rear doors: 0.53 m^2 each
- Front doors: 0.84 m^2 each
- Hood: 0.92 m^2
- Windshield: 1.21 m^2.

In addition, the doors, hood, and windshield are to be modeled as flat plates oriented at 90°, 10°, and 30° from horizontal, respectively.

5.9 Modeling Additional C-MAX Body Panels Covered in PV

A Matlab function, VehicleAnalysis.m was written to calculate the energy generated by each of the body panels given their respective sizes and orientations. This is accomplished using the UnitPanelProduction.m file discussed earlier, and a matrix, ‘CMAX.mat’ which characterizes each of the body panels to be modeled. The ‘CMAX.mat’ file contains the areas and orientations from horizontal discussed in the previous section, as well as the azimuth angle of each of the body panels with the front of the car facing north and the efficiency of the PV to be mounted on each of the body panels. As with the UnitPanelProduction.m function, the VehicleAnalysis.m function can be run for any city in the database, and for any month and vehicle direction. The vehicle direction is the direction that the front of the vehicle is facing in degrees from north, and changing the vehicle direction automatically applies the appropriate rotation to the azimuth angles of each of the body panels in the characterization matrix ‘CMAX.mat’.

5.10 Results and Discussion

5.10.1 The Daily Energy Generation of Additional Body Panels Covered in PV for Atlanta, GA

To better understand the magnitude of the difference in daily energy generation when covering additional body panels in PV, the model was run first using the same inputs as the one sun analysis of just the roof covered in PV. The model inputs are as follows:

- Month: July
- City: Atlanta, GA
- PV Efficiency: 21.5%

As discussed in the previous section, the angle of the PV from horizontal is dependent on the particular body panel, and the angle of each PV in the model was set accordingly. The hood and windshield of the C-MAX represent the largest and nearest to horizontal body panels, aside from the roof, and as a result, all models in this analysis were run with the front of the vehicle facing south. An angled PV panel in the northern hemisphere will generate the maximum year-round energy when facing in a southwardly direction (Stanciu and Stanciu 2014). Therefore, the largest body panels, the hood and windshield, should be facing south to maximize PV energy generation. As with the previous one sun analysis, the model was run with a time step of 5 minutes, and the energy generation at each time step was scaled to the area of the respective body panel. The daily energy generation values for each body panel were then used to produce the daily energy generation CDFs depicted in Figure 33.

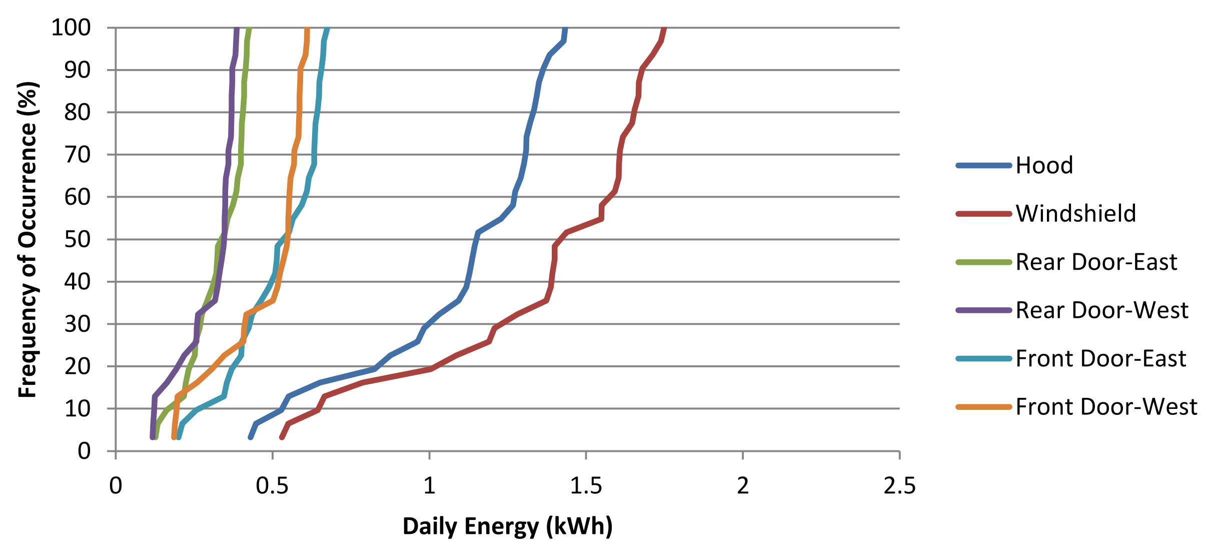

Figure 33. Daily Energy CDFs of Modeled Body Panels for July in Atlanta, GA

As shown in the figure, the daily energy generation for the hood is distributed around 1.15 kWh, with approximately 64% of the data lying above the average of 1.10 kWh. The daily energy generation of the windshield is distributed around 1.42 kWh, with approximately 65% of the data lying above the average of 1.35 kWh. The daily energy generation for the eastwardly facing rear door is distributed around 0.34 kWh, with approximately 53% of the data lying above the average of 0.32 kWh. The daily energy generation for the westward facing rear door is distributed around 0.35 kWh, with approximately 65% of the data lying above the average of 0.30 kWh. The daily energy generation of the eastwardly facing front door is distributed around 0.53 kWh, with approximately 53% of the data lying above the average of 0.51 kWh. And the daily energy generation of the westward facing front door is distributed around 0.55 kWh, with approximately 65% of the data lying above the average of 0.48 kWh.

To get a better idea of the year-round energy generation by the additional panels in Atlanta, the same analysis was conducted for the months of January and October. The daily energy generation CDF's for each of the body panels in the months of January and October are shown in Figure 34 and Figure 35, respectively.

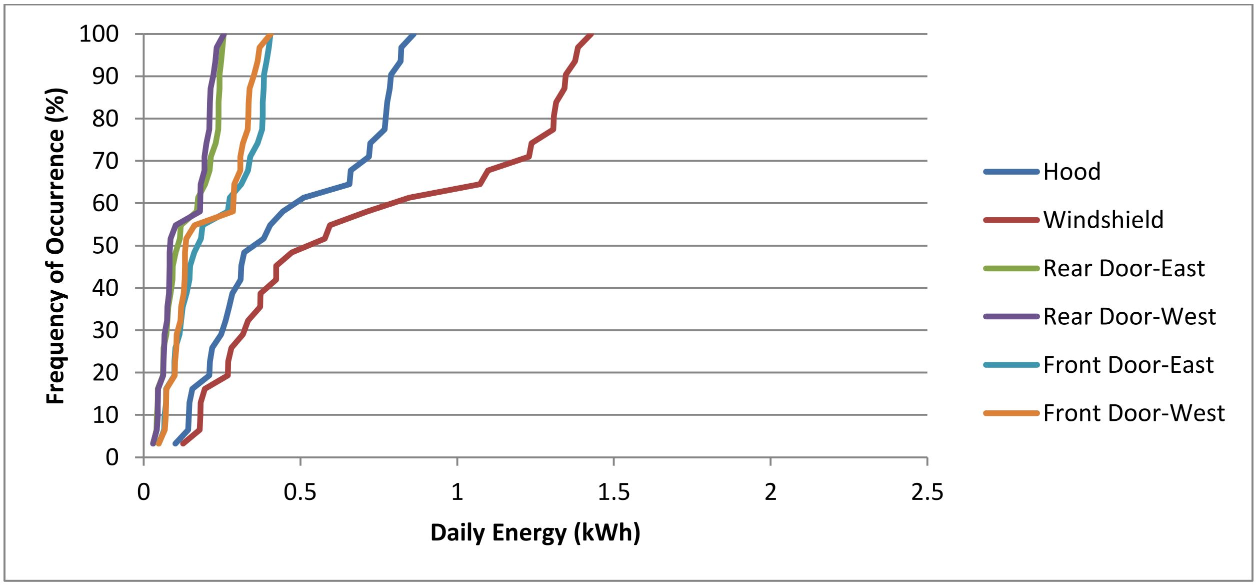

Figure 34. Daily Energy CDFs of Modeled Body Panels for January in Atlanta, GA

As shown in the figure, the daily energy generation of the hood is distributed around 0.35 kWh, with approximately 41% of the data lying above the average of 0.46 kWh. The daily energy generation of the windshield is distributed around 0.53 kWh, with approximately 42% of the data lying above the average of 0.73 kWh. The daily energy generation of the rear eastwardly facing door is distributed around 0.11 kWh, with approximately 44% of the data lying above the average of 0.14 kWh. The daily energy generation of the rear westward facing door is distributed around 0.08 kWh, with approximately 44% of the data lying above the average of 0.13 kWh. The daily energy generation of the front eastwardly facing door is distributed around 0.17 kWh, with approximately 44% of the data lying above the average of 0.22 kWh. The daily energy generation of the front westward facing door is distributed around 0.13 kWh, with approximately 44% of the data lying above the average of 0.21 kWh. Finally, the daily energy generation of the roof is distributed around 0.42 kWh, with approximately 41% of the data lying above the average of 0.52 kWh.

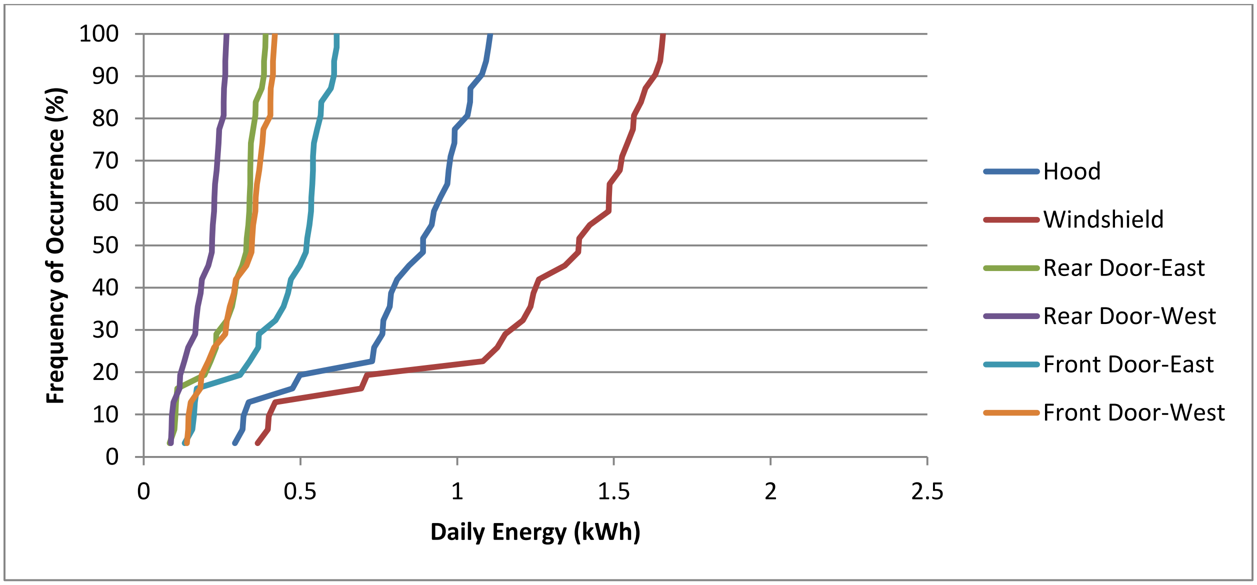

Figure 35. Daily Energy CDFs of Modeled Body Panels for October in Atlanta, GA

As shown in Figure 35, the daily energy generation of the hood in October is distributed around 0.89 kWh, with approximately 57% of the data lying above the average of 0.82 kWh. The daily energy generation of the windshield is distributed around 1.39 kWh, with approximately 60% of the data lying above the average of 1.25 kWh. The daily energy generation of the rear eastwardly facing door is distributed around 0.33 kWh, with approximately 63% of the data lying above the average of 0.28 kWh. The daily energy generation of the rear westward facing door is distributed around 0.22 kWh, with approximately 57% of the data lying above the average of 0.19 kWh. The daily energy generation of the front eastwardly facing door is distributed around 0.52 kWh, with approximately 63% of the data lying above the average of 0.45 kWh. The daily energy generation of the front westward facing door is distributed around 0.35 kWh, with approximately 57% of the data lying above the average of 0.31 kWh. Finally, the daily energy generation of the roof is distributed around 1.0 kWh, with approximately 55% of the data lying above the average of 0.94 kWh.

The results of the additional body panels covered in PV analysis for Atlanta, Georgia are summarized in Table 10. The table depicts the daily contributions for each of the body panels covered in PV with respect to the 50% frequency of occurrence from the CDF and the average. The table also includes the percent of the data above average to demonstrate the frequency of values above the average daily energy value. From the table it can be shown that the total daily energy generated by the addition of PV to the hood, windshield, roof, and front and rear doors of a C-MAX is 1.79 kWh when considering the 50% frequency of occurrence and 2.41 kWh when considering the average in the month of January. For the month of July, the total daily energy generated by the addition of PV to the hood, windshield, roof, and front and rear doors of a C-MAX is 5.84 kWh when considering the 50% frequency of occurrence and 5.48 kWh when considering the average. For the month of October, the total daily energy generated by the addition of PV to the hood, windshield, roof, and front and rear doors of a C-MAX is 5.70 kWh when considering the 50% frequency of occurrence and 5.18 kWh when considering the average.

Table 10. Summary of the Additional Body Panels Covered in PV Analysis for Atlanta, GA

City	Month	Body Panel	Daily Energy 50% Frequency of Occurrence (kWh)	Average Daily Energy (kWh)	% of Data Above Average
Atlanta, GA	January	Hood	0.35	0.46	41
		Windshield	0.53	0.73	42
		Rear Door-East	0.11	0.14	44
		Rear Door-West	0.08	0.13	44
		Front Door-East	0.17	0.22	44
		Front Door-West	0.13	0.21	44
		Roof	0.42	0.52	41
		Total	1.79	2.41	N/A
	July	Hood	1.15	1.1	64
		Windshield	1.42	1.35	65
		Rear Door-East	0.34	0.32	53
		Rear Door-West	0.35	0.3	65
		Front Door-East	0.53	0.51	53
		Front Door-West	0.55	0.48	65
		Roof	1.49	1.42	63
		Total	5.84	5.48	N/A
	October	Hood	0.89	0.82	57
		Windshield	1.39	1.25	60
		Rear Door-East	0.33	0.28	63
		Rear Door-West	0.22	0.19	57
		Front Door-East	0.52	0.45	63
		Front Door-West	0.35	0.31	57
		Roof	1.0	0.94	55
		Total	5.70	5.18	N/A

5.10.2 Determining the Effect of Daily Insolation Level

To better understand how the energy generation resulting from the addition of PV to the hood, windshield, roof, and front and rear doors of a C-MAX is effected by the level of daily insolation, the model was also run for Phoenix, Arizona and Seattle, Washington. Phoenix, Arizona is a location that experiences consistently high levels of daily insolation and Seattle, Washington, is a location that consistently experiences low levels of insolation due to cloud cover. To determine the range of daily energy values, each city was run for the months of January and July. For Phoenix, Arizona, the daily energy generation CDF's of each of the body panels in the months of July and January are shown in Figure 36 and Figure 37, respectively. For Seattle, Washington, the daily energy generation CDF's of each of the body panels in the months of July and January are shown in Figure 38 and Figure 39, respectively.

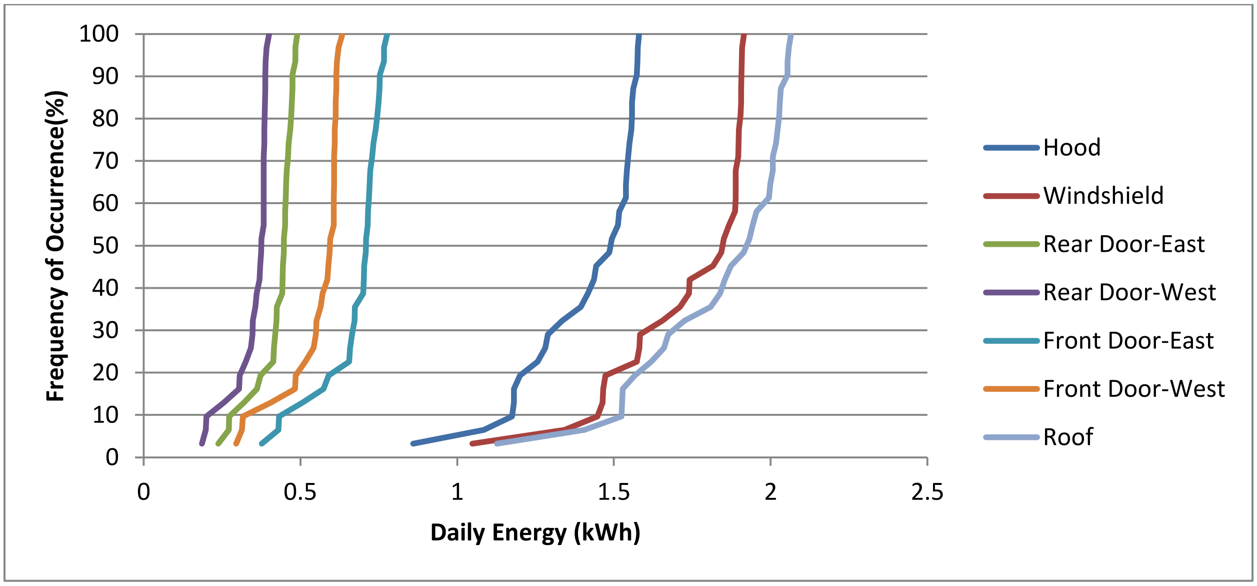

Figure 36. Daily Energy CDFs of Modeled Body Panels for July in Phoenix, AZ

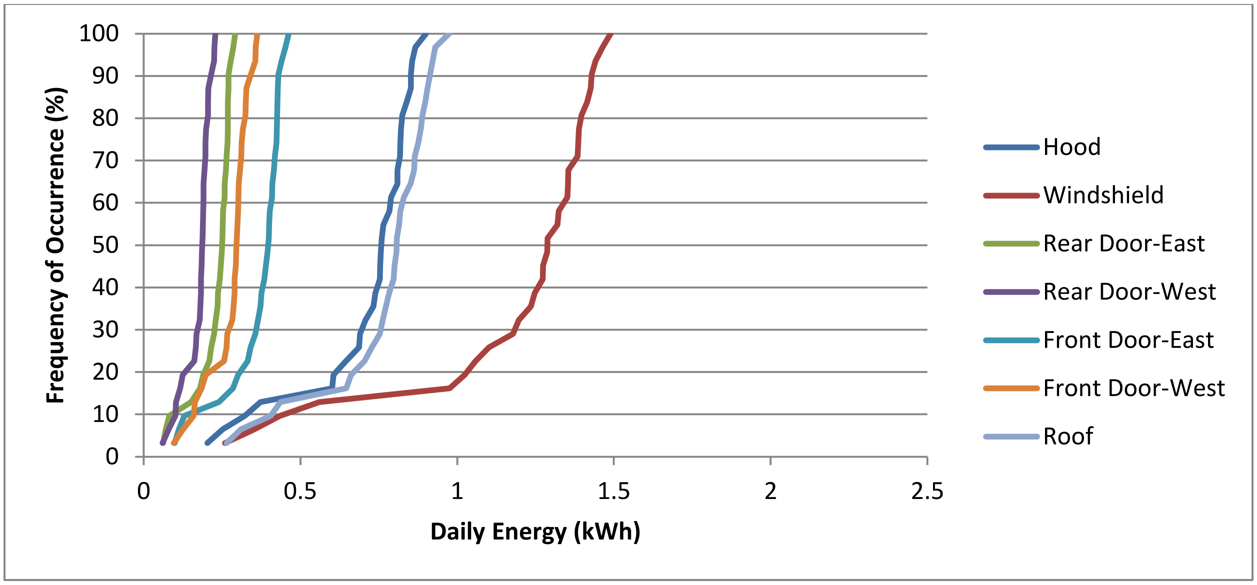

Figure 37. Daily Energy CDFs of Modeled Body Panels for January in Phoenix, AZ

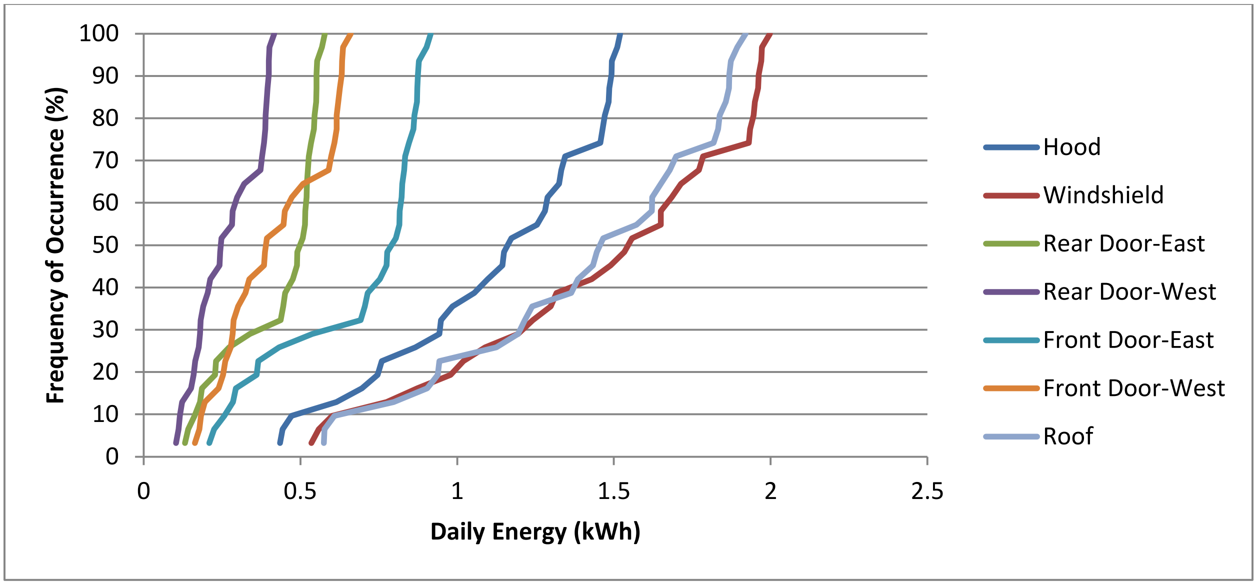

Figure 38. Daily Energy CDFs of Modeled Body Panels for July in Seattle, WA

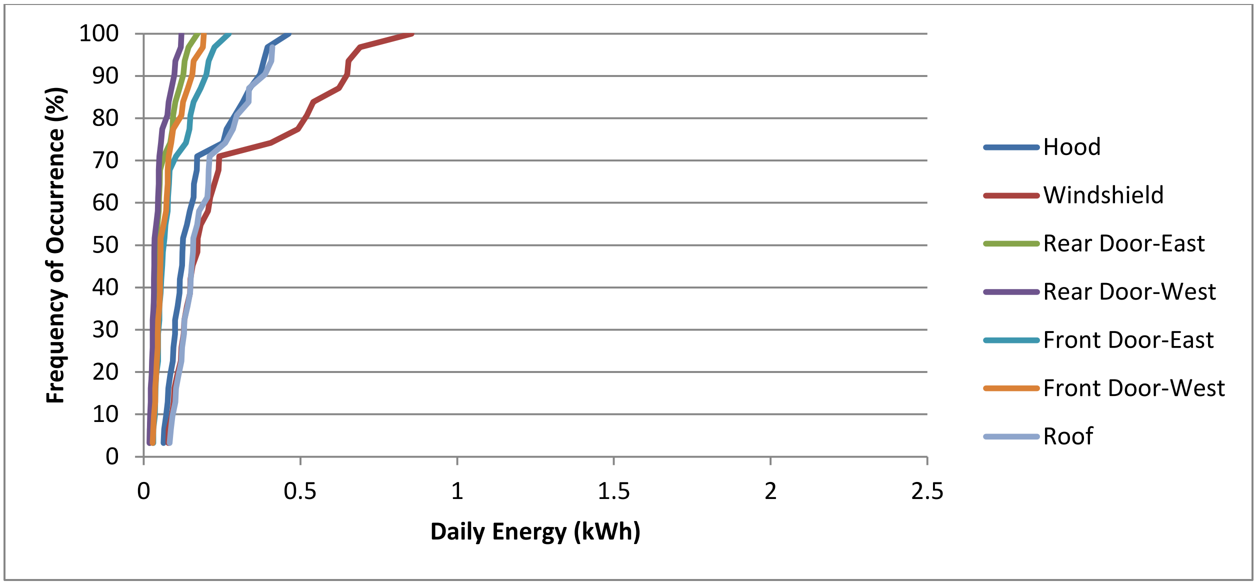

Figure 39. Daily Energy CDFs of Modeled Body Panels for January in Seattle, WA

The results of the additional body panels covered in PV analysis for Phoenix and Seattle are summarized in Table 11. The table depicts the daily contributions for each of the body panels covered in PV with respect to the 50% frequency of occurrence from the CDF and the average. The table also includes the percent of the data above average to demonstrate the frequency of values above the average daily energy value. From the table it can be shown that the total daily energy generated in Phoenix, Arizona by the addition of PV to the hood, windshield, roof, and front and rear doors of a C-MAX is 7.38 kWh when considering the 50% frequency of occurrence and 6.97 kWh when considering the average in the month of July, and 4.0 kWh when considering the 50% frequency of occurrence and 3.7 kWh when considering the average in the month of January. For Seattle, Washington, the total daily energy generated by the addition of PV to the hood, windshield, roof, and front and rear doors of a C-MAX is 6.13 kWh when considering the 50% frequency of occurrence and 5.79 kWh when considering the average in the month of July, and 0.63 kWh when considering the 50% frequency of occurrence and 0.94 kWh when considering the average in the month of January.

Table 11. Summary of the Additional Body Panels Covered in PV Analysis for Phoenix, AZ and Seattle, WA

City	Month	Body Panel	Daily Energy 50% Frequency of Occurrence (kWh)	Average Daily Energy (kWh)	% of Data Above Average
Phoenix, AZ	January	Hood	0.76	0.71	68
		Windshield	1.29	1.18	70
		Rear Door-East	0.25	0.23	68
		Rear Door-West	0.19	0.18	69
		Front Door-East	0.4	0.36	68
		Front Door-West	0.3	0.28	69
		Roof	0.81	0.76	67
		Total	4.0	3.7	N/A
	July	Hood	1.49	1.41	62
		Windshield	1.85	1.74	62
		Rear Door-East	0.45	0.42	66
		Rear Door-West	0.37	0.35	67
		Front Door-East	0.71	0.67	66
		Front Door-West	0.59	0.55	67
		Roof	1.92	1.83	62
		Total	7.38	6.97	N/A
Seattle, WA	January	Hood	0.12	0.18	29
		Windshield	0.17	0.28	28
		Rear Door-East	0.04	0.06	30
		Rear Door-West	0.03	0.05	32
		Front Door-East	0.06	0.09	30
		Front Door-West	0.05	0.08	32
		Roof	0.16	0.2	37
		Total	0.63	0.94	N/A
	July	Hood	1.16	1.12	56
		Windshield	1.55	1.46	56
		Rear Door-East	0.5	0.43	68
		Rear Door-West	0.25	0.27	46
		Front Door-East	0.79	0.68	68
		Front Door-West	0.39	0.42	46
		Roof	1.46	1.41	56
		Total	6.13	5.79	N/A

Covering the body panels of the vehicle with PV was shown to have the potential of achieving a daily energy generation near that of the daily energy generation goal for locations and times of year with high levels of daily solar insolation. However, during times of the year with low levels of daily solar insolation covering the body panels of the vehicle with PV does not demonstrate the ability to generate enough energy in a day to come near the daily energy goal. That said, as shown in Table 10 and Table 11, the daily energy contribution of the body panels covered in PV in the month of January, a low solar insolation month, is on the order of 1 kWh. While this is not sufficient to reach the daily energy goal, it may well suited for consideration as a supplement to the other more promising technologies.

CHAPTER 6: CONCENTRATED PHOTOVOLTAICS

Concentrated PV (CPV) systems utilize either reflective or refractive optics to focus the area of the concentrating optic down to a smaller area of PV material. In doing so, the system acts effectively as a PV cell of the same area as the concentrating optic. Since concentrating optics can generally be produced at a lower cost than PV material of the same area, it becomes cost-effective to use more expensive high efficiency PV cells; especially at high levels of concentration. Additional costs and complexity are however associated with CPV systems. Many CPV systems necessitate the use of a tracking mechanism to follow the sun and ensure that the concentrated sunlight lands on PV cell. Higher levels of concentration necessitate higher accuracy tracking mechanisms. The benefit to using a tracking mechanism over a standard fixed panel is that there is an increase in useable daylight hours, as the tracking allows the PV cells to make use of more sunlight in the morning and evening hours.

Additional benefits to solar concentrators include the increased PV efficiency experienced with higher radiation flux (Kalogirou 2014). Higher radiation flux also implies increased heating of the PV cell, and as a result some form of passive, and in some cases active, cooling is generally required to maintain cell temperature; particularly at high levels of concentration. A disadvantage to CPV systems is that current systems are only capable of concentrating direct beam radiation. This not only reduces the total amount of sunlight available to the PV cell by not making use of diffuse radiation, but also can drastically reduce the power output during periods of cloud cover.

6.1 Fresnel Lens Concentrator

A Fresnel lens was selected as a means of concentration for the concentrated PV concepts in order to cut the size, weight, and cost associated with traditional continuous surface lenses. For an extended review of Fresnel lenses as a means of concentrating solar energy, see reference (Xie, Dai et al. 2011). As shown in Figure 40, a Fresnel lens discretizes the continuous surface of a traditional lens into a finite number of concentric surfaces with the same curvature as the respective location in the traditional lens. The premise behind this discretization is that refraction occurs only at the optical interfaces of the lens. By discretizing the lens into prisms with the same optical interfaces, the amount of material used to achieve the same refractive properties can be considerably reduced. The weight and cost of the lens can further be reduced by appropriate material selection.

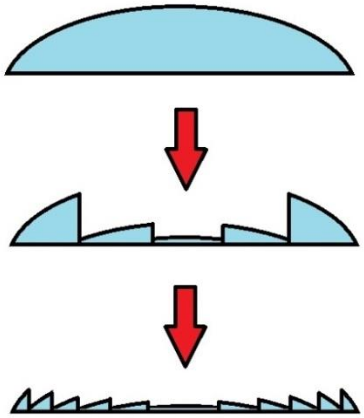

Figure 40.Illustration of Collapsing a Continuous Surface Lens into an Equivalent Fresnel Lens: Adapted from (Davis and Kühnlenz 2007)

Polymethyl methacrylate (PMMA) is commonly used as a lens material in Fresnel concentrating systems for its favorable optical properties. As shown in Figure 41, when compared to the AM 1.5 direct spectrum, the optical transmittance of PMMA is good over the wavelength range of interest for PV applications; namely, 400-1200 nm. From the figure it is also clear that the ultraviolet (100-400 nm) and infrared (700 nm-1 mm) transmittance for PMMA is considerably lower than that of glass. This property of PMMA has both positive and negative implications to the CPV application. Since these wavelengths cannot be used by the PV cells the optical flux absorbed by the lens material will not contribute to the heating of the PV cell. This effect may result in the increased operating efficiency of the PV cell, and also a reduced exposure to damaging UV radiation. At the same time the increase in temperature of the PMMA due to UV and IR absorbtance may accelerate the UV degradation of the lens.

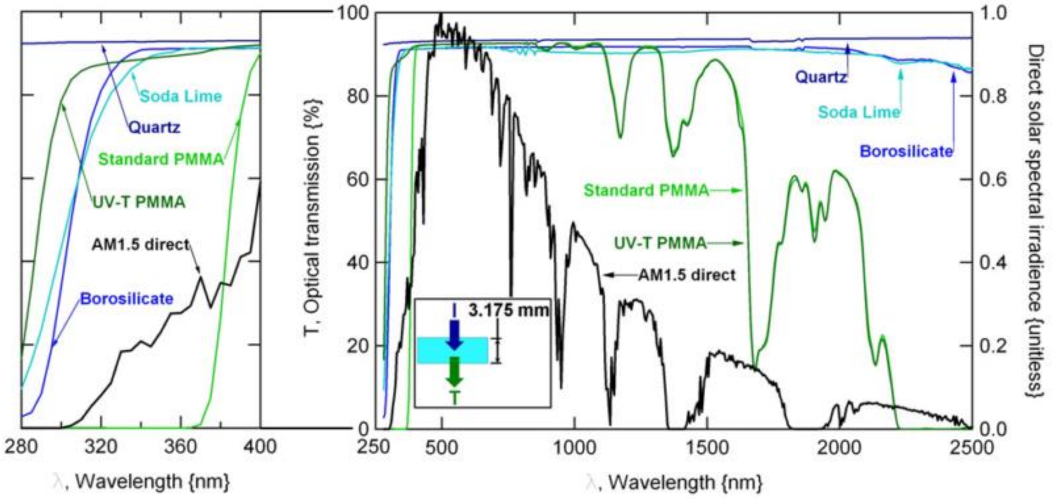

Figure 41.Measured Optical Transmittance for candidate CPV Optical Component Materials (Miller 2009)

The longevity of materials used in CPV systems has not been well researched; however, the degradation in the optical transmittance of PMMA resulting from outdoor exposure has been demonstrated to be less than 7%, for wavelengths pertinent to photovoltaics, over test periods up to 22 years at multiple test sites (Miller and Kurtz 2011). Other studies have concluded that the weathering properties of PMMA glazing in thermal collector applications were in the range of glass or even slightly better (Florian Ruesch 2008), and that the PMMA will endure 20 years exposure in the southwestern United states (Rainhart and Schimmel Jr 1975)

In designing a concentrating Fresnel lens, considerable design work will be necessary in order to maximize the optical efficiency, flux uniformity, and tracking error tolerance of the lens, while at the same time minimizing the effects chromatic aberration. This may be accomplished using non-imaging lens design, which must be analyzed using ray-tracing software (Miller and Kurtz 2011). Additional secondary optics, such as kaleidoscope homogenizers, may be used in conjunction with Fresnel lenses to improve flux uniformity, compensate misalignment, reduce chromatic aberration, and compensate focusing errors (Miller 2009). The mechanical properties of the lens should also be considered in the lens design. Rainhart and Schimmel Jr (1975) have shown that the flexural strength of PMMA to be reduced by 51% after 17 years of outdoor exposure. Physical aging or densification of the polymers may affect many mechanical characteristics, including: dimensions, Poisson’s ratio, yield stress, mechanical modulus, and mechanical dissipation. Changes in these mechanical characteristics may in turn affect optical characteristics such as optical alignment. To date, such design work has yet to be completed.

6.2 Off-Vehicle Concentrator

Various design alternatives for a concentrated photovoltaic system capable of reaching the daily energy goal of 7.6 kWh have been developed and modeled. In the initial design ideation, deployable on vehicle concentrating systems were considered. Systems such as the stretched lens array concentrating system used in space applications (Xie, Dai et al. 2011), and the concentrating system devised by the Nuon Solar Race team for the World Solar Challenge have been previously developed (NuonSolarTeam 2014); however, due to the added complexity and on vehicle mass, such concepts were quickly eliminated. The remaining designs involve off-vehicle concentrators, and a C-MAX with the roof covered in PV. All of the design alternatives utilize Fresnel lenses as a means of concentration, and employ some form of tracking mechanism in order to increase the overall efficacy of the system. The tracking mechanism is the primary distinction between the design alternatives, and they are named accordingly:

- Tracking Vehicle – Static Lens
- Static Vehicle – Tracking Lens
- Fiber Optic System

The Tracking Vehicle – Static lens concept involves a statically mounted overhead Fresnel lens to concentrate the incident direct beam solar radiation and a C-MAX equipped with the hardware and software necessary to autonomously track the projected path of the Sun throughout the course of the day. The Static Vehicle – Tracking Lens concept involves a Fresnel lens capable of tracking the Sun’s altitude and azimuth, and a C-MAX, which remains stationary at a fixed distance from the lens. Finally, the fiber optic system uses an array of small Fresnel lenses to concentrate light into optical fibers. The Fresnel lens array and the inputs of the optical fibers are attached to a two-axis tracking mechanism, and the outputs of the optical fibers emit the concentrated light onto the roof of the vehicle. The modeling of the designs is explained in detail in the following sections.

6.3 Tracking Vehicle – Static Lens Concept

As previously mentioned, the Tracking Vehicle – Static Lens concept involves a statically mounted overhead Fresnel lens to concentrate the incident direct beam solar radiation. To maximize the use of on-vehicle technology, the vehicle will perform the necessary tracking.

The size of the Fresnel lens necessary to reach the 7.6 kWh daily energy goal is location specific. Locations with very high levels of direct insolation will require smaller lens areas, and locations at higher latitudes and locations with lower levels of daily direct insolation will require larger lenses. To manufacture the large Fresnel lenses necessary for such a concept, it will be necessary to discretize the Fresnel lens into smaller, more easily-manufacturable sections. After speaking with several lens manufacturers, the largest discretized point focus Fresnel lens that any of them have manufactured is 9 square meters. The effect of discretizing the Fresnel lens on the lens's efficiency is yet to be determined.

The premise behind the Tracking Vehicle – Static Lens concept is illustrated in Figure 42. The discretized Fresnel lens is supported by a structure at a fixed distance from the roof of the C-MAX. This distance is based upon the f-number of the Fresnel lens, and is such that the focal area is equal to the area of the C-MAX roof at the Sun's highest point. The f-number of a lens is the ratio of the focal length to the maximum diameter of the lens. Figure 43 illustrates the relationship between the transmission efficiency of an acrylic lens and the f-number of the lens. To prevent dust and debris from collecting in the grooves of the lens, the grooves of the lens should be downward facing. It is clear from Figure 43 that there is a considerable decrease in transmission efficiency for a "grooves in" concentrating lens for f-numbers less than 1. Higher f-numbers will result in improved transmission efficiency, but will also require a taller concentrating structure, for a given lens size. For all modeled concepts utilizing concentrating Fresnel lens, the Fresnel lens transmission efficiency, or optical efficiency, is assumed to be 85%.

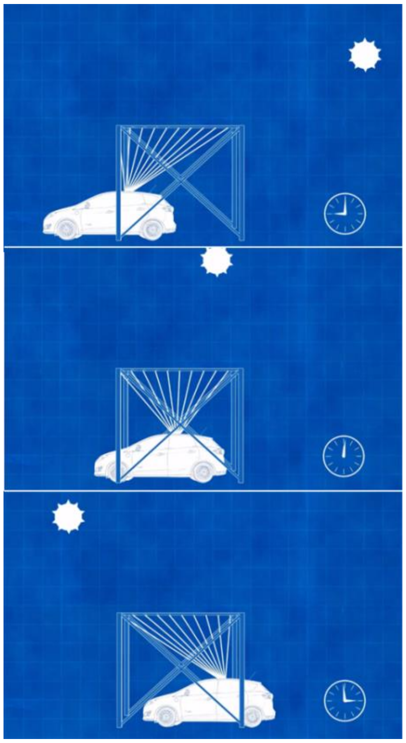

Figure 42. Illustration of Tracking Vehicle – Static Lens Concept

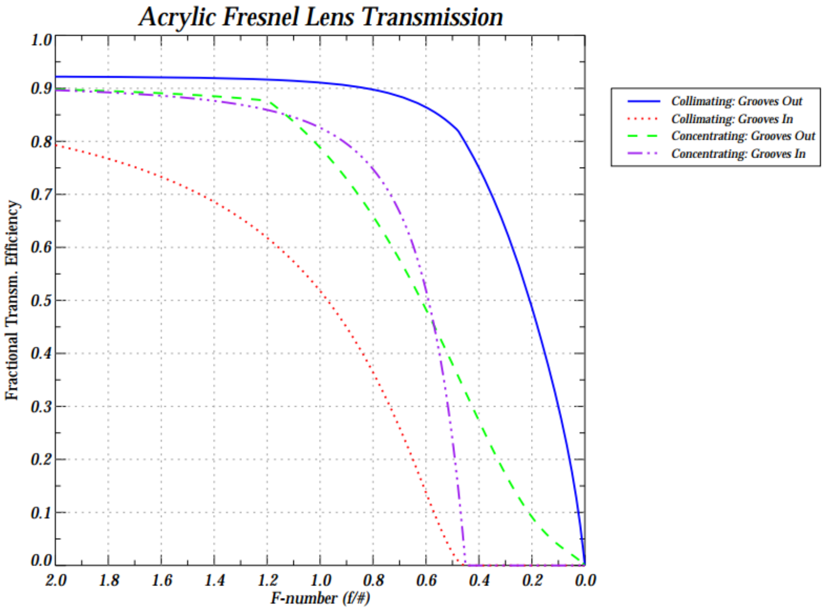

Figure 43. Fresnel Lens Transmissibility as a Function of Lens F-number (Davis and Kühnlenz 2007)

The motion of the Sun is in two planes, and as a result the path that the C-MAX must traverse is non-linear. As shown in the Figure 44, as the Sun traverses from east to west, the vehicle must move counter the motion of the sun in order to keep the focal area atop the C-MAX. As the Sun's elevation, or height from the horizon, increases, the C-MAX must also traverse south to north. As shown in Figure 44, during the summer months, the Sun rises higher in the sky, and for the vehicle to track this second plane of motion of the Sun the driving path becomes much more of an arc.

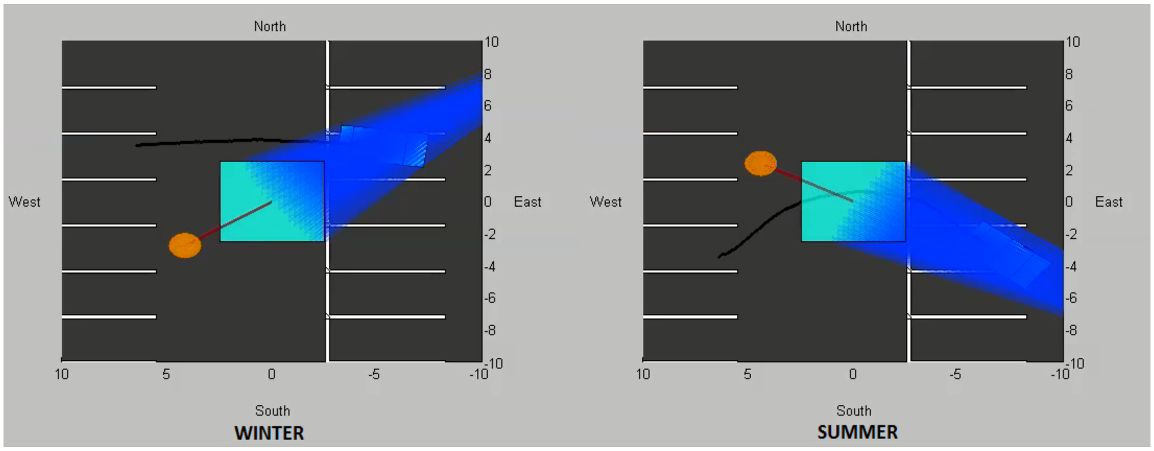

Figure 44. Driving paths for winter and summer months, respectively, in Columbia, SC

Since a driver will not be present at all times while the vehicle is situated under the concentrator, it is necessary that the C-MAX be equipped with the hardware and software necessary to autonomously track the path of the Sun over the course of the day. As previously mentioned, the path of the Sun varies with geographic location and with time of year. As a result, the hardware and software must have sufficient temporal and spatial resolution to accurately locate and track the focal area on any given day, at any time of day, at any location. Additionally, it should be able to do so in the absence of concentrated radiation or direct beam radiation, in the event that there is temporary heavy cloud cover.

6.3.1 Modeling

A 3D ray tracing simulation was developed to accurately trace rays from the Sun, through the Fresnel lens, and onto the roof of the vehicle. For the purposes of modeling the direct beam radiation from the Sun is approximated as collimated and discretized into rays. If more accurate models are to be developed, the 0.5° solid angle subtended by the solar disk at the Earth's surface should be taken into consideration (Badescu 2008). Circumsolar radiation is neglected in this model. If more accurate models are to be developed, the effect of circumsolar radiation should be taken into consideration (Buie and Monger 2004). The model can be run for any city in the TMY3 data set, and for any month, day, and time. The GPS coordinates of the selected city are used in conjunction with the month, day, and time to determine the Sun's position in terms of altitude and azimuth angles of the sun; shown in Figure 45. The Sun's position is calculated using the day number N, as a time variable. This convention has been adopted by other researchers including (Braun and Mitchell 1983),(Gunerhan and Hepbasli 2007),(Huang and Sun 2007),(Morcos 1994),(Tang and Wu 2004).

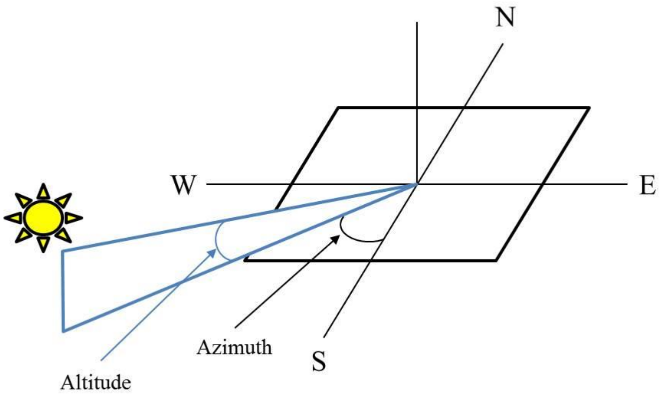

Figure 45. Illustration of Sun's Position in Terms of Solar Angles

In calculating the Sun's position, the equation of time must first be calculated. Prakash and Garg (2000) approximate the equation of time, ET in minutes by

$$ET = 9.87\sin(2D) - 7.53\cos(D) - 1.5\sin(D) \tag{10}$$

where,

$$D = 360° \frac{(N - 81)}{365} \quad (11).$$

Here, N is the day number of the year, with January 1 being equal to 1. This value can then be used in calculating the apparent solar time, AST. In the western longitudes AST is calculated as follows

$$AST = LST + \left(\frac{4\text{min}}{\text{deg}}\right)(LSTM - Long) + ET \quad (12).$$

Here, LST is the local standard time or clock time for that zone (adjusted for daylight savings time, DST, by $LST = DST - 1$ hr), $Long$ is the local longitude at the position of interest, and $LSTM$ is the local longitude of standard time meridian. $LSTM$ is given by

$$LSTM = 15° * \left(\frac{Long}{15}°\right)_{\text{round to integer}} \tag{13}$$

The solar angles of interest can now be calculated using the above values. The hour angle, H, is also the azimuth angle of the Sun's rays, and is given by

$$H = \frac{(No. of\ minutes\ past\ midnight, AST) - 720\ \text{mins}}{4\ \text{min/deg}} \tag{14}$$

The solar altitude angle, γ is the angular height of the Sun from the horizon, and is calculated by

$$\sin(\gamma) = \cos(L)\cos(\delta)\cos(H) + \sin(L)\sin(\delta) \tag{15}$$

Here, L is the latitude of the location of interest, H is the hour angle, and δ is the declination angle (positive for the northern hemisphere). The declination angle is the angular distance to the Sun north of the Earth's equator, given by

$$\delta = 23.45° \sin\left[\frac{N + 284}{365} * 360°\right] \tag{16}$$

With the direct beam radiation from the Sun being treated as collimated, the altitude and azimuth angles determine the incidence angles of the Sun's rays on the lens. The refraction of these rays into and out of the lens can then be determined by the vector form of Snell's Law, as shown in Equation 17:

$$\hat{s}_2 = \frac{\eta_1}{\eta_2}\left[\hat{N}\ \text{x}\ \left(-\hat{N}\ \text{x}\ \hat{s}_1\right)\right] - \hat{N}\sqrt{1 - \left(\frac{\eta_1}{\eta_2}\right)^2 \left(\hat{N}\ \text{x}\ \hat{s}_1\right)\left(\hat{N}\ \text{x}\ \hat{s}_1\right)} \tag{17}$$

Here $\hat{s}_1$ is the incident ray, $\hat{s}_2$ is the refracted ray, $\hat{N}$ is the surface normal vector at the point of incidence, η_1 is the index of refraction of the incident ray's medium, and η_2 is the index of refraction of the refracted ray's medium.

The refractive index of a material is spectrally dependent. The refractive indices of some materials commonly used in CPV applications are plotted with respect to the range of wavelengths pertinent to PV applications in Figure 46. From the figure, it is clear that for PMMA, the material of which the Fresnel lens is to be made, the refractive index is relatively constant for wavelengths in the useable range of the PV cells – 400-1200 nm. For this broadband analysis, it is assumed that the refractive index of the PMMA used for the Fresnel lens is a constant 1.490. The refractive index of a material also has some dependence on the temperature, pressure, and composition of the medium – particularly with gases. For simplicity it is assumed that the refractive index of Air at STP is 1.000293 (de Podesta 2002). If more accurate models are to be developed, the effect of wavelength, temperature, pressure, etc. should be considered in determining the refractive index.

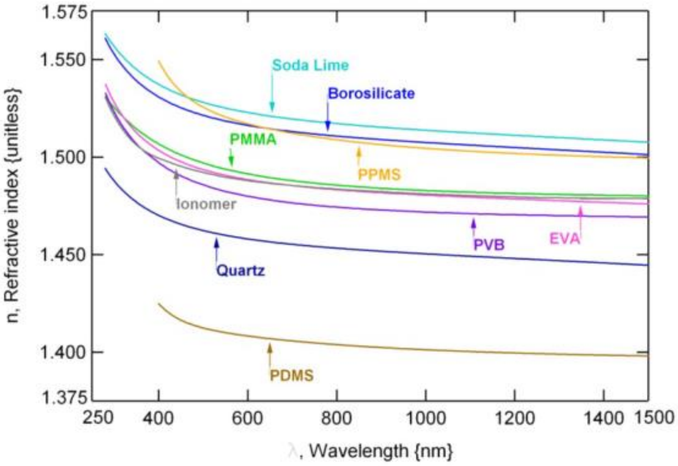

Figure 46. Refractive Indices of candidate CPV Optical Materials Over the Wavelength Range Commonly Utilized in PV Applications (Miller 2009)

The refracted rays exiting the lens are then traced to the plane of the roof of the C-MAX. The PV energy production is dictated by the percentage of rays landing on the roof of the vehicle as well as the incidence angle of these rays; amongst other factors. The percentage of rays landing on the roof of the vehicle is determined by dividing the number of rays at a particular instant in time that are within a polygon of the same area and contained in a plane the same height off of the ground as the roof of a C-MAX by the number of rays in the initial discretization of the concentrating lens. The position of the polygon representing the roof of the vehicle, and hence the path that the vehicle must traverse to track the Sun, is determined by translating the polygon representing the roof to the location with the highest density of transmitted rays at each time step. Figure 47 illustrates a single time step of the current model. As shown in the in the figure, the model illustrates the position of the sun at each time step, as well as the position that the vehicle must be oriented in, in order for the maximum number of transmitted rays to land on the roof of the C-MAX.

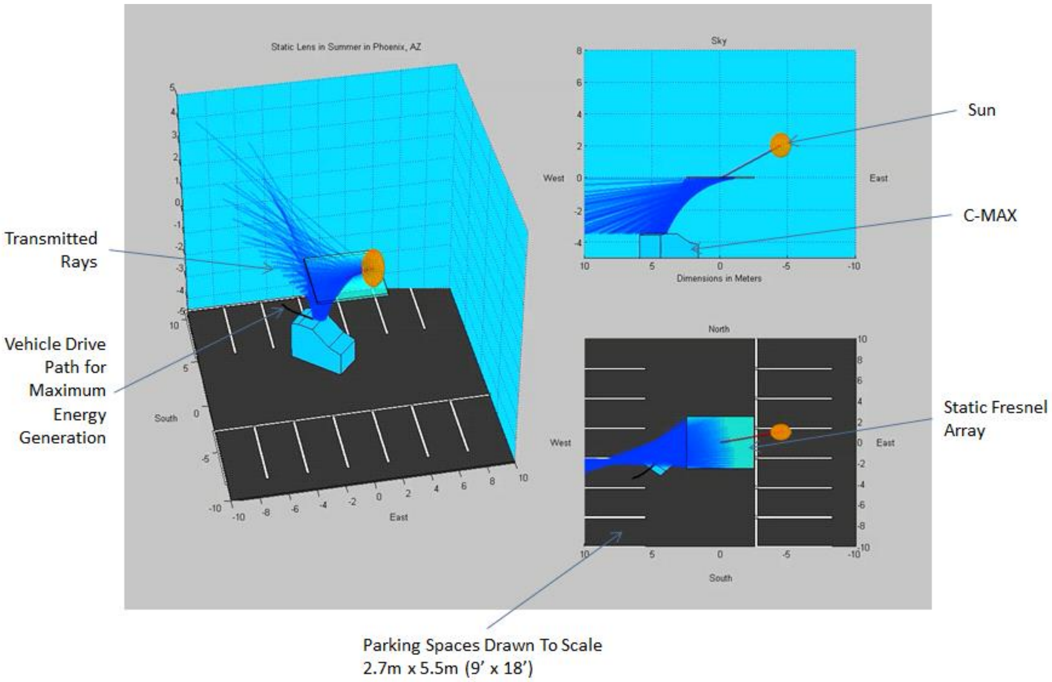

Figure 47. Tracking Vehicle - Static Lens Array Landscape

Since all of the transmitted rays do not land perpendicular to the roof and therefore PV surface, losses are incurred that are proportionate to the cosine of the incidence angle. The current model simplifies the effect of the incidence angle by considering only the cosine of the elevation angle at each time step with respect to a horizontal flat surface; however, if more accurate models are to be developed, the effect of the incidence angle of each ray on the 2-D roof curvature should be taken into consideration. As shown in Figure 48, the incidence angle, θ_i, between a single incident ray and the surface normal at the point of incidence is given as:

$$\begin{aligned}\cos(\theta_i) = {} & \sin(\delta)\sin(L)\cos(\beta) - \sin(\delta)\cos(L)\sin(\beta)\cos(\alpha) \\ & + \cos(\delta)\cos(L)\cos(\beta)\cos(H) \\ & + \cos(\delta)\sin(L)\sin(\beta)\cos(\alpha)\cos(H) \\ & + \cos(\delta)\sin(\beta)\sin(\alpha)\sin(H)\end{aligned} \tag{18}$$

Here, δ is the solar declination angle, L is the latitude of the location of interest, H is the solar azimuth angle, β is the tilt of the surface with respect to the horizontal, and α is the azimuth angle of the surface (measured clockwise from south).

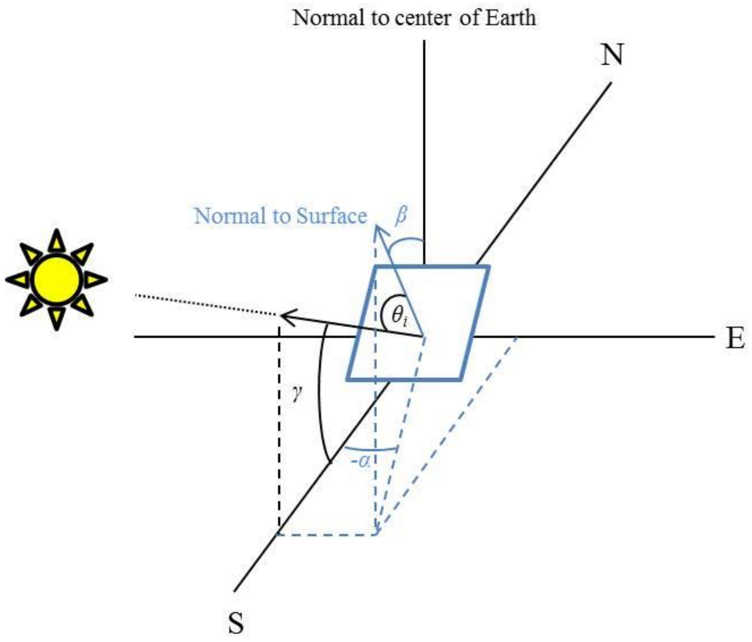

Figure 48. Solar Radiation Incident on an Inclined Surface: Adapted from (Demain, Journée et al. 2013)

It follows that the direct radiation flux onto the surface is then

$$I_D = I_{DN}\cos(\theta_i) \tag{19}$$.

This direct radiation flux, I_D, should be determined for each ray incident on the PV, and then be used to more accurately determine the PV output.

In addition to simplifying the effect of the incidence angle on the PV performance, the model does not take into account the effect of the non-uniformity of the light intensity on the performance of the PV array. The model also neglects the spectral non-uniformity due to chromatic aberration on the performance of the PV array. Finally the model does not take into account the thermal derate in PV efficiency associated with operating temperatures greater than 25˚C. A constant efficiency of 21.5%, which is lower than that of the rated efficiency of the arrays, is assumed on the premise that heat transfer mechanisms will be employed to control the PV array’s temperature. The energy output of the model will then be equal to the direct insolation incident on the static Fresnel lens, times the percentage of transmitted rays incident on the C-MAX roof, less the PV efficiency of 21.5%, less the wiring efficiency of 93%, less an assumed optical efficiency of 85%, less the efficiency loss resulting from the cosine of the incidence angle.

6.3.2 Results and Discussion

For comparison to the one sun analyses, the static lens analysis was initially run under similar input conditions; namely, a location of Atlanta, Georgia and a PV efficiency of 21.5%. As with the one sun models, a wiring efficiency of 93% was assumed, and an additional Fresnel lens efficiency of 85% was included. To gain a better understanding of the year-round energy generation, the tracking lens model was run for the months of January, July, and October, with a time step of 60 minutes. As previously mentioned, after speaking with several lens manufacturers, the largest discretized point focus Fresnel lens that any of them have manufactured is 9 square meters. For this reason, in the initial analysis the energy generation at each time step was scaled to the area of a 9 square meter collector. The concentration level of a 9 square meter collector concentrating onto a 1.2 square meter PV array is 7.5 times. The daily energy generation values for each month were then used to produce the daily energy generation CDFs depicted in Figure 49.

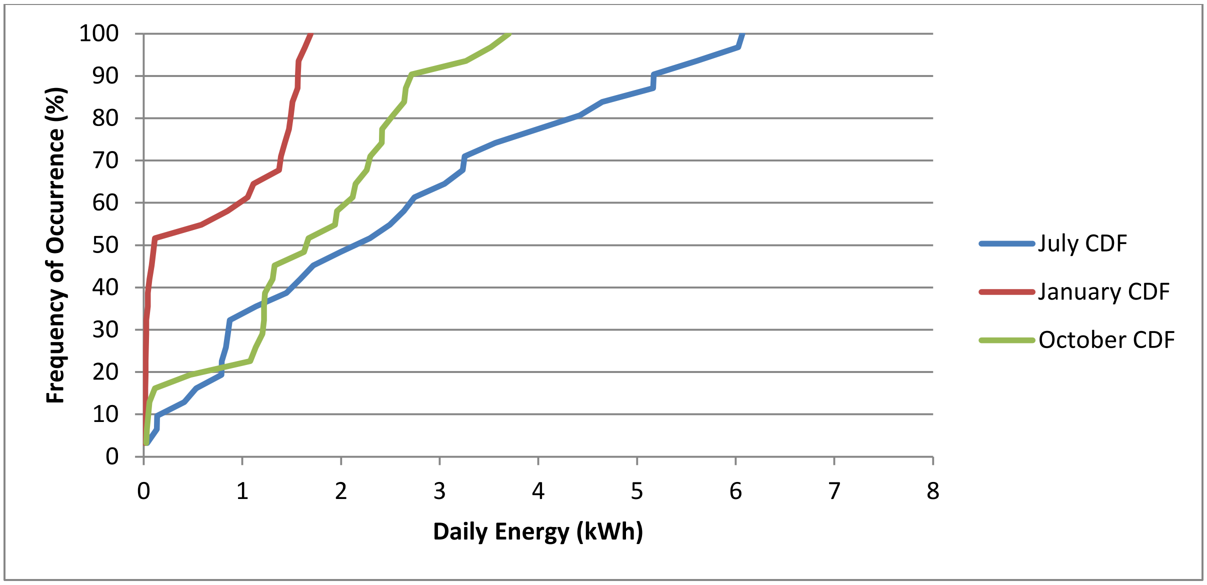

Figure 49. Daily Energy CDFs for 9m² Static Lens in Atlanta, GA

As shown in the figure, for a 9 m² static Fresnel lens in Atlanta, Georgia, the daily energy generation in the month of January is distributed around 0.11 kWh, with approximately 44% of the data lying above the average of 0.67 kWh. The daily energy generation in the month of July is distributed around 2.15 kWh, with approximately 45% of the data lying above the average of 2.5 kWh, and the daily energy generation for the month of October is distributed around 1.65 kWh, with approximately 48% of the data lying above the average of 1.69 kWh.

As with the one sun analyses, to better understand how the energy generation of a 9 m² static lens concept is effected by the level of daily insolation, the model was also run for Phoenix, Arizona and Seattle, Washington. Phoenix, Arizona is a location that experiences consistently high levels of daily insolation and Seattle, Washington, is a location that consistently experiences low levels of insolation due to cloud cover. To determine the range of daily energy values throughout the year, each city was run for the months of January, July, and

October. For Phoenix, Arizona, the daily energy generation CDF's for the months of January, July, and October are shown in Figure 50. For Seattle, Washington, the daily energy generation CDF's for the months of January, July, and October are shown in Figure 51.

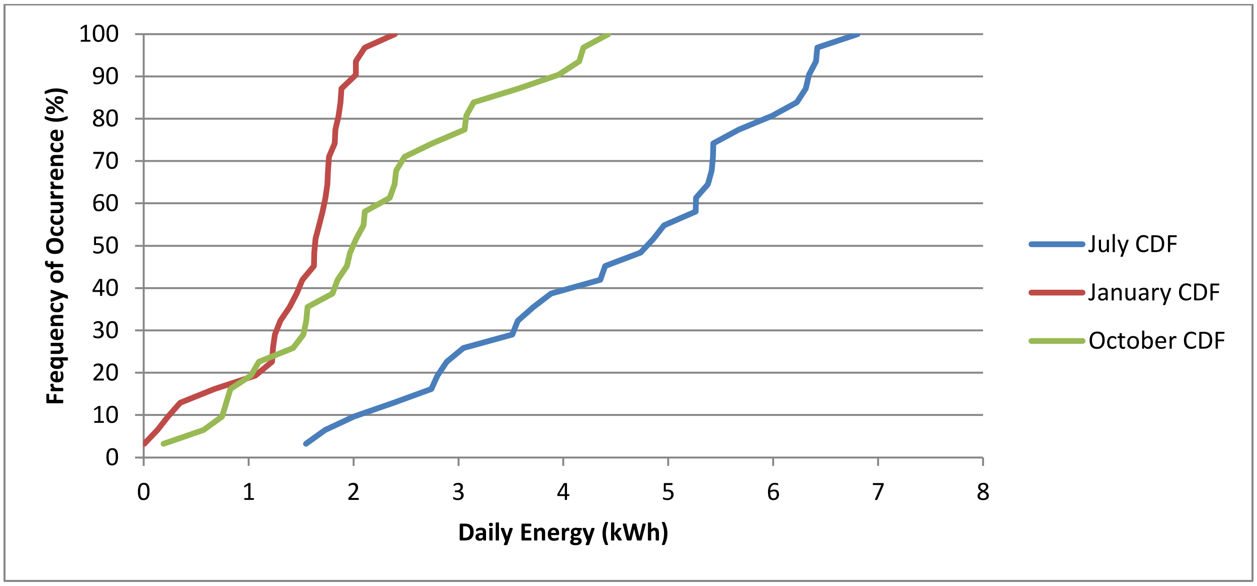

Figure 50. Daily Energy CDFs for 9m² Static Lens in Phoenix, AZ

As shown in Figure 50, for a 9 m² static Fresnel lens in Phoenix, Arizona, the daily energy generation in the month of January is distributed around 1.6 kWh, with approximately 62% of the data lying above the average of 1.4 kWh. The daily energy generation in the month of July is distributed around 4.8 kWh, with approximately 54% of the data lying above the average of 4.5 kWh, and the daily energy generation for the month of October is distributed around 2.0 kWh, with approximately 41% of the data lying above the average of 2.2 kWh.

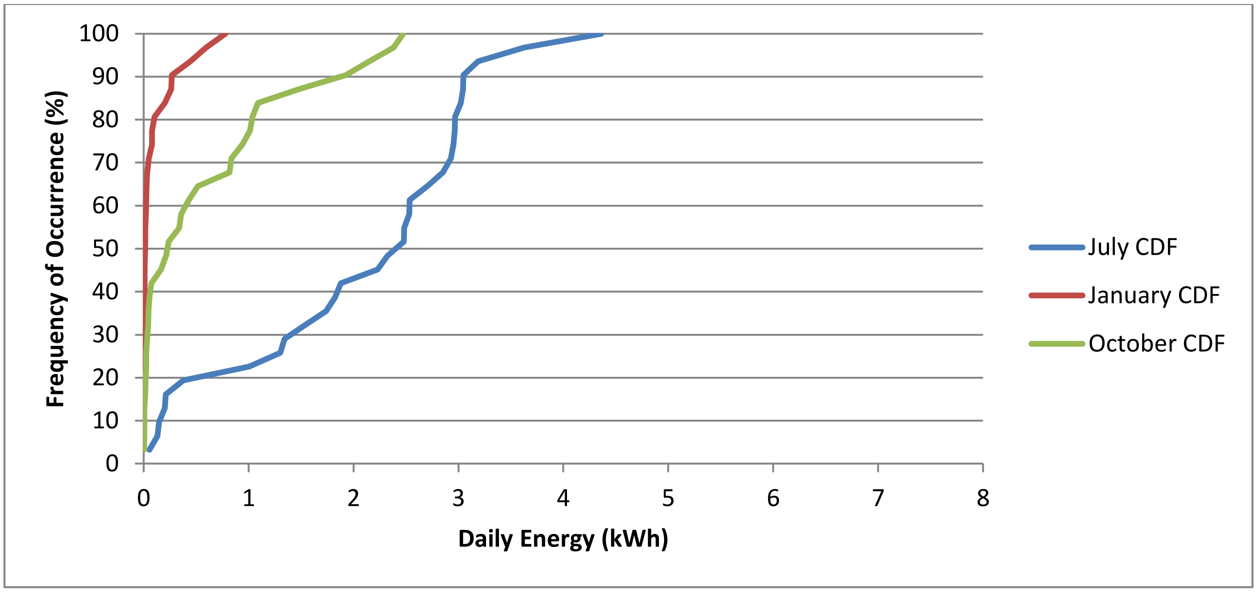

Figure 51. Daily Energy CDFs for 9m² Static Lens in Seattle, WA

As shown in Figure 51, for a 9 m² static Fresnel lens in Seattle, Washington, the daily energy generation in the month of January is distributed around 0.01 kWh, with approximately 20% of the data lying above the average of 0.14 kWh. The daily energy generation in the month of July is distributed around 2.4 kWh, with approximately 56% of the data lying above the average of 2.1 kWh, and the daily energy generation for the month of October is distributed around 0.23 kWh, with approximately 35% of the data lying above the average of 0.61 kWh. The results of this analysis for each city and month are summarized in Table 12.

.

Table 12. Summary of 9 m² Static Lens Concept

City	Month	Daily Energy 50% Frequency of Occurrence (kWh)	Average Daily Energy (kWh)	% of Data Above Average
Atlanta, GA	January	0.11	0.67	44
	July	2.15	2.5	45
	October	1.65	1.69	48
Phoenix, AZ	January	1.6	1.4	62
	July	4.8	4.5	54
	October	2.0	2.2	41
Seattle, WA	January	0.01	0.14	20
	July	2.4	2.1	56
	October	0.23	0.61	35

A similar analysis was conducted to determine the minimum static Fresnel lens area that would be necessary to reach the daily energy generation goal of 7.6 kWh. For the analysis it was assumed that the highest levels of daily direct beam insolation occur in the month of July. As such, the minimum static Fresnel lens area that would be necessary to reach the daily energy generation goal of 7.6 kWh would be the minimum static Fresnel lens area necessary to reach the daily energy generation goal in the month of July. From the analysis, it was determined that a 72 m² static Fresnel lens would be necessary in Seattle, Washington to reach a daily average of 7.9 kWh in July, with the CDF of daily energy values centered around 7.11 kWh and with 43% of the values above average. In Atlanta, Georgia, a 49 m² static Fresnel lens would necessary to reach a daily average of 7.5 kWh in July, with the CDF of daily energy values centered around 6.2 kWh and with 46% of the values above average. Likewise, in Phoenix, Arizona, a 18 m² static Fresnel lens would be necessary to reach a daily average of 7.6 kWh in July, with the CDF of daily energy centered around 9.0 kWh and with 51% of the values above average.

The tracking vehicle - static lens concept addresses the desire to use the on-board vehicle technology as much as possible; however, this comes at considerable cost. The primary concern with such a system is safety. Exposure to concentrated solar radiation can pose serious and potentially fatal hazards to users and any other people or animals that may come into contact with the system. In addition, concentrated solar radiation presents the risk of destroying any material not suited to handle such high levels of radiative flux. Additional safety concerns arise with the autonomously tracking vehicle. The vehicle will necessarily be able to detect and respond to any persons, animals, or objects that may come into its path. In addition, in avoiding these persons, animals, or objects, the vehicle should also be capable of having the concentrated radiation incident on any part of the vehicle not capable of withstanding such high levels of radiative flux.

As previously mentioned, having the vehicle track the sun poses certain design challenges. Since a driver will not be present at all times while the vehicle is situated under the concentrator, it is necessary that the vehicle be equipped with the hardware and software necessary to autonomously track the path of the Sun over the course of the day. The hardware and software implemented to track the sun must have sufficient temporal and spatial resolution to accurately locate and track the focal area on any given day, at any time of day, at any location. Additionally, it should be able to do so in the absence of concentrated radiation or direct beam radiation, in the event that there is temporary heavy cloud cover.

Although the vehicle tracks the sun in this concept, there are considerable efficiency losses associated with the static lens. As shown Table 12, a 9 m^2 static lens is capable of generating 2.5 kWh on average for the month of July in Atlanta, Georgia; however, as previously discussed, to reach the daily energy generation goal of 7.6 kWh, the necessary static lens area jumps to 49 m^2. This is a result of considerable losses due to internal refraction in the lens and the effect of the incidence angle on the PV at low solar elevation angles. To compensate for these losses, the size of the lens increases drastically to allow for greater energy generation at greater solar elevation angles. Aside from the considerable inefficiencies, the Fresnel lens area necessary for a single vehicle is simply impractical.

Issues that are common to all CPV systems; namely, the ‘off-season’ and geographic utilities of such systems are only exaggerated by the fact the lens does not track the sun. As previously stated, current concentrating optics are only capable of concentrating direct beam radiation. During periods of heavy cloud cover the direct beam irradiance can drop considerably, thereby drastically reducing the electricity generating capabilities of CPV systems. As a result, locations, like Seattle, Washington, which experience whole seasons of heavy cloud cover, are not particularly suitable for CPV systems. To make matters worse, these cloudy seasons often correspond to the time of year when the sun is at its lowest elevation throughout the day. Locations at higher latitudes experience lower solar elevation angles than locations at lower latitude, and as a result, for cities like Seattle, the issue of cloud cover is compounded by the aforementioned losses resulting from low solar elevation.

6.4 Static Vehicle - Tracking Lens

As previously mentioned, the Static Vehicle – Tracking Lens concept involves a tracking Fresnel lens capable of concentrating the incident direct beam solar radiation onto the roof of a static vehicle over the course of the day. The benefit to this design is that the vehicle does not require autonomous driving capabilities. Again, the size of the Fresnel lens necessary to reach the 7.6 kWh daily energy goal is location specific. Locations with very high levels of direct insolation will require smaller lens areas, and locations at higher latitudes and locations with lower levels of daily direct insolation will require larger lenses. As with the Static Lens – Tracking Vehicle concept, it will be necessary to discretize the Fresnel lens into smaller, more easily-manufacturable sections. After speaking with several lens manufacturers, the largest discretized point focus Fresnel lens that any of them have manufactured is 9 square meters. The effect of discretizing the Fresnel lens on the lens's efficiency is yet to be determined.

The premise behind the Static Vehicle – Tracking Lens concept is illustrated in Figure 52. The discretized Fresnel lens is articulated by a mechanism, which tracks the sun, while keeping the lens at a fixed distance from the roof of the C-MAX. This distance is based upon the f-number of the Fresnel lens, and is such that the focal area is equal to the area of the C-MAX roof at the Sun's highest point. As previously discussed, the motion of the Sun is in two planes, and as a result the lens must track about at least two-axes. In addition, the lens must be articulated in such a way that the distance from the roof of the C-MAX to the center of the lens remains constant, as changing this distance will affect the concentration level. As the driving path for the Tracking Vehicle – Static Lens concept varied throughout the year, so will the path that the lens must traverse in order to track the sun. To further complicate matters, the path that the lens must traverse will be location dependent.

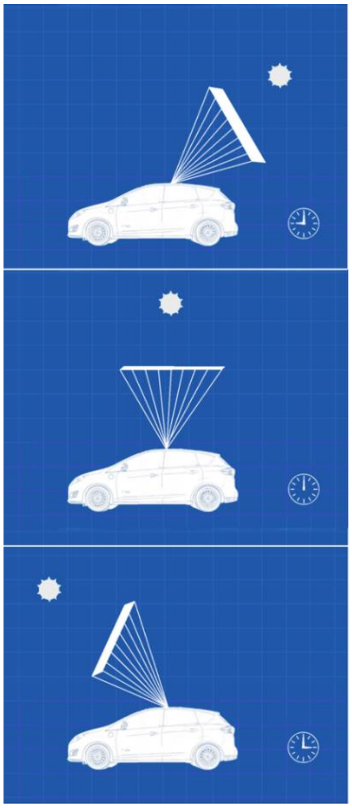

Figure 52. Illustration of Static Vehicle - Tracking Lens Concept

A mechanism to perform the task of articulating the lens has yet to be devised. It will be necessary that the mechanism be equipped with the hardware and software necessary to autonomously track the path of the Sun over the course of the day. As previously mentioned, the path of the Sun varies with geographic location and with time of year. As a result, the hardware and software must have sufficient temporal and spatial resolution to accurately locate and track the Sun on any given day, at any time of day, at any location, while maintaining a fixed distance between the roof of the C-MAX and the center of the lens. Additionally, it should be able to do so in the absence of concentrated radiation or direct beam radiation, in the event that there is temporary heavy cloud cover.

6.4.1 Modeling

A 3D ray-tracing simulation, similar to that developed for the Tracking Vehicle – Static Lens concept, was also developed for the Static Vehicle – Tracking Lens concept. This 3D simulation however, was not developed to calculate the energy produced by the concept, but rather to demonstrate the complexity of the motion of the tracking Fresnel lens. For simplicity, the path of the lens was calculated about a focal point on the roof of the C-MAX. As previously mentioned, in actuality the lens would not be focusing to a point, but rather an area atop the C-MAX. The path of the lens was determined by applying rotation matrices to the lens geometry based on the altitude and azimuth angles of the Sun about the focal point of the lens. Figure 53 depicts a screenshot of the output of the model at a single time step. As shown in the in the figure, the model illustrates the position of the sun at each time step, as well as the position that the tracking Fresnel Array must be oriented in, in order for the transmitted rays to land on the roof of the C-MAX.

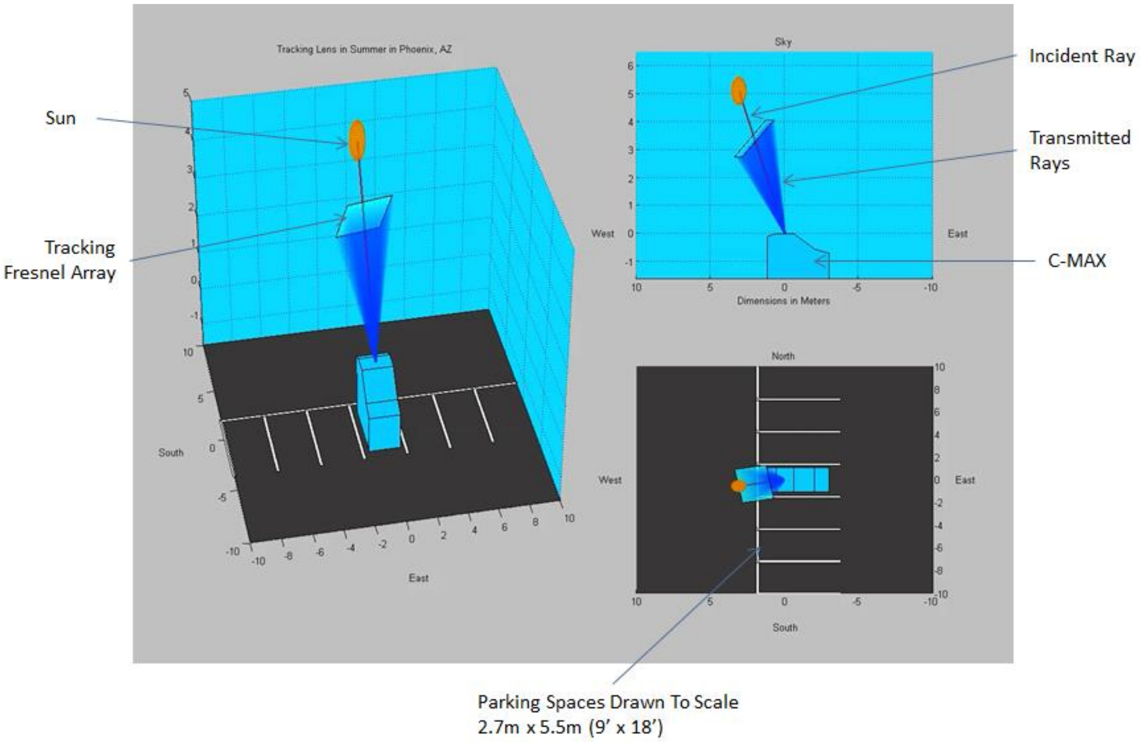

Parking Spaces Drawn To Scale
2.7m x 5.5m (9' x 18')

Figure 53. Tracking Lens Array Landscape

To calculate the energy produced by the Tracking Lens – Static Vehicle concept, the concept is simplified as a two-axis tracking flat panel PV array of the same area as the tracking Fresnel lens. For a two-axis tracking flat panel, the angle of the altitude-tracking axis is 90° minus solar altitude angle, β_1, in degrees; where 0° is a horizontal surface. The angle of the azimuth-tracking axis is simply equal to the solar azimuth angle, H. Since the Fresnel lens is only capable of concentrating direct beam radiation, the diffuse component of the solar radiation is neglected in the model. The energy output of the model will then be equal to the direct insolation incident on the tracking panel over the provided time step, times the area of the panel, less the PV efficiency of 21.5%, less the wiring efficiency of 93%, less an assumed optical efficiency of 85%.

Additional losses are incurred due to the incidence angle of the transmitted rays on the roof of the C-MAX. The current model simplifies the effect of the incidence angle by considering only the cosine of the elevation angle at each time step with respect to a horizontal flat surface; however, if more accurate models are to be developed, the effect of incidence angle and roof curvature should be taken into consideration. Although the model does trace the rays to the roof of the vehicle, the model does not take into account the effect of the non-uniformity of the light intensity on the performance of the PV array. Additionally, the model does not take into account the spectral non-uniformity due to chromatic aberration on the performance of the PV array. Finally the model does not take into account the thermal derate in PV efficiency associated with operating temperatures greater than 25˚C. A constant efficiency of 21.5%, which is lower than that of the rated efficiency of the arrays, is assumed on the premise that heat transfer mechanisms will be employed to control the PV array's temperature.

6.4.2 Results and Discussion

For comparison to the one sun analyses, the tracking lens analysis was initially run under similar input conditions; namely, a location of Atlanta, Georgia and a PV efficiency of 21.5%. As with the one sun models, a wiring efficiency of 93% was assumed, and an additional Fresnel lens efficiency of 85% was included. To gain a better understanding of the year-round energy generation, the tracking lens model was run for the months of January, July, and October, with a time step of 5 minutes. As previously mentioned, after speaking with several lens manufacturers, the largest discretized point focus Fresnel lens that any of them have manufactured is 9 square meters. For this reason, in the initial analysis the energy generation at each time step was scaled to the area of a 9 square meter collector. The daily energy generation values for each month were then used to produce the daily energy generation CDFs depicted in Figure 54.

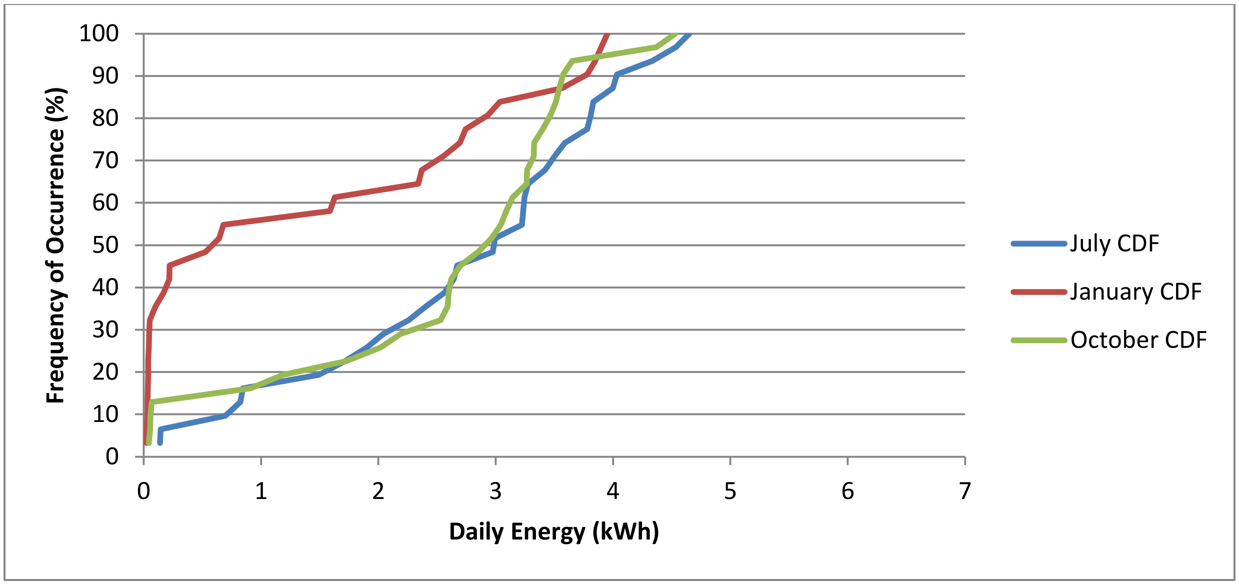

Figure 54. Daily Energy CDFs for 9m² Tracking Lens in Atlanta, GA

As shown in the figure, for a 9 m² tracking Fresnel lens in Atlanta, Georgia, the daily energy generation in the month of January is distributed around 0.59 kWh, with approximately 43% of the data lying above the average of 1.4 kWh. The daily energy generation in the month of July is distributed around 3.0 kWh, with approximately 54% of the data lying above the average of 2.7 kWh, and the daily energy generation for the month of October is distributed around 2.9 kWh, with approximately 66% of the data lying above the average of 2.6 kWh.

As with the one sun analyses, to better understand how the energy generation of a 9 m² tracking lens concept is effected by the level of daily insolation, the model was also run for Phoenix, Arizona and Seattle, Washington. Phoenix, Arizona is a location that experiences consistently high levels of daily insolation and Seattle, Washington, is a location that consistently experiences low levels of insolation due to cloud cover. To determine the range of daily energy values throughout the year, each city was run for the months of January, July, and

October. For Phoenix, Arizona, the daily energy generation CDF's for the months of January, July, and October are shown in Figure 55. For Seattle, Washington, the daily energy generation CDF's for the months of January, July, and October are shown in Figure 56.

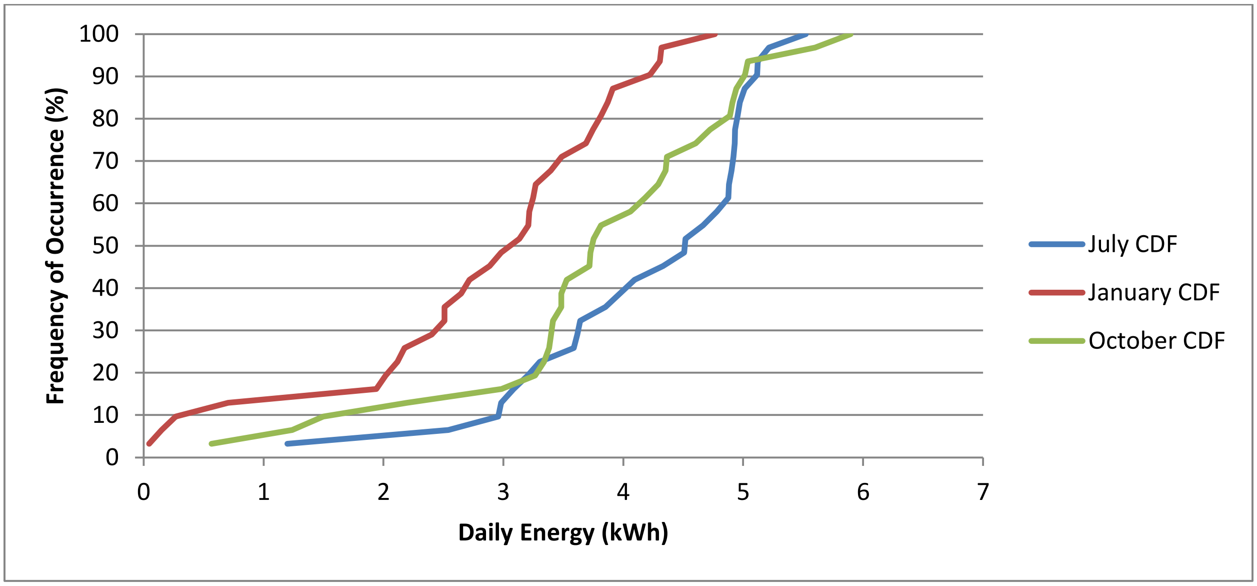

Figure 55. Daily Energy CDFs for 9m² Tracking Lens in Phoenix, AZ

As shown in Figure 55, for a 9 m² tracking Fresnel lens in Phoenix, Arizona, the daily energy generation in the month of January is distributed around 3.1 kWh, with approximately 56% of the data lying above the average of 2.8 kWh. The daily energy generation in the month of July is distributed around 4.5 kWh, with approximately 57% of the data lying above the average of 4.2 kWh, and the daily energy generation for the month of October is distributed around 3.7 kWh, with approximately 46% of the data lying above the average of 3.8 kWh.

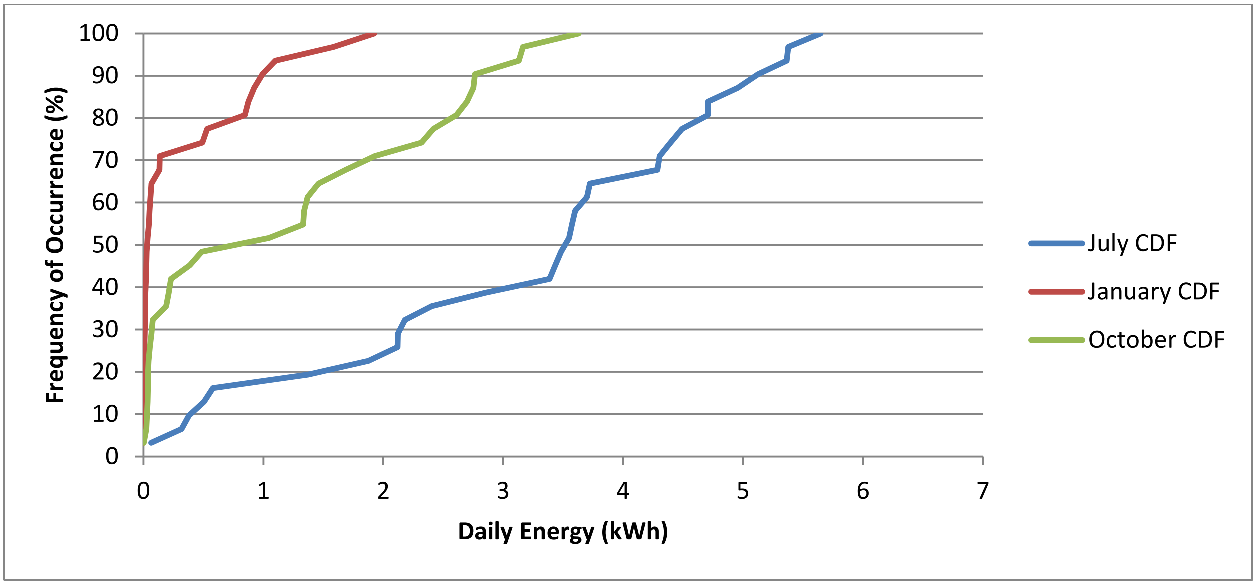

Figure 56. Daily Energy CDFs for 9m² Tracking Lens in Seattle, WA

As shown in Figure 56, for a 9 m² tracking Fresnel lens in Seattle, Washington, the daily energy generation in the month of January is distributed around 0.03 kWh, with approximately 27% of the data lying above the average of 0.32 kWh. The daily energy generation in the month of July is distributed around 3.5 kWh, with approximately 59% of the data lying above the average of 3.2 kWh, and the daily energy generation for the month of October is distributed around 0.77 kWh, with approximately 47% of the data lying above the average of 1.2 kWh. The results of this analysis for each city and month are summarized in Table 13.

.

Table 13. Summary of 9 m² Tracking Lens Concept

City	Month	Daily Energy 50% Frequency of Occurrence (kWh)	Average Daily Energy (kWh)	% of Data Above Average
Atlanta, GA	January	0.59	1.4	43
	July	3.0	2.7	54
	October	2.9	2.6	66
Phoenix, AZ	January	3.1	2.8	56
	July	4.5	4.2	57
	October	3.7	3.8	46
Seattle, WA	January	0.03	0.32	27
	July	3.5	3.2	59
	October	0.77	1.2	47

A similar analysis was conducted to determine the minimum tracking Fresnel lens area that would be necessary to reach the daily energy generation goal of 7.6 kWh. For the analysis it was assumed that the highest levels of daily direct beam insolation occur in the month of July. As such, the minimum tracking Fresnel lens area that would be necessary to reach the daily energy generation goal of 7.6 kWh would be the minimum tracking Fresnel lens area necessary to reach the daily energy generation goal in the month of July. From the analysis, it was determined that a 21 m² tracking Fresnel lens would be necessary in Seattle, Washington to reach a daily average of 7.4 kWh in July, with the CDF of daily energy values centered around 8.2 kWh and with 59% of the values above average. In Atlanta, Georgia, a 25 m² tracking Fresnel lens would necessary to reach a daily average of 7.6 kWh in July, with the CDF of daily energy values centered around 8.3 kWh and with 54% of the values above average. Likewise, in Phoenix, Arizona, a 16 m² tracking Fresnel lens would be necessary to reach a daily average of 7.5 kWh in July, with the CDF of daily energy centered around 8.0 kWh and with 57% of the values above average. An early preliminary run of this study which neglected the effect of the incidence angle losses suggested that a much smaller lens area would be necessary. The results of this study are provided in Appendix C.

As with the tracking vehicle – static lens concept, the primary concern with the static vehicle – tracking lens concept is safety. Exposure to concentrated solar radiation can pose serious and potentially fatal hazards to users and any other people or animals that may come into contact with the system. In addition, concentrated solar radiation presents the risk of destroying any material not suited to handle such high levels of radiative flux.

The tracking lens in this concept increases the efficiency of the design; however, there are still considerable losses due to the incidence angle of the concentrated radiation on the roof of the vehicle. The losses due to the incidence angle are smallest at larger solar elevation angles, and as with the tracking vehicle – static lens concept, the size of the lens increases considerably to maximize energy generation at the larger solar elevation angles. While the size of the tracking lens necessary to reach the daily energy generation goal is considerably smaller than that of the tracking vehicle – static lens concept, the area requirement for such a system is still not practical. The area of an average parking space is approximately 15 m^2, and in addition to the space requirement for the lens to track, the best case scenarios for Atlanta and Phoenix require 25 m^2 and 16 m^2 lenses, respectively.

The tracking mechanism for such a design is also overly complex. As previously stated, the lens must be articulated in such a way that the distance from the roof of the C-MAX to the center of the lens remains constant, as changing this distance will affect the concentration level. As the driving path for the tracking vehicle – static lens concept varied throughout the year, so will the path that the lens must traverse in order to track the sun. To further complicate matters, the path that the lens must traverse will be location dependent. Articulating a Fresnel lens of the area necessary to reach the daily energy goal in such a manner is not impossible, but is considerably more complex than traditional two-axis tracking mechanisms.

Again, there are certain issues that are common to all CPV systems, and when considering tracking systems, this primarily deals with daily direct insolation levels. As previously stated, current concentrating optics are only capable of concentrating direct beam radiation. During periods of heavy cloud cover the direct beam irradiance can drop considerably, thereby drastically reducing the electricity generating capabilities of CPV systems. As a result, locations, like Seattle, Washington, which experience whole seasons of heavy cloud cover, are not particularly suitable for CPV systems.

6.5 Fiber Optic Design

The fiber optic design involves a two-axis tracking array of small Fresnel lenses. The concentrated light from each Fresnel lens is coupled into an optical fiber and transmitted to the roof of the C-MAX. An illustration of the tracking array of Fresnel lenses and the bundle of optical fibers used to transmit the concentrated light to the vehicle is shown in Figure 57. As with the other designs, the size of the Fresnel lens array necessary to reach the 7.6 kWh daily energy goal is location specific. Locations with very high levels of direct insolation will require smaller lens areas, and locations at higher latitudes and locations with lower levels of daily direct insolation will require larger lenses. Unlike the other designs, the array will be made of smaller individual Fresnel lenses, which will likely be more easily manufacturable and will also likely have a higher optical efficiency than the aforementioned discretized lenses.

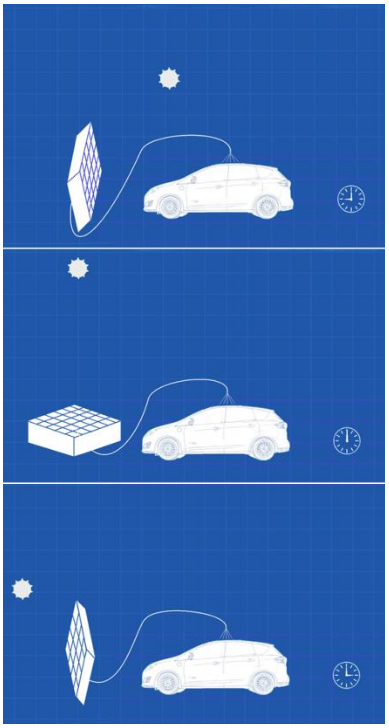

Figure 57. Illustration of Fiber Optic Concept

The fiber optic concept was designed with safety, adaptability, and modularity in mind. Since the concentrated light is contained within the optical fiber until the light exists the fiber, there is a significantly lower risk of people, animals, or other objects being subject to the concentrated light. When the concentrated light is no longer needed, the collector can be quickly turned away from the sun, and since the collector can only concentrate direct beam radiation, no light will be emitted from the optical fibers. Since the fibers are flexible, the incidence angle of the concentrated light on the PV can be entirely controlled regardless of the tracking path of the collector. The tracking mechanism of the collector is also greatly simplified, as the focal point of the lens is no longer constrained to the roof of the vehicle. There are however additional losses to be considered with the fiber optic design due to the coupling efficiency and the attenuation of light within the fiber.

6.5.1 Modeling

As with the Tracking Lens – Static Vehicle concept, a 3D model was developed not to calculate the energy produced by the Fiber Optic concept, but rather to illustrate the motion of the tracking lens array over the course of the day. As shown in Figure 58, a simple clevis structure is sufficient to support the Fresnel lens array. Since the focal points of the Fresnel lenses are not constrained to the roof of the vehicle, the Sun can be effectively tracked by simply rotating the clevis about an axis perpendicular to the ground to track the Sun's azimuth, and by rotating the Fresnel lens array about its supporting axis, parallel to the ground, to track the Sun's altitude.

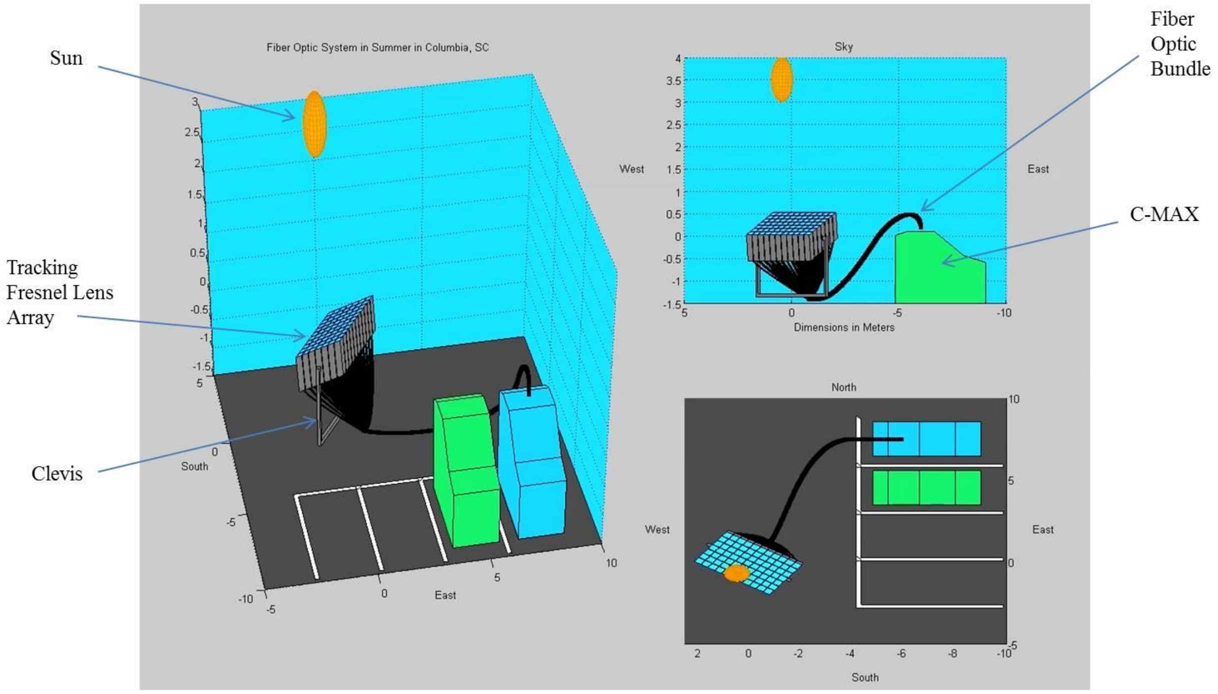

Figure 58. Fiber Optic System Landscape

To calculate the energy produced by the Fiber Optic concept, the concept is simplified as a two-axis tracking flat panel PV array of the same area as the tracking Fresnel lens array. For a two-axis tracking flat panel, the angle of the altitude-tracking axis is 90° minus solar altitude angle, β_1, in degrees; where 0° is a horizontal surface. The angle of the azimuth-tracking axis is simply equal to the solar azimuth angle, H. Since the Fresnel lens array is only capable of concentrating direct beam radiation, the diffuse component of the solar radiation is neglected in the model. The direct component of the Sun's radiation will always be perpendicular to the two-axis tracking flat panel, and as a result the energy output will be equal to the direct insolation incident on the panel over the provided time step, times the area of the panel, less the PV efficiency of 21.5%, less the wiring efficiency of 93%. Additional reductions in efficiency due to the 85% optical efficiency of the Fresnel lenses and the 60% fiber optic efficiency are also included in the energy calculations.

For such a system to be viable, considerable optical design work would still be necessary. To date, the model groups all of the losses in the fiber optic system into losses in the Fresnel lens and losses in the optical fiber. In actuality, the losses will be highly dependent on the system design. Arnaoutakis, Marques-Hueso et al. (2013) identified the optical losses in such a system as:

- Fresnel reflection on both surfaces of the primary lens ①,②
- Reflection at the front surface of the secondary optic ③
- Chromatic and spherical aberration from the primary lens ④
- Disruption of the total internal reflection in the secondary optic ⑤
- Disruption of the total internal reflection in the fiber optic ⑥
- Absorption in the fiber optic
- Reflection at the end of the fiber ⑦.

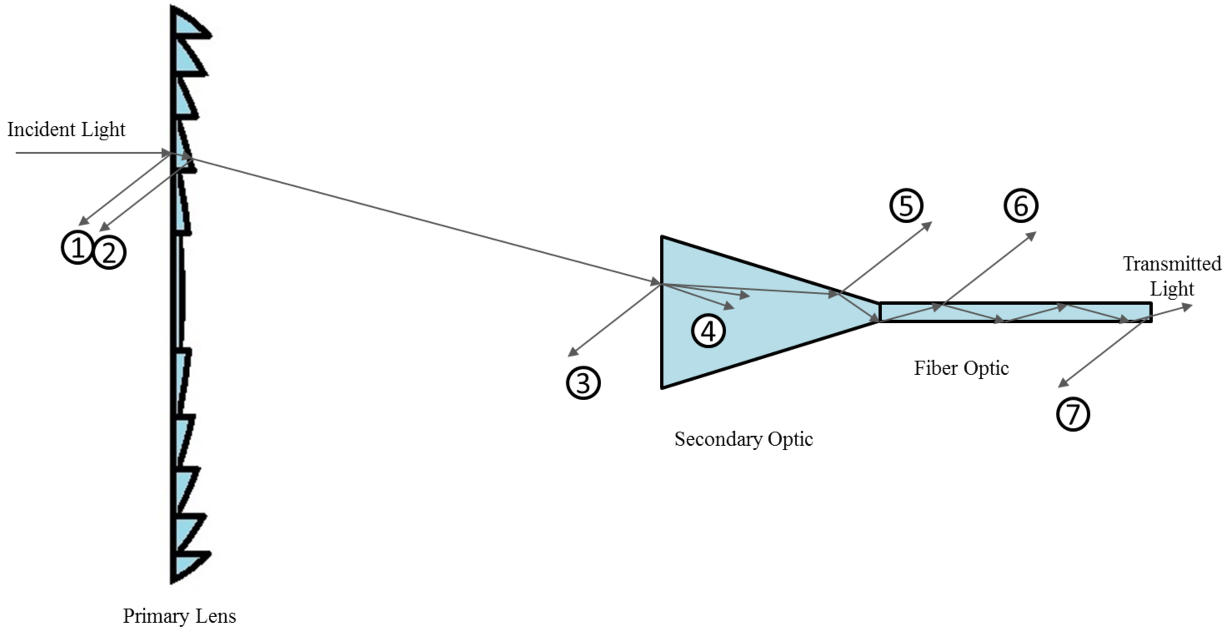

Figure 59. Optical Losses in Fiber Optic Concentrating System, Adapted from: (Arnaoutakis, Marques-Hueso et al. 2013)

The secondary optic shown in Figure 59 is not entirely necessary, but the use of such an optic will increase the coupling efficiency of light into the fiber optic and also to reduce the tolerance necessary for the tracking system to effectively focus light into the fiber optic (Kurtz 2012). Ray tracing simulations have shown theoretical coupling efficiencies of better than 94% for a lens-taper-fiber system similar to that shown in Figure 59 (Arnaoutakis, Marques-Hueso et al. 2013). In real world conditions, maximum experimental coupling efficiencies of only 60%, for a side-polished and fused bundle of 19 fibers (Liang, Fraser Monteiro et al. 1998), and 38% for a single fiber (Nakamura 2011) have been demonstrated. For an extended review of studies conducted on the transmission of concentrated solar energy via optical fibers see reference (Kandilli and Ulgen 2009).

While the optical efficiency of the fiber optic concept may lower than that of the other concepts, additional design considerations may be made to boost the overall system efficiency. The f-number of the primary lens and the acceptance angle of the secondary lens should be optimized so as to maximize the coupling efficiency to the fiber. The amount of sunlight that can be accepted by an optical fiber is limited by the numerical aperture of the fiber. The numerical aperture is a dimensionless number used to characterize the range of angles over which an optic can accept light. While very high numerical apertures are achievable today, (Arnaoutakis, Marques-Hueso et al. 2013) have shown that systems using primary optics with higher f-numbers and secondary optics with an acceptance angles that utilize 50% or less of the numerical aperture of the fiber result in the highest coupling efficiencies for solar applications. Additional considerations, like infrared-absorbing filters, such as those described by (Firat and Beyene 2012), may significantly reduce the heating of the PV cells by reducing the proportion of unusable IR radiation incident on the cells. The addition of such features will surely incur additional costs; as such, in designing such a system, it is necessary to not only consider the impact of the system's performance, but also the impact on the system's cost.

6.5.2 Results and Discussion

For comparison to the one sun analyses, the fiber optic analysis was initially run under similar input conditions; namely, a location of Atlanta, Georgia and a PV efficiency of 21.5%. As with the one sun models, a wiring efficiency of 93% was assumed, and an additional Fresnel lens efficiency of 85% was included. To gain a better understanding of the year-round energy generation, the fiber optic model was run for the months of January, July, and October, with a time step of 5 minutes. For comparison to the tracking lens analysis, the initial analysis was run with the energy generation at each time step scaled to the area of a 9 square meter collector. The daily energy generation values for each month were then used to produce the daily energy generation CDFs depicted in Figure 60.

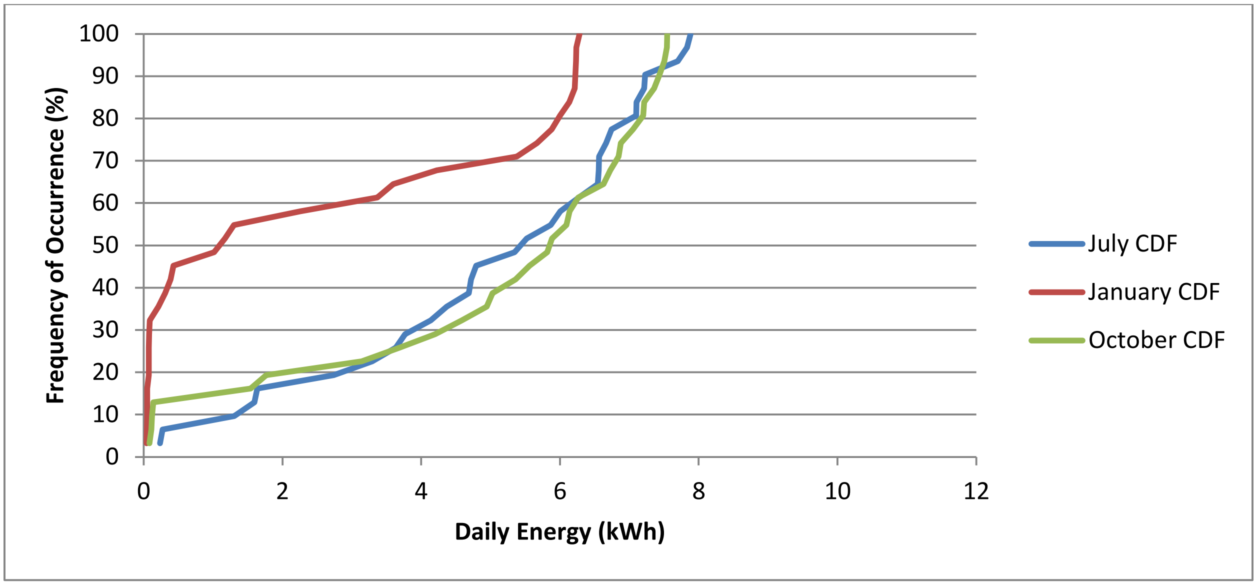

Figure 60. Daily Energy CDFs for 9m² Fiber Optic Concept in Atlanta, GA

As shown in the figure, for a 9 m² collector in Atlanta, Georgia, the daily energy generation in the month of January is distributed around 1.1 kWh, with approximately 41% of the data lying above the average of 2.6 kWh. The daily energy generation in the month of July is distributed around 5.4 kWh, with approximately 54% of the data lying above the average of 5.0 kWh, and the daily energy generation for the month of October is distributed around 5.9 kWh, with approximately 61% of the data lying above the average of 5.0 kWh.

As with the tracking lens analysis, to better understand how the energy generation of a 9 m² collector for the fiber optic concept is effected by the level of daily insolation, the model was also run for Phoenix, Arizona and Seattle, Washington. Again, Phoenix, Arizona is a location that experiences consistently high levels of daily insolation and Seattle, Washington, is a location that consistently experiences low levels of insolation due to cloud cover. To determine the range of daily energy values throughout the year, each city was run for the months of January, July, and October. For Phoenix, Arizona, the daily energy generation CDF’s for the months of January, July, and October are shown in Figure 61. For Seattle, Washington, the daily energy generation CDF’s for the months of January, July, and October are shown in Figure 62.

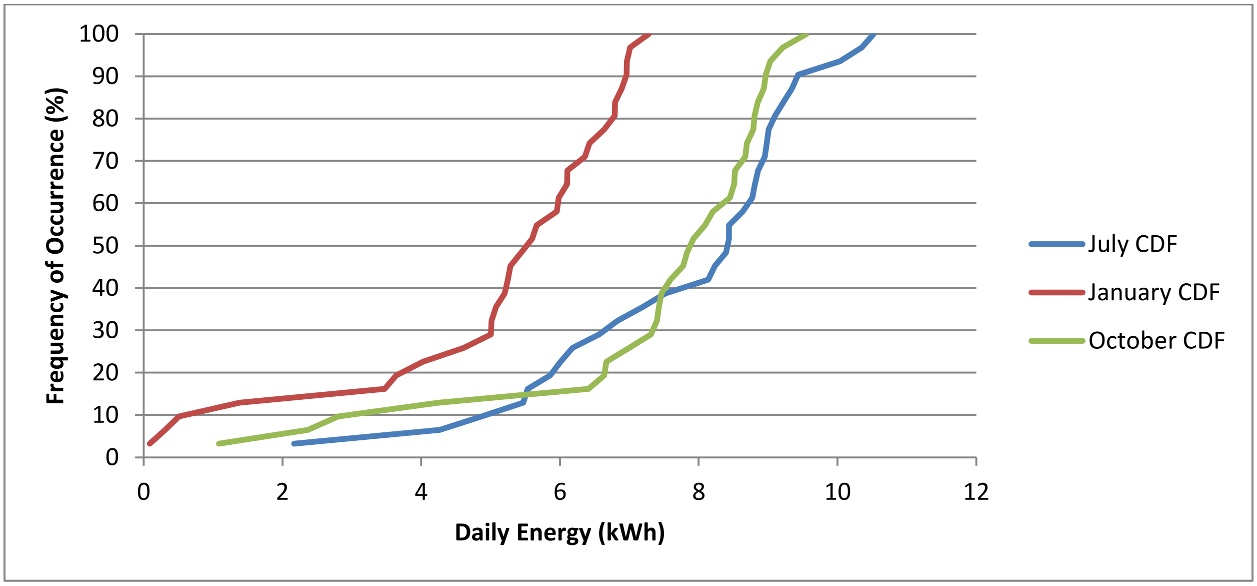

Figure 61. Daily Energy CDFs for 9m² Fiber Optic Concept in Phoenix, AZ

As shown in Figure 61, for a 9 m² collector in Phoenix, Arizona, the daily energy generation in the month of January is distributed around 5.5 kWh, with approximately 64% of the data lying above the average of 5.1 kWh. The daily energy generation in the month of July is distributed around 8.4 kWh, with approximately 60% of the data lying above the average of 7.7

kWh, and the daily energy generation for the month of October is distributed around 7.9 kWh, with approximately 68% of the data lying above the average of 7.4 kWh.

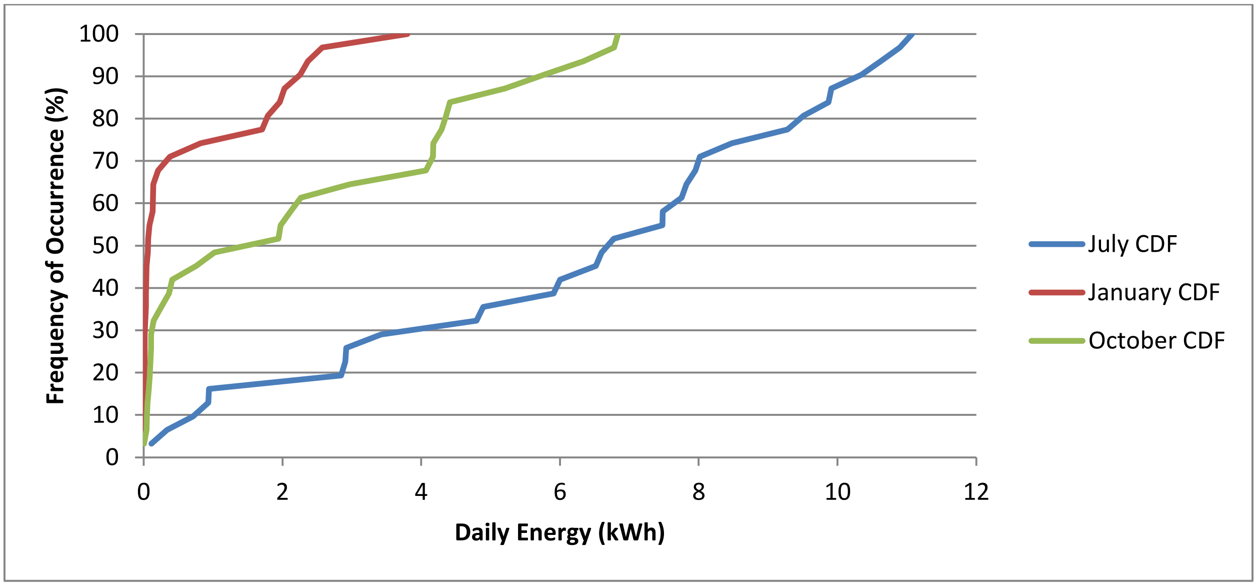

Figure 62. Daily Energy CDFs for 9m² Fiber Optic Concept in Seattle, WA

As shown in Figure 62, for a 9 m² collector in Seattle, Washington, the daily energy generation in the month of January is distributed around 0.06 kWh, with approximately 27% of the data lying above the average of 0.67 kWh. The daily energy generation in the month of July is distributed around 6.7 kWh, with approximately 57% of the data lying above the average of 6.2 kWh, and the daily energy generation for the month of October is distributed around 1.5 kWh, with approximately 39% of the data lying above the average of 2.3 kWh. The results of this analysis for each city and month are summarized in Table 14.

Table 14. Summary of 9 m² Collector for Fiber Optic Concept

City	Month	Daily Energy 50% Frequency of Occurrence (kWh)	Average Daily Energy (kWh)	% of Data Above Average
Atlanta, GA	January	1.1	2.6	41
	July	5.4	5.0	54
	October	5.9	5.0	61
Phoenix, AZ	January	5.5	5.1	64
	July	8.4	7.7	60
	October	7.9	7.4	68
Seattle, WA	January	0.06	0.67	27
	July	6.7	6.2	57
	October	1.5	2.3	39

A similar analysis was conducted to determine the minimum collector area that would be necessary to reach the daily energy generation goal of 7.6 kWh. For the analysis it was assumed that the highest levels of daily direct beam insolation occur in the month of July. As such, the minimum collector area that would be necessary to reach the daily energy generation goal of 7.6 kWh would be the minimum collector area necessary to reach the daily energy generation goal in the month of July. From the analysis, it was determined that an 11 m² collector would be necessary in Seattle, Washington to reach a daily average of 7.7 kWh in July, with the CDF of daily energy values centered around 8.4 kWh and with 60% of the values above average. In Atlanta, Georgia, a 13.5 m² collector would necessary to reach a daily average of 7.5 kWh in July, with the CDF of daily energy values centered around 8.2 kWh and with 54% of the values above average. Likewise, in Phoenix, Arizona, a 9 m² tracking Fresnel lens would be necessary to reach a daily average of 7.6 kWh in July, with the CDF of daily energy centered around 8.2 kWh and with 57% of the values above average.

As previously stated, the fiber optic concept was designed with safety, adaptability, and modularity in mind. The safety issues of the previous designs have been mitigated by containing the concentrated light. Since the concentrated light is contained within the system until the light exists the fiber, there is a significantly lower risk of people, animals, or other objects being subject to the concentrated light. When the concentrated light is no longer needed, the collector can be quickly turned away from the sun, and since the collector can only concentrate direct beam radiation, no light will be emitted from the optical fibers. While there are additional losses associated with the use of fiber optics, the overall losses have been reduced by eliminating the considerable losses resulting from the incidence angle of the concentrated light on the PV. Since the fibers are flexible, the incidence angle of the concentrated light on the PV can be entirely controlled regardless of the tracking path of the collector. The flexible cables also eliminate the necessity of the collector being immediately proximate to the vehicle, thereby alleviating the space requirement of the collector. Finally, the tracking mechanism of the collector is also greatly simplified with respect to the static vehicle – tracking lens concept. Since the focal point of the lens is no longer constrained to the roof of the vehicle, a simple two-axis tracking mechanism can be employed.

Again, there are certain issues that are common to all CPV systems, and when considering tracking systems, this primarily deals with daily direct insolation levels. As previously stated, current concentrating optics are only capable of concentrating direct beam radiation. During periods of heavy cloud cover the direct beam irradiance can drop considerably, thereby drastically reducing the electricity generating capabilities of CPV systems. As a result, locations, like Seattle, Washington, which experience whole seasons of heavy cloud cover, are not particularly suitable for CPV systems.

CHAPTER 7: THERMAL MANAGEMENT OF CPV SYSTEMS

When designing a CPV system, the heat transfer mechanism necessary to effectively cool the PV cells is of particular importance. Due to the limited efficiency of today's PV technologies, a considerable portion of the sunlight incident on a PV cell is converted into thermal rather than electrical energy. This thermal energy, if not managed properly, can result in elevated junction temperatures within the PV cell resulting in a reduction in the cells operating efficiency. Long term exposure to elevated temperatures may result in permanent damage to the PV cell. Royne, Dey et al. (2005) have outlined the major design considerations for cooling of PV cells as:

- Cell Temperature
- Uniformity of Temperature
- Reliability and Simplicity
- Usability of Thermal Energy
- Pumping Power
- Material Efficiency.

As previously mentioned, cell temperature addresses the junction temperature of the cell and the associated decrease in cell efficiency with increase in temperature. Uniformity of temperature addresses the uniformity of the temperature distribution across individual cells as well as across an array of cell. Baig, Heasman et al. (2012) have shown the efficiency of a single cell to drop with a non-uniform temperature distribution. The uniformity of temperature for an array of cells is of particular importance when the cells are connected in series. With cells wired in series, the current across all of the cells is limited by the cell generating the lowest current. As a result, if a single cell has a reduced efficiency due to an elevated junction temperature, the efficiency of all cells wired in series with it will also be reduced, resulting in additional heat generation. The reliability and simplicity design consideration is very straightforward. The heat transfer mechanism should be as uncomplicated as possible, while at the same time capable of dealing with possible worst-case or failure scenarios. Usability of thermal energy and pumping power are particularly relevant to active cooling mechanisms, and deal with the energy that could be recovered and the energy that must be expended by the system, respectively. Finally, materials for the heat transfer mechanism should be chosen, such that the cost, weight and embodied energy are minimized.

There are also several design considerations that are unique to cooling PV cells on board a vehicle. In addition to the weight consideration, there are size and geometry constraints. As the PV cells are on the roof of the vehicle it is necessary that the heat exchanger for the cooling system also fit on the roof of the vehicle, while not adding unsightly bulk. The service life of the cooling system should be comparable to that of the vehicle, and if maintenance is required it should be on intervals comparable to that of regular vehicle maintenance. Passenger comfort should be taken into consideration, by minimizing the heat transferred into the cabin of the vehicle. Mezrhab and Bouzidi (2006) have developed a computational model for the thermal comfort in the cabin of a passenger vehicle that may be useful for this purpose. In addition to passenger comfort, the passenger safety should be taken into consideration. Failure modes of the system should also account for failure modes that are unique to a vehicle, such as crashes.

The non-uniform nature of irradiance levels with time and geographic location present a considerable design challenge for a CPV cooling mechanism. As previously discussed, the size of the collector area necessary for the various CPV designs is dependent on geographic location and time of year. For the fiber optic concept, it was determined that for the month of July, a 13.5 m^2 collector would be necessary to reach the stated energy goal in Atlanta, Georgia, and a 9 m^2 collector would be necessary in Phoenix, Arizona. Since the PV area on the roof of the vehicle is a constant 1.2 m^2, the concentration ratios at each geographic location will vary. As a result, the thermal energy that must be removed from the system will also vary. A simple calculation shows that for 13.5 m^2 collector, if a solar irradiance of 1000 W/ m^2 is assumed, the solar power incident on the PV array is 13,500 W, of which only 20% can be converted to electricity by the PV. As a result 10,800 W of heat must be dissipated by the cooling system. Using the same assumptions for a 9 m^2 collector, 7,200 W of heat must be dissipated by the cooling system. While these approximations are greatly simplified, they do demonstrate the difference in thermal load that may be experienced in different geographic locations. Likewise, solar irradiance will vary considerably with time, resulting in the same effect, even at the same geographic location.

Additional design challenges stem from the arrangement of PV cells on the roof. To maximize the utilization of the area available on the roof of the C-MAX, the PV cells must be arranged as densely as possible. While this results in a higher power output per unit area, it also poses special problems in removing heat from the cells, particularly under concentrated sunlight. When PV cells are closely packed in an array, the only area available to remove heat from the cell is that of the cell itself. This generally necessitates the need for active cooling (Royne, Dey et al. 2005). Designing an active cooling system for the CPV concept is beyond the scope of this project; however, many examples of the design, modeling, and experimental validation of active cooling systems for CPV applications can be found in the literature.

Solar Systems PTY Ltd. utilizes a water cooling circuit patented by (Lasich 2006) to maintain the average temperature of a densely packed array of 24 series-connected 1.0 x 1.5 cm

PV cells at 35.52°C under 340 times concentration. The cooling circuit required 86 W to pump the water at a flow rate of 33.44 liters per minute (P.J. Verlinden 2001).

Verlinden, Sinton et al. (1991) have designed, fabricated, and tested a monolithic PV module with an integrated cooling circuit to meet the needs of a very large Fresnel CPV system. The module consists of a 36 cm^2 array of PV cells designed to operate under 200 times concentration, and an integrated cooling plate. The heat to be removed from the cells is 540W, with 720W peaks. The cooling plate is capable of maintaining the PV cell temperature at 58.9°C at a water inlet temperature of 25°C and a flow rate of 0.76 liters per minute. Pump power requirements are not provided.

Many active cooling systems for CPV applications also seek make use of some of the thermal energy from the system thus increasing the solar conversion efficiency. Such systems can generally be grouped into photovoltaic/thermal (PV/T) systems, which seek to remove thermal energy from the PV array and utilize it elsewhere and photovoltaic/thermoelectric generator systems (PV/TEG) systems, which utilize TEGs to generate additional energy. Chow (2010) conducted an extensive review of the various PV/T systems that have been theoretically, numerically, and experimentally developed over the past thirty years; concluding that there exists a vast array of PV/T applications, all of which depend on geographic location and the particular application. For additional literature on PV/TEG systems, see references: (Kraemer, McEnaney et al. 2012), (Kraemer, Poudel et al. 2011), (Chávez-Urbiola, Vorobiev et al. 2012), (Khattab and El Shenawy 2006), (Wang, Han et al. 2011), and (Rockendorf, Sillmann et al. 1999).

CHAPTER 8: RECOMMENDATIONS AND FUTURE WORK

At this point, regenerative shock absorbers, solar PV, and CPV technologies have been investigated. Other technologies such as wind turbines and piezoelectrics were also considered, but quickly eliminated due to their net energy expenditure, and low energy densities, respectively. It was determined that regenerative shock absorbers, although capable of capturing energy that would otherwise be wasted, do not generate sufficient energy for a typical driver to meet the daily energy goal. Furthermore, by only having the capability of regenerating 0.3% of the daily energy goal, they do not contribute any significant amount of energy to the daily energy goal and are therefore not particularly well suited for consideration as a supplement to the other technologies investigated.

Covering the body panels of the vehicle with PV was shown to have the potential of achieving a daily energy generation near that of the daily energy generation goal for locations and times of year with high levels of daily solar insolation. During times of the year with low levels of daily solar insolation, particularly low levels of daily direct insolation, standard PV panels still have merit. Unlike CPV systems, standard PV panels are capable of utilizing direct beam and diffuse solar radiation. As a result, standard PV systems tend to perform better than CPV systems during periods of heavy cloud cover when direct beam radiation levels are very low. As shown in Table 10 and Table 11, the daily energy contribution of the body panels covered in PV in the month of January is on the order of 1 kWh. While this is not sufficient to reach the daily energy goal, it may well suited for consideration as a supplement to the other technologies investigated.

In addressing the remaining stated design criteria, covering the body panels of the vehicle in PV requires no additional off-vehicle technologies or hardware. In this way, the vehicle utilizes the maximum amount of on-vehicle technology as possible. Covering the body panels of a vehicle in PV is not restricted to PHEVs, and is feasible for most any type of vehicle. The only limitations of this concept are the area and geometry of the body panels on the different vehicles. That said, the concept addresses the criteria of being applicable to PHEVs and BEVs. Covering the body panels of a vehicle in PV is not particularly innovative. Car manufacturers including Toyota, Chevy, Audi, Mazda, and Fisker have all utilized small PV panels as auxiliary power sources on production level vehicles. In addition, competitions like the World Solar Challenge have led to considerable efforts in designing specialized cars which rely on only PV generated power to operate (Challenge 2014). In this way, the concept by itself does not address the criteria of being innovative.

Several CPV concepts were outlined and modeled. Since it was determined that the concentrator would best be situated off of the vehicle, the Tracking Vehicle – Static Lens concept was developed to maximize the use of on-vehicle technologies by having the vehicle perform the tracking. Unfortunately, by not having a tracking lens the reflection losses in the lens at low solar elevation angles were significant – rendering the concept infeasible. The remaining concepts did not require the use of as much on-vehicle technology, as a mechanism separate from the vehicle performed the tracking. Of the remaining two concepts, the fiber optic concept was demonstrated to be the most feasible. In addressing the remaining stated design criteria, the fiber optic CPV system would be applicable to both PHEVs and BEVs, so long as the necessary heat transfer mechanisms and additional hardware are in place. While the application of PV alone to a vehicle is not all that innovative, the concept of concentrated PV on a vehicle has considerable novelty. All things considered, the fiber optic CPV concept is the concept that best meets the stated design criteria.

That being said, there are still many limitations to the design. The concept was shown to have the potential of reaching the daily energy generation goal for locations and times of year with high levels of daily solar insolation; however, during times of the year with low levels of daily solar insolation the concept underperforms if at all. In addition, since CPV systems are only capable of concentrating direct beam radiation, cloud cover can drastically affect the performance of the system. This aspect of the system affects the reliability of the system in any location, and also limits the feasibility of such a system to locations with consistently high levels of daily direct insolation. To enhance the performance of the fiber optic CPV system during periods of low direct beam radiation, it may be worth investigating how supplementing the system with the addition of standard PV to the remaining body panels improves performance.

For the fiber optic CPV system to be viable, considerable optical design work would still be necessary. To date, the model groups all of the losses in the fiber optic system into losses in the Fresnel lens and losses in the optical fiber. In actuality, the losses will be highly dependent on the system design. Arnaoutakis, Marques-Hueso et al. (2013) identified the optical losses in such a system as:

Fresnel reflection on both surfaces of the primary lens ①,②

Reflection at the front surface of the secondary optic ③

Chromatic and spherical aberration from the primary lens ④

Disruption of the total internal reflection in the secondary optic ⑤

Disruption of the total internal reflection in the fiber optic ⑥

Absorption in the fiber optic

Reflection at the end of the fiber ⑦.

These losses are illustrated in Figure 59. The secondary optic shown in Figure 59 is not entirely necessary, but the use of such an optic will increase the coupling efficiency of light into the fiber optic and also to reduce the tolerance necessary for the tracking system to effectively focus light into the fiber optic (Kurtz 2012). Ray tracing simulations have shown theoretical coupling efficiencies of better than 94% for a lens-taper-fiber system similar to that shown in Figure 59 (Arnaoutakis, Marques-Hueso et al. 2013). In real world conditions, maximum experimental coupling efficiencies of only 60%, for a side-polished and fused bundle of 19 fibers (Liang, Fraser Monteiro et al. 1998), and 38% for a single fiber (Nakamura 2011) have been demonstrated. For an extended review of studies conducted on the transmission of concentrated solar energy via optical fibers see reference (Kandilli and Ulgen 2009).

To enhance the coupling efficiency of the fiber optic concept, the reflection losses and tracking error tolerance of the primary and secondary lenses may be improved using non-imaging lens design. The performance of the PV may also be enhanced through non-imaging lens design by reducing the effects of chromatic aberration and increasing the flux uniformity of the concentrated light. Such designs must be analyzed using ray-tracing software (Miller and Kurtz 2011). Such an analysis has yet to be conducted. In addition to the optical properties of the lenses, the mechanical properties of the lens should be considered. Particular attention should be paid to the primary concentrating Fresnel lens, as it will be exposed to the elements. Rainhart and Schimmel Jr (1975) have shown the flexural strength of PMMA to be reduced by 51% after 17 years of outdoor exposure. Physical aging or densification of the polymers may affect many mechanical characteristics, including: dimensions, Poisson’s ratio, yield stress, mechanical modulus, and mechanical dissipation. Changes in these mechanical characteristics may in turn affect optical characteristics such as optical alignment. Mechanical properties of the lens have yet to be taken into consideration.

While the real-world coupling efficiency of the fiber optic concept may low, on the order of 60% (Liang, Fraser Monteiro et al. 1998), additional design considerations may be made to boost the overall system efficiency. The use of infrared-absorbing filters, such as those described by (Firat and Beyene 2012), may significantly reduce the heating of the PV cells by reducing the proportion of unusable IR radiation incident on the cells. The addition of such features will surely incur additional costs, and as such in designing such a system, it is necessary to not only consider the impact of the system’s performance, but also the impact on the system’s cost.

In modeling the fiber optic concept, a number of assumptions and simplifications had to be made to account for the yet to be determined effects of chromatic aberration, flux uniformity, etc. At present, the model does not take into account the effect of the non-uniformity of the light intensity on the performance of the PV array. The model also neglects the spectral non-uniformity due to chromatic aberration on the performance of the PV array. Reflection losses in the system are accounted for only in the optical efficiency of the Fresnel lens, 85%, and the coupling efficiency to the fiber optic, 60%. Misalignment errors are not accounted for. Finally, as discussed in Chapter 7, a heat transfer mechanism will need to be devised to manage the heat generated by the concentrating system. At present, the model does not take into account the variation in PV efficiency resulting from varying cell junction temperatures. A constant PV efficiency of 21.5% is assumed. As the necessary additional design work is carried out, the model should be updated accordingly so as to generate more accurate results.

Another important metric that should be taken into consideration as the necessary additional design work is carried out is the energy expended by the system during operation. For the fiber optic, or most any other CPV system to be feasible, some form of tracking mechanism is necessary. Although passive solar tracking mechanisms have been devised, such as that designed by Clifford and Eastwood (2004), generally an active tracking mechanism will be necessary for CPV applications. In addition, since the concentrated light will be incident on a closely packed array of cells, active cooling will likely be necessary (Royne, Dey et al. 2005). As energy will then necessarily be expended by the tracking and heat transfer mechanisms, the net energy generated by the system will be reduced. Additional losses due to the on-vehicle mass of the system will also be incurred. For more accurate daily energy calculations, these expenditures should be taken into consideration in the model.

Many commercial and utility scale CPV systems utilize high efficiency multi-junction solar cells rather than monocrystalline or other types of PV technologies. Multi-junction PV cells are very expensive; however, at high levels of concentration they become more cost-effective to utilize (Royne, Dey et al. 2005). The performance of the fiber optic CPV concept may be enhanced by utilizing a smaller area of high efficiency multi-junction PV cells. There are many benefits to using multi-junction PV over monocrystalline -the first being the inherent higher efficiency. A higher efficiency PV cell will convert a greater portion of the incident radiation into useable electricity and therefore less thermal energy will be generated for the same level of radiative flux. If the same collector is used to concentrate onto the smaller area of high efficiency cells, obviously there will be a higher level of radiative flux. However, the thermal energy that must be dissipated is the same, and since the area if the high efficiency cells is smaller there is a greater area available over which to dissipate the heat. If multi-junction PV cells can be shown to be cost effective and readily available for mass production, they demonstrate great potential. While the cost of multi-junction PV cells is addressed, an economic analysis of the concepts considered in this paper is beyond the scope of this project. Further work is necessary to prove or disprove the financial feasibility of such a concept.

The overall goal of this project was to reduce the greenhouse gas emissions that are associated with the charging of electrified passenger vehicles. While it has been suggested that utilizing clean renewables to reach the daily energy goal of 7.6 kWh may the greenhouse gas emissions of a typical driver by four metric tons annually (Ford 2014), an actual environmental impact of the concepts was beyond the scope of this project. Further research will be necessary to determine the actual environmental impact of the fiber optic CPV system.

Aside from the intended use of charging the vehicle, fiber optic solar concentrating systems, like that proposed in this paper, have many additional uses. Auxiliary uses of the fiber optic concentrating system may prove worth consideration as a vehicle may not be under the concentrator at all times. Kandilli and Ulgen (2009) conducted an extensive review of systems of transmission of concentrated solar energy via optical fibers. Auxiliary uses of fiber optic solar concentrating systems include, but are not limited to:

- Fiber optic solar lighting
- Fiber optic based photo-bioreactors for hydrogen generation
- Fiber optic based solar pumped lasers
- Fiber optic solar thermal energy transfer

For studies conducted on fiber optic solar lighting see references: (Han, Riffat et al. 2013), (Oh, Chun et al. 2013), (Ullah and Shin 2014), (Wang, Abdul-Rahman et al. 2010), (Han and Tai Kim 2010), (He, Zheng et al. 2009), (Kandilli, Ulgen et al. 2008), (Mayhoub 2014), and (Sapia 2013).

For studies conducted on fiber optic based photo-bioreactors see references: (Chen, Lee et al. 2006), (Chen, Lee et al. 2006), (Chen, Saratale et al. 2008), (Guo, Zhu et al. 2011), (Liao, Zhong et al. 2014), (Xue, Zhang et al. 2013), (Zhu, Guo et al. 2012), (Zhang, Zhang et al. 2014)

For studies conducted on fiber optic based solar pumped lasers see references: (Kandilli and Ulgen 2009), (Kandilli, Ulgen et al. 2008), (Liang, Fraser Monteiro et al. 1998), (Weksler 1988)

For studies conducted on fiber optic solar thermal energy transfer see references: (Amara, Nordell et al. 2011), (Barlev, Vidu et al. 2011), (Cariou, Dugas et al. 1985), (Kribus, Zik et al. 2000), (Zik, Karni et al. 1999)

APPENDIX A: REGENERATIVE SHOCK ABSORBERS ANALYSIS

The profile of the instantaneous power dissipated by the RF, LR, and RR shocks on a single pass of brushed concrete at 30 mph is provided in Figure 63. The average power dissipated by the RF, LR, and RR shock in a single pass of brushed concrete at 30 mph is 2.74 W, 2.97 W, and 1.65 W, respectively. The average energy dissipated by the RF, LR, and RR shock in a single pass of brushed concrete at 30 mph is 0.0191 Wh, 0.0206 Wh, and 0.0115 Wh, respectively.

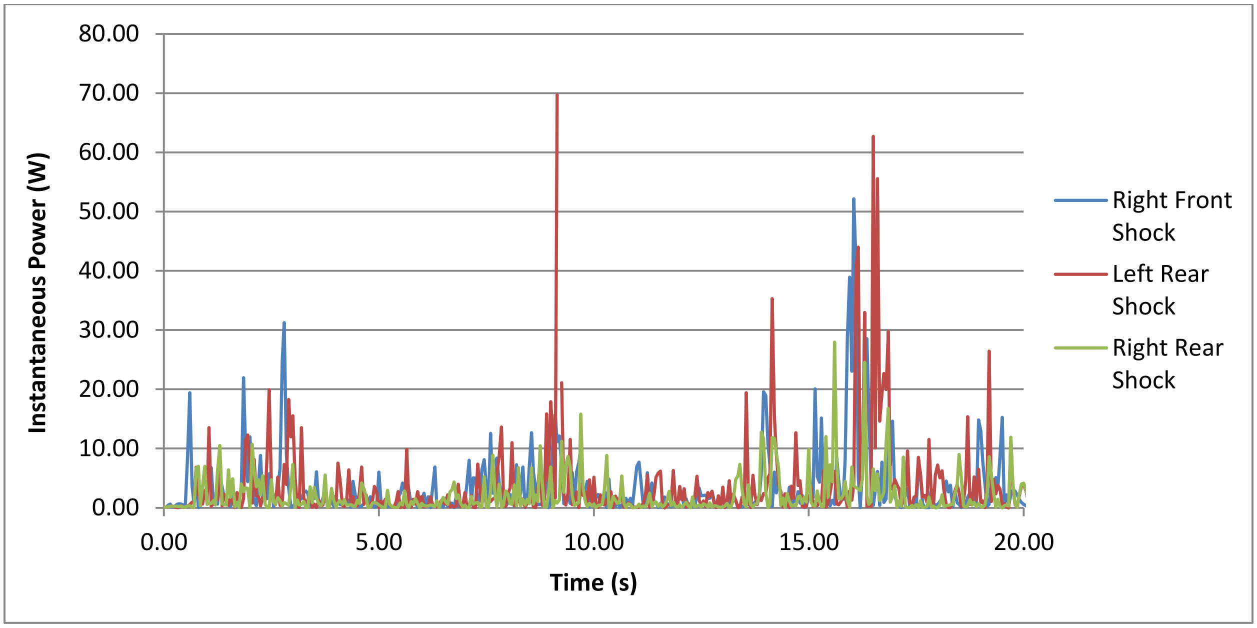

Figure 63. Instantaneous Power Output per Pass for RF, LR, and RR Shock on Brushed Concrete at 30 mph

The profile of the instantaneous power dissipated by the RF, LR, and RR shocks on a single pass of brushed concrete at 50 mph is provided in Figure 64. The average power dissipated by the RF, LR, and RR shock in a single pass of brushed concrete at 50 mph is 9.63

W, 9.83 W, and 6.07 W, respectively. The average energy dissipated by the RF, LR, and RR shock in a single pass of brushed concrete at 50 mph is 0.0403 Wh, 0.0411 Wh, and 0.0254 Wh, respectively.

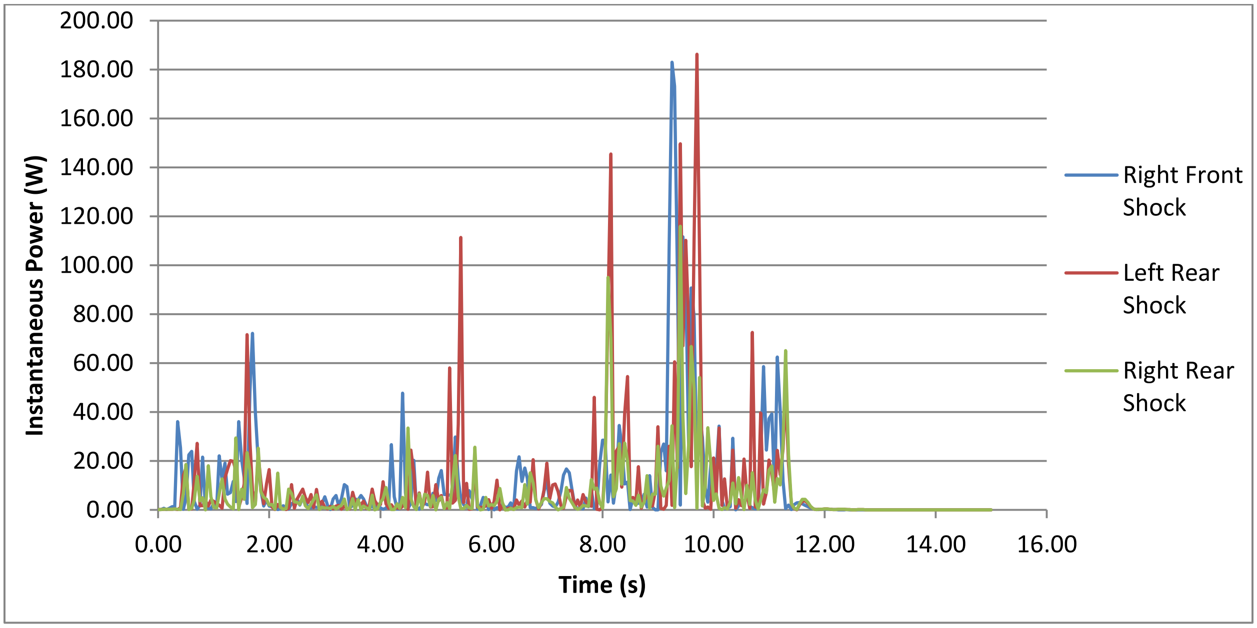

Figure 64. Instantaneous Power Output per Pass for LF, RF, LR, and RR Shock on Brushed Concrete at 50 mph

The profile of the instantaneous power dissipated by the RF, LR, and RR shocks on a single pass of brushed concrete at 70 mph is provided in Figure 65. The average power dissipated by the RF, LR, and RR shock in a single pass of brushed concrete at 70 mph is 19.66 W, 17.37 W, and 12.65 W, respectively. The average energy dissipated by the RF, LR, and RR shock in a single pass of brushed concrete at 70 mph is 0.0603 Wh, 0.0531 Wh, and 0.0388 Wh, respectively.

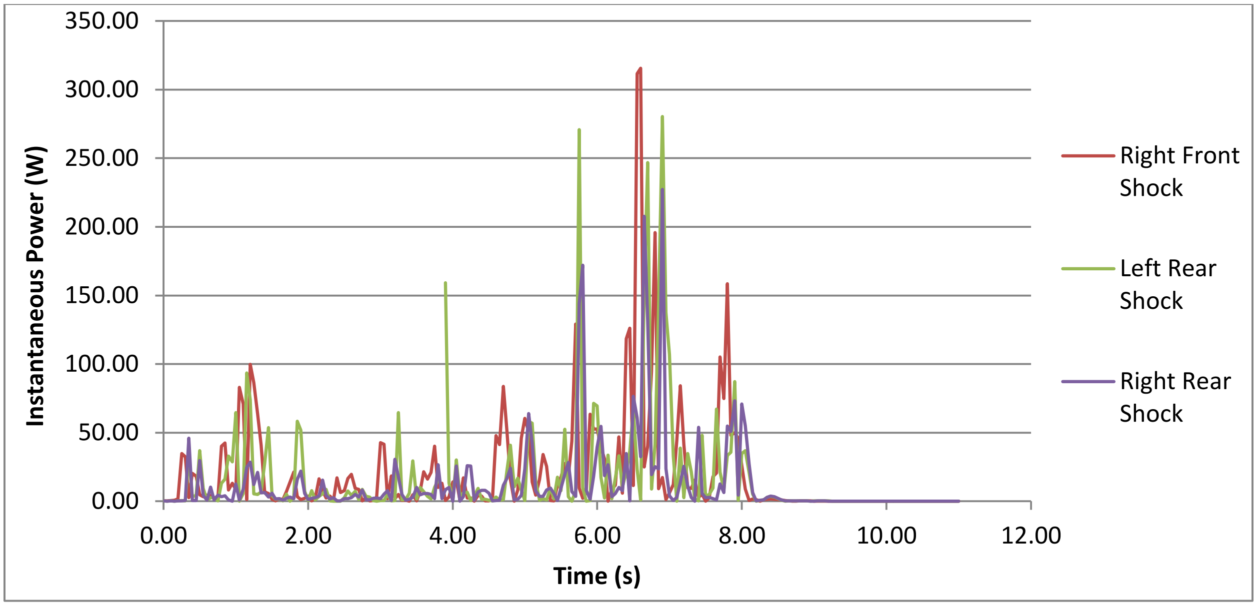

Figure 65. Instantaneous Power Output per Pass for LF, RF, LR, and RR Shock on Brushed Concrete at 70 mph

The profile of the instantaneous power dissipated by the LF, RF, LR, and RR shocks on a single pass of coarse road at 30 mph is provided in Figure 66. The average power dissipated by the LF, RF, LR, and RR shock in a single pass of coarse road at 30 mph is 1.59, 1.33 W, 1.03 W, and 1.06 W, respectively. The average energy dissipated by the LF, RF, LR, and RR shock in a single pass of coarse road at 30 mph is 0.0168 Wh, 0.0141 Wh, 0.0109 Wh, and 1.0112 Wh, respectively.

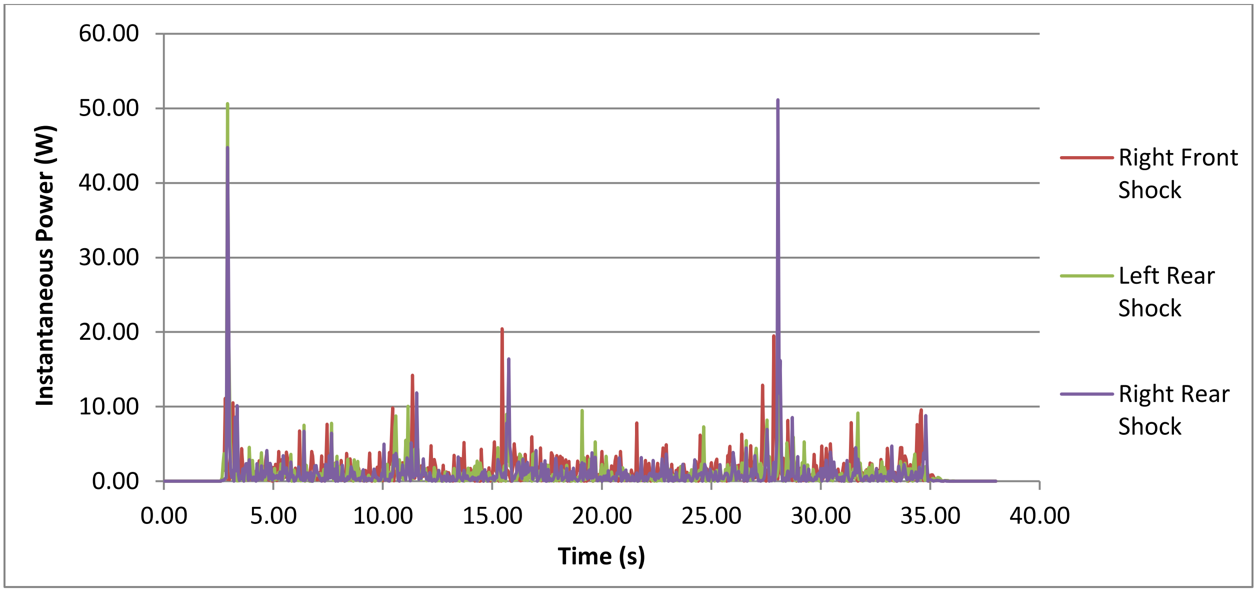

Figure 66. Instantaneous Power Output per Pass for LF, RF, LR, and RR Shock on Coarse Road at 30 mph

The profile of the instantaneous power dissipated by the LF, RF, LR, and RR shocks on a single pass of FEC Road at 50 mph is provided in Figure 67. The average power dissipated by the LF, RF, LR, and RR shock in a single pass of FEC road at 50 mph is 43.17 W, 41.50 W, 34.77 W, and 33.18 W, respectively. The average energy dissipated by the LF, RF, LR, and RR shock in a single pass of FEC road at 50 mph is 0.2884 Wh, 0.2773 Wh, 0.2323 Wh, and 0.2217 Wh, respectively.

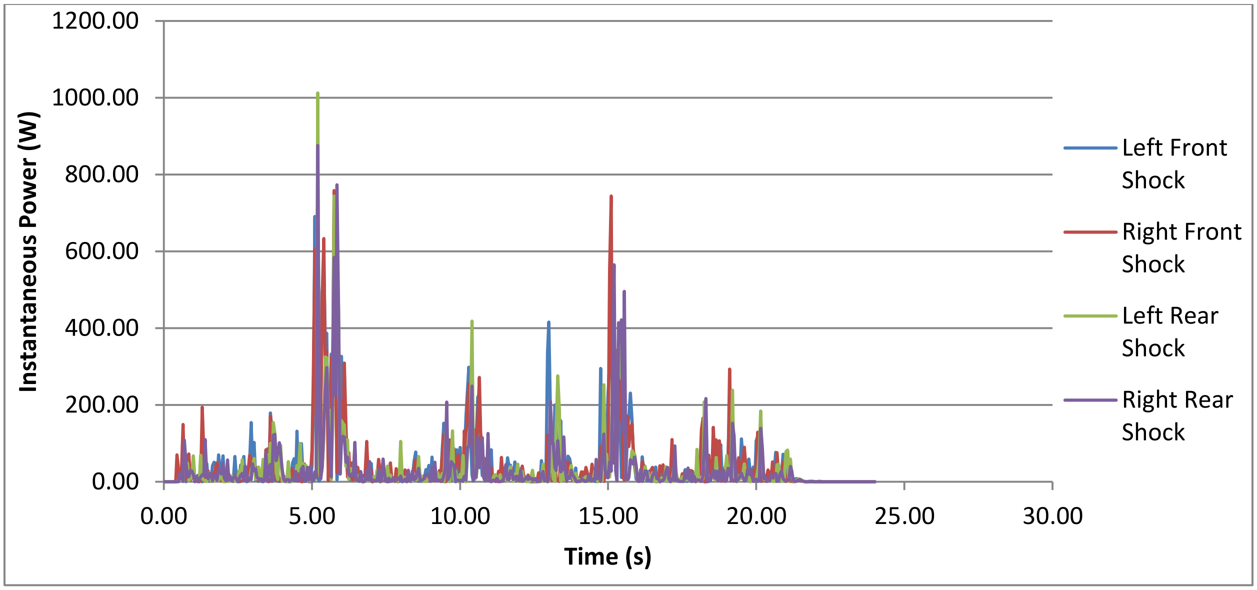

Figure 67. Instantaneous Power Output per Pass for LF, RF, LR, and RR Shock on FEC Road at 50 mph

The profile of the instantaneous power dissipated by the LF, RF, LR, and RR shocks on a single pass of DeSoto road at 40 mph is provided in Figure 68. The average power dissipated by the LF, RF, LR, and RR shock in a single pass of DeSoto road at 40 mph is 28.33 W, 30.25 W, 25.51 W, and 29.41 W, respectively. The average energy dissipated by the LF, RF, LR, and RR shock in a single pass of DeSoto road at 40 mph is 0.2365 Wh, 0.2525 Wh, 0.2130 Wh, and 0.2455 Wh, respectively.

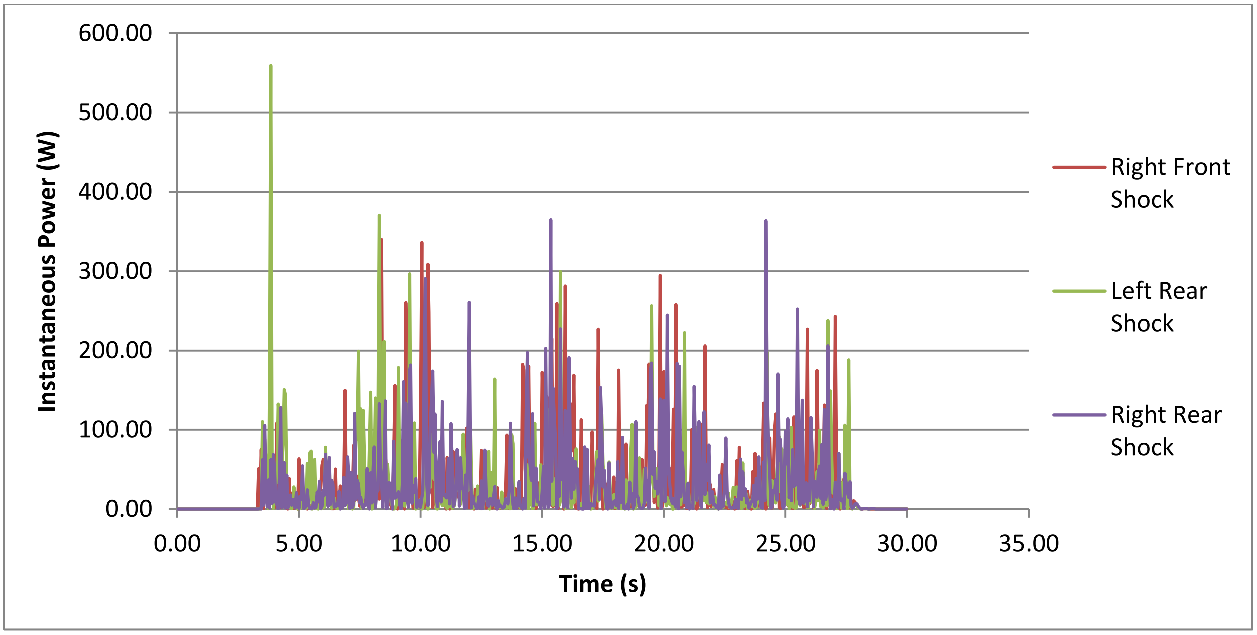

Figure 68. Instantaneous Power Output per Pass for LF, RF, LR, and RR Shock on DeSoto Road at 40 mph

APPENDIX B: ONE SUN TESTING RESULTS

As shown in Figure 69, Figure 70, and Figure 71, for the test conducted with the rear of the vehicle facing west 338.1 Wh, 309.0 Wh, and 340.9 Wh were generated over the period of 9:00 – 16:15 by panels 1, 2, and 3 respectively.

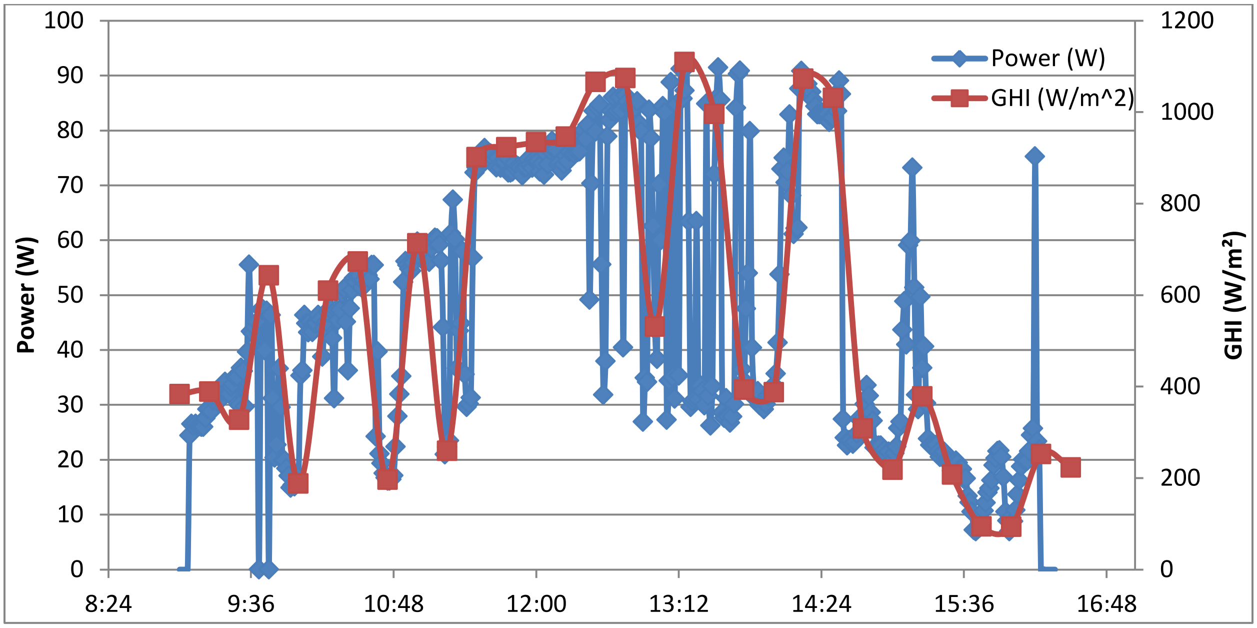

Figure 69. Instantaneous Power and GHI Incident on Panel 1 for Rear of Vehicle Facing West

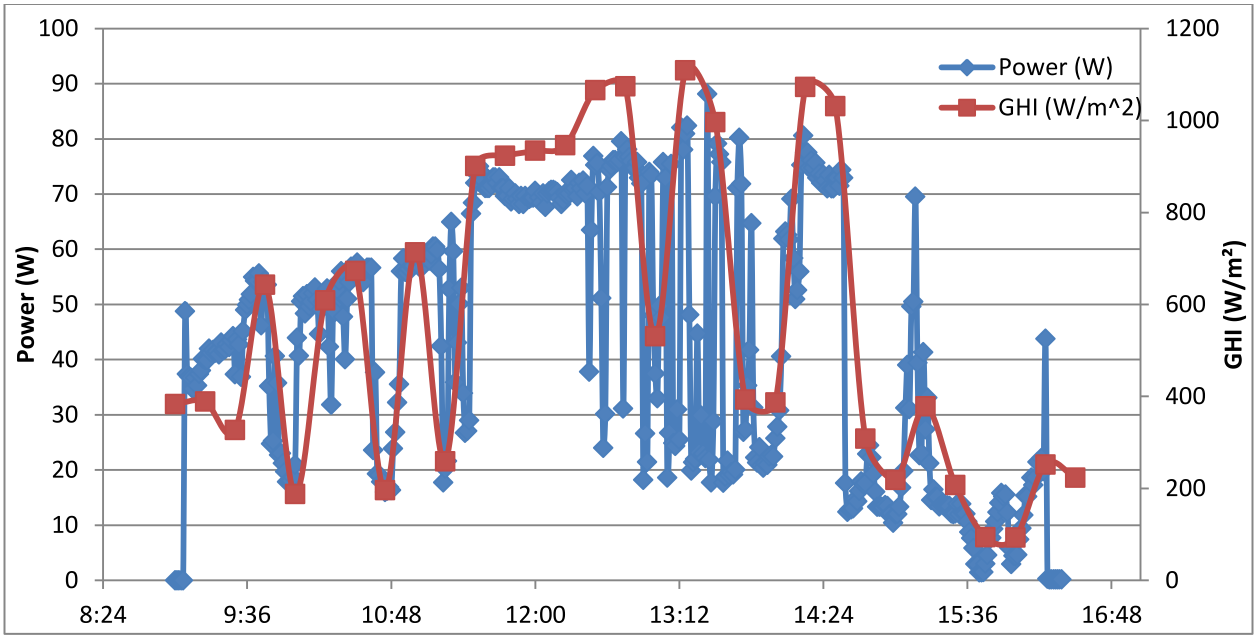

Figure 70. Instantaneous Power and GHI Incident on Panel 2 for Rear of Vehicle Facing West

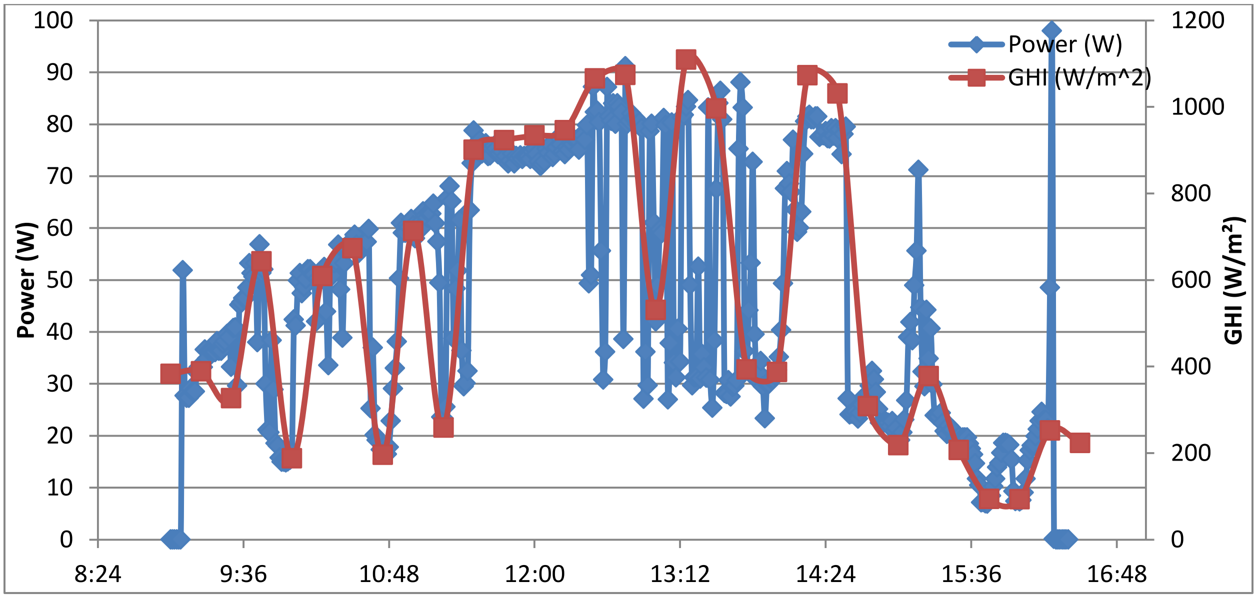

Figure 71. Instantaneous Power and GHI Incident on Panel 3 for Rear of Vehicle Facing West

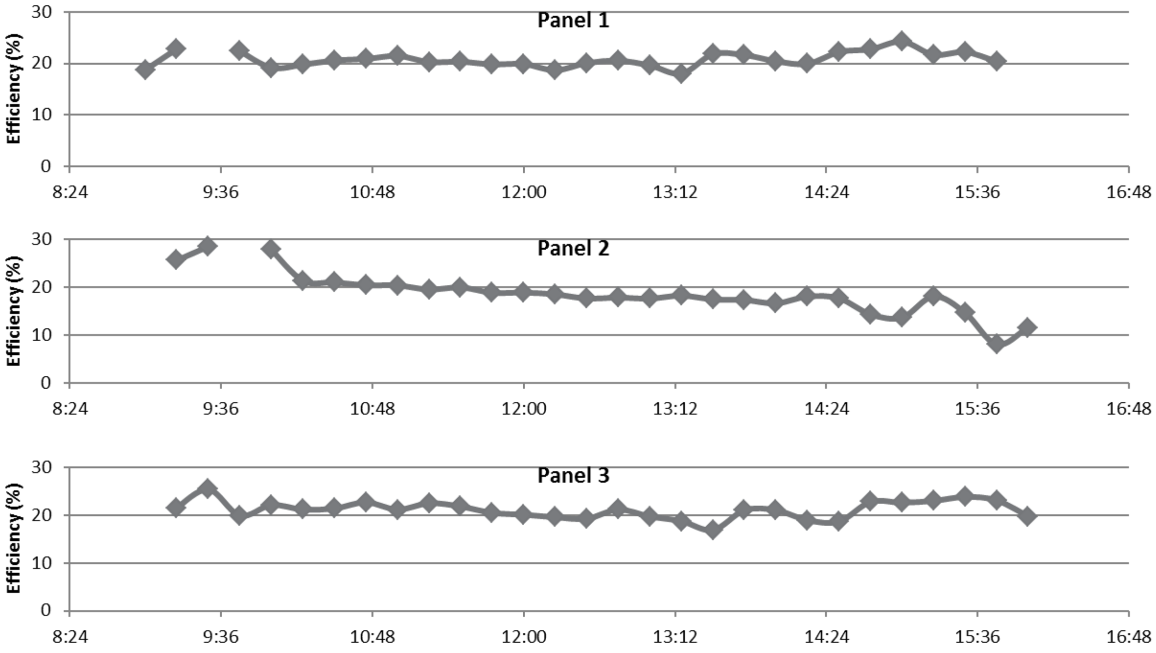

Figure 72. Experimental Panel Efficiencies for Rear of Vehicle Facing West

As previously mentioned, the PV panels are assumed to be horizontal flat plate collectors. In making this assumption, the operating efficiency of the panels can be determined by dividing the instantaneous power at a given time step by the solar power incident on a horizontal flat plate at the same time step. The GHI can be used to determine the solar power incident on a horizontal flat plate by multiplying the GHI by the area of the solar panel in meters squared, or $0.4m^2$. The calculated operating efficiencies for panels 1, 2, and 3 with the rear of the vehicle facing west are plotted in Figure 72.

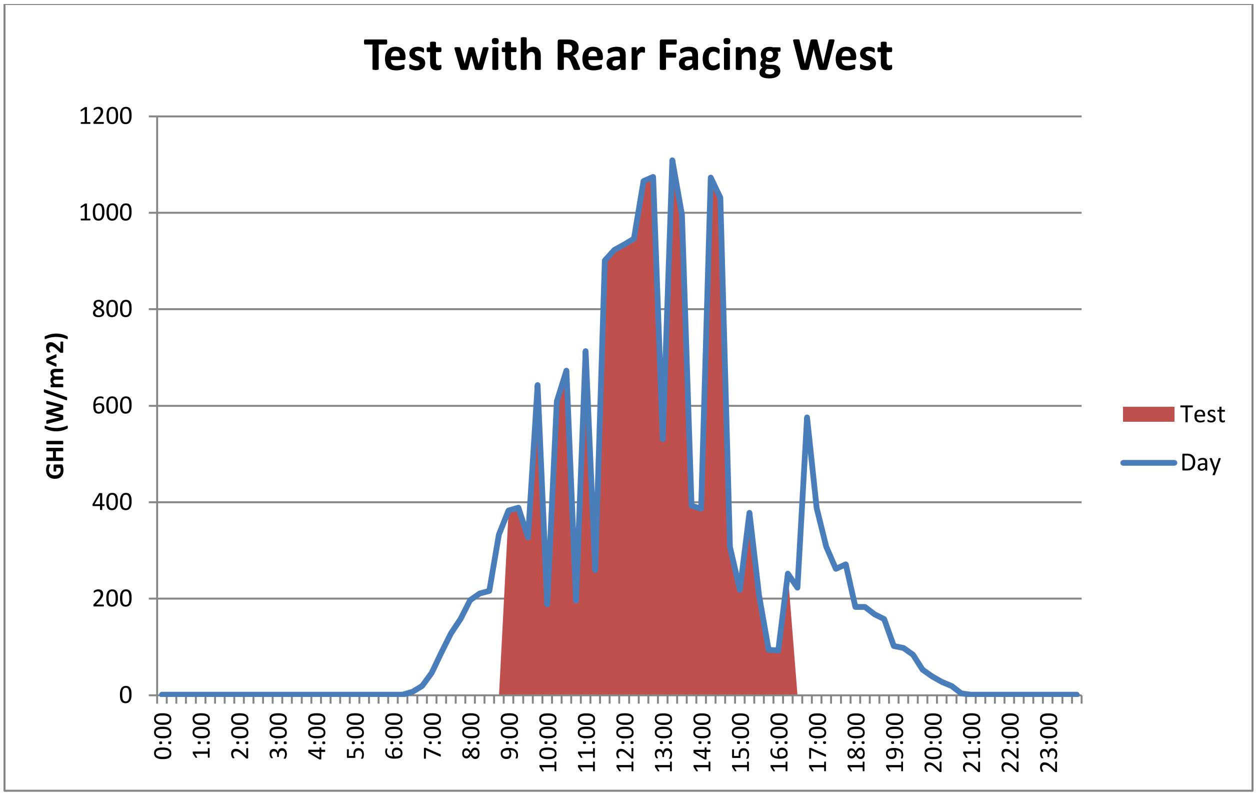

Figure 73. GHI Available During Test with Respect to GHI Available over Entire Day for Rear of Vehicle Facing West

The percentage of the daily insolation available during the test period was determined by comparing the GHI that was available during the test period to the GHI that was available over the entire day. For the test day shown in Figure 73, 79% of the daily insolation was captured during the test period. As discussed in Chapter 5, the energy that could be expected of the PV panel over the entire day is then equal to the actual energy collected by the panel over the test period divided by the percentage of the daily insolation available during the test period.

As shown in Figure 74, Figure 75, Figure 76 for the test conducted with the rear of the vehicle facing east 478.4 Wh, 498.8 Wh, and 499.2 Wh were generated over the period of 9:00 – 17:08 by panels 1, 2, and 3 respectively.

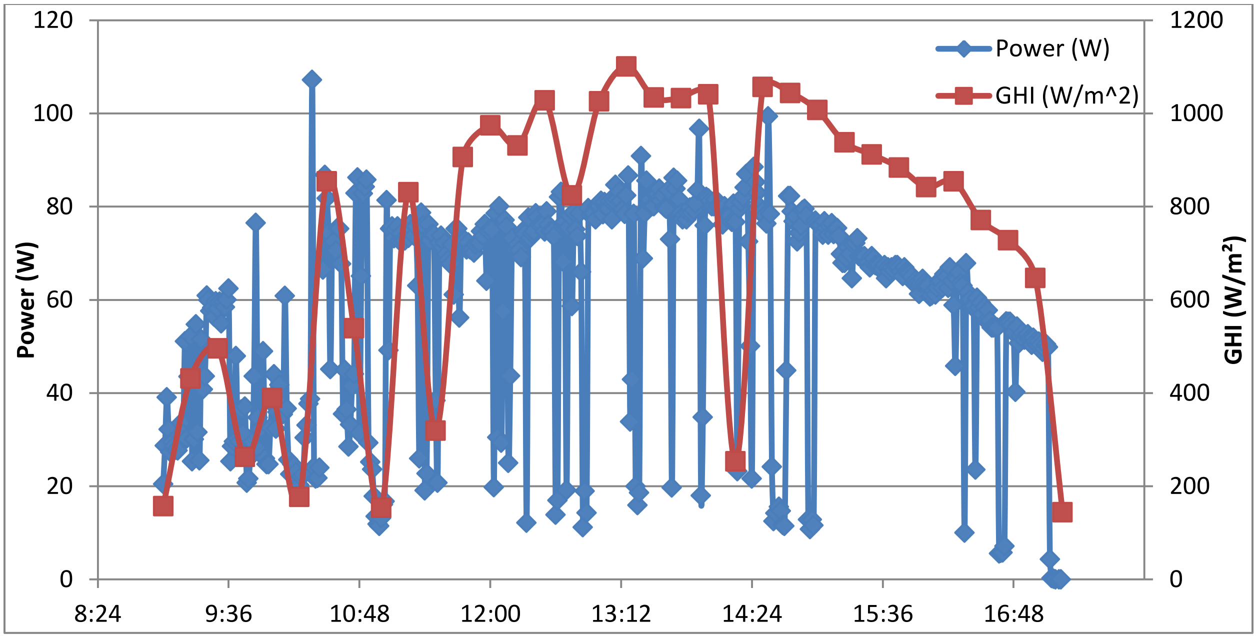

Figure 74. Instantaneous Power and GHI Incident on Panel 1 for Rear of Vehicle Facing East

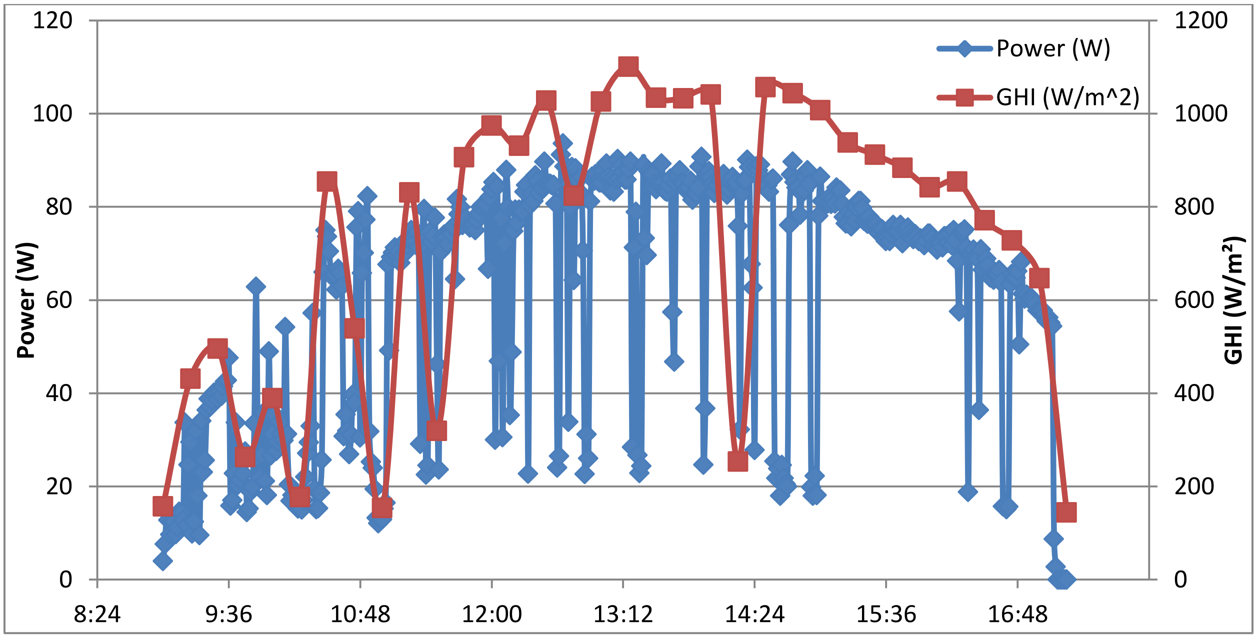

Figure 75. Instantaneous Power and GHI Incident on Panel 2 for Rear of Vehicle Facing East

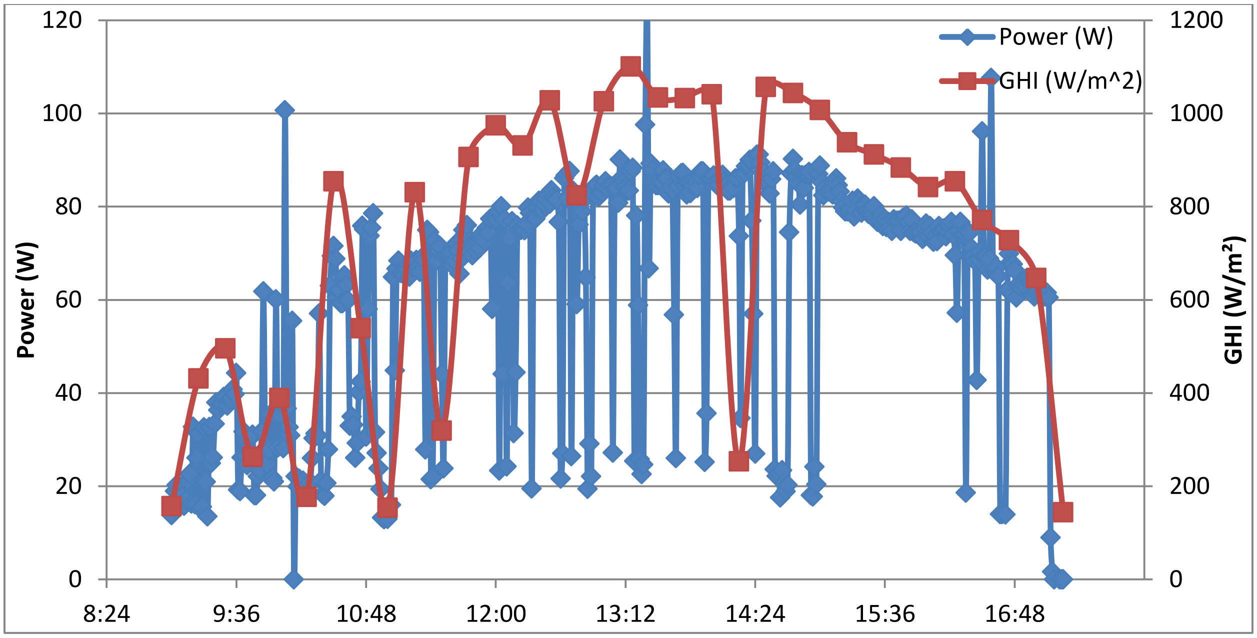

Figure 76. Instantaneous Power and GHI Incident on Panel 3 for Rear of Vehicle Facing East

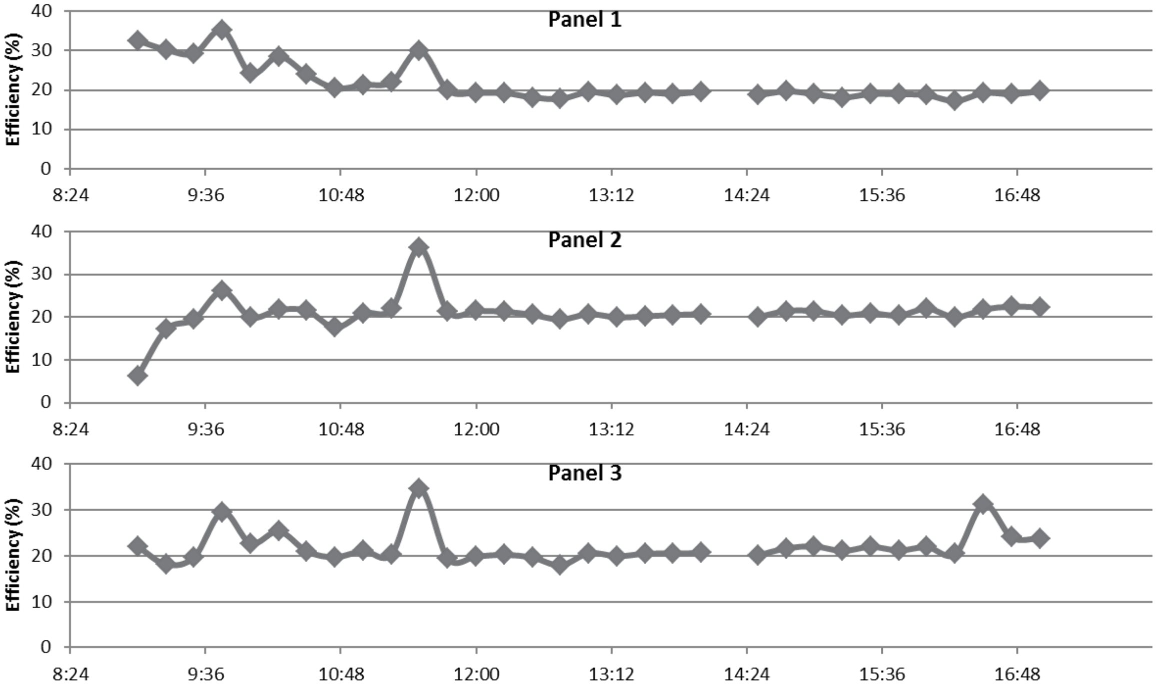

Figure 77. Experimental Panel Efficiencies for Rear of Vehicle Facing East

The operating efficiency of the panels was again determined by dividing the instantaneous power at a given time step by the solar power incident on a horizontal flat plate at the same time step. The calculated operating efficiencies for panels 1, 2, and 3 with the rear of the vehicle facing east are plotted in Figure 77.

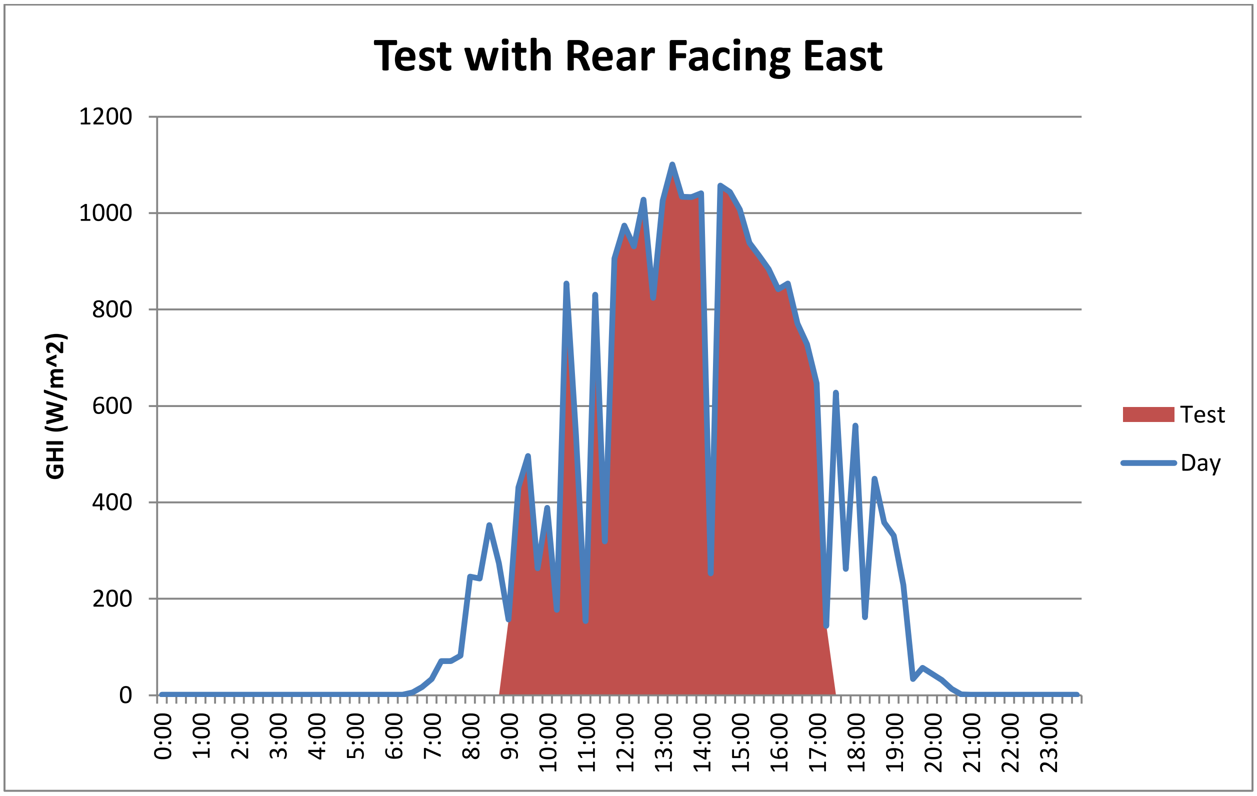

Figure 78. GHI Available During Test with Respect to GHI Available over Entire Day for Rear of Vehicle Facing East

The percentage of the daily insolation available during the test period was determined by comparing the GHI that was available during the test period to the GHI that was available over the entire day. For the test day shown in Figure 78, 84% of the daily insolation was captured during the test period. As discussed in Chapter 5, the energy that could be expected of the PV panel over the entire day is then equal to the actual energy collected by the panel over the test period divided by the percentage of the daily insolation available during the test period.

As shown in Figure 79, Figure 80, and Figure 81 for the test conducted with the rear of the vehicle facing south 325.6 Wh, 343.0 Wh, and 369.8 Wh were generated over the period of 9:00 – 15:45 by panels 1, 2, and 3 respectively.

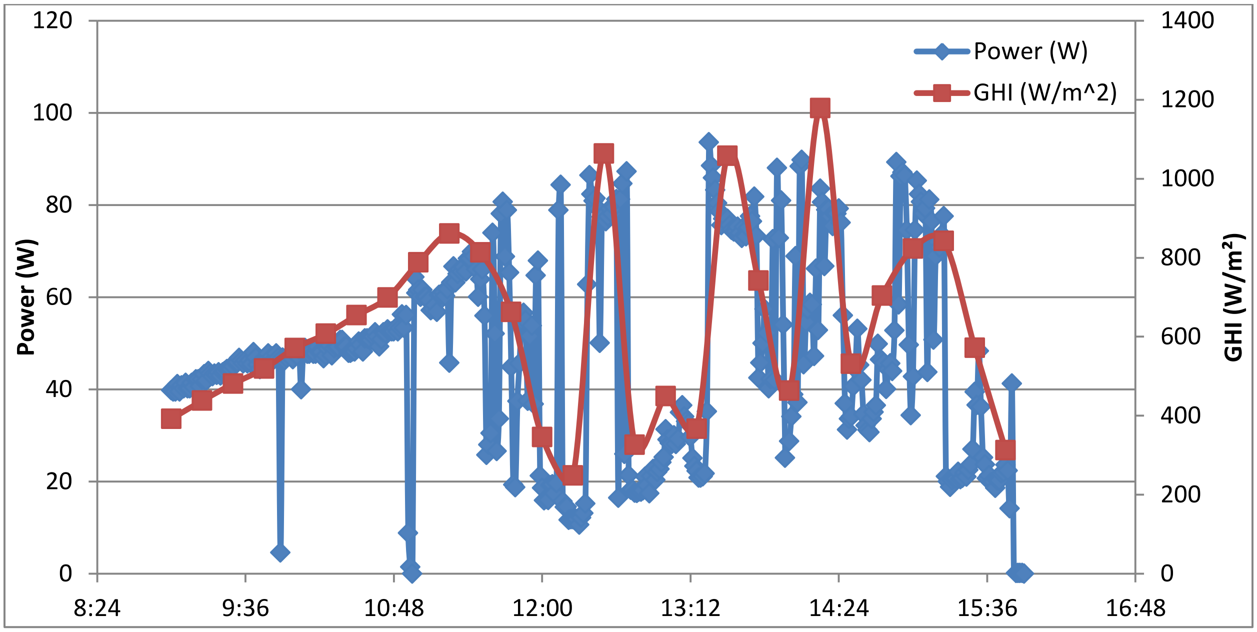

Figure 79. Instantaneous Power and GHI Incident on Panel 1 for Rear of Vehicle Facing South

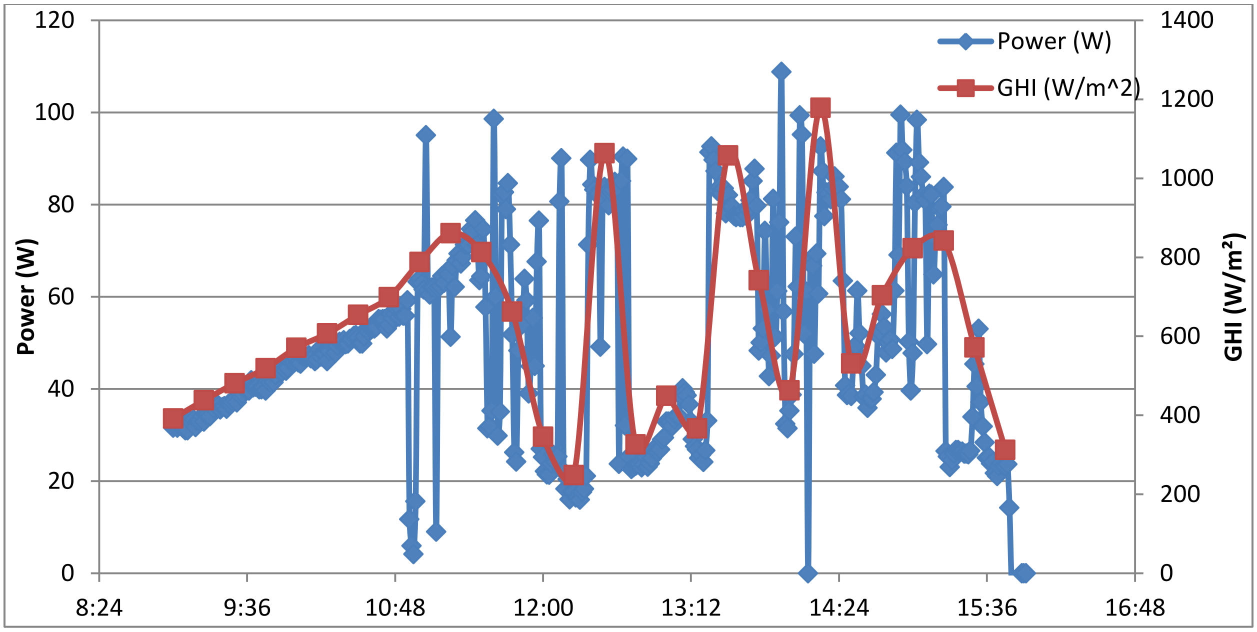

Figure 80. Instantaneous Power and GHI Incident on Panel 2 for Rear of Vehicle Facing South

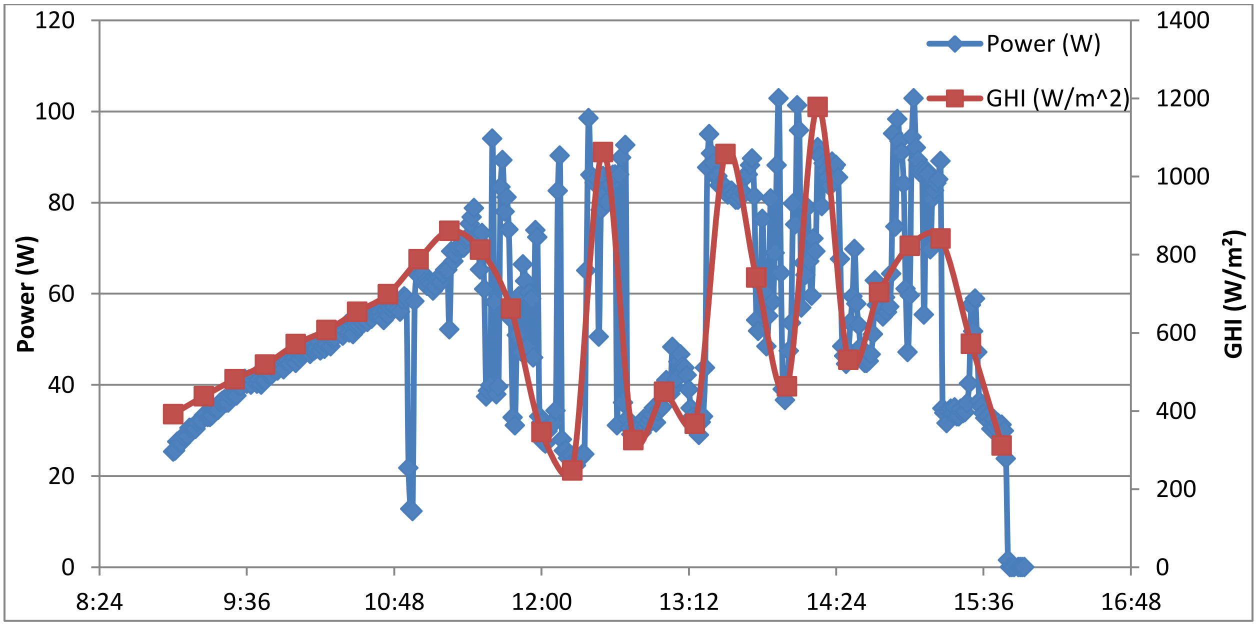

Figure 81. Instantaneous Power and GHI Incident on Panel 3 for Rear of Vehicle Facing South

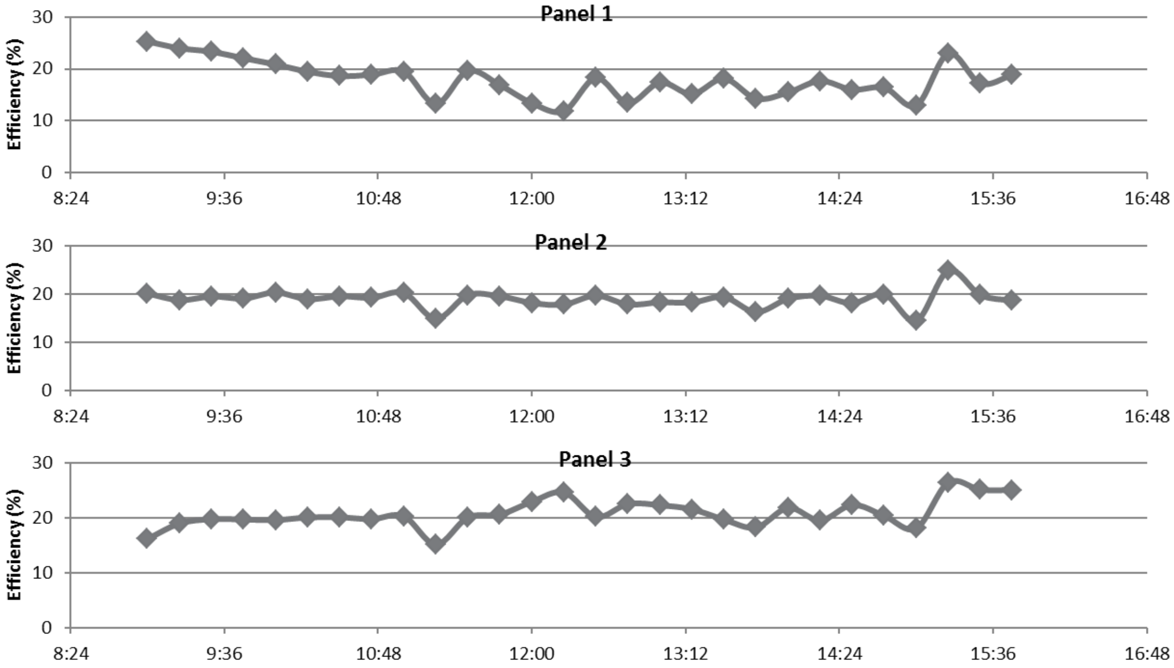

Figure 82. Experimental Panel Efficiencies for Rear of Vehicle Facing South

The operating efficiency of the panels was again determined by dividing the instantaneous power at a given time step by the solar power incident on a horizontal flat plate at the same time step. The calculated operating efficiencies for panels 1, 2, and 3 with the rear of the vehicle facing south are plotted in Figure 82.

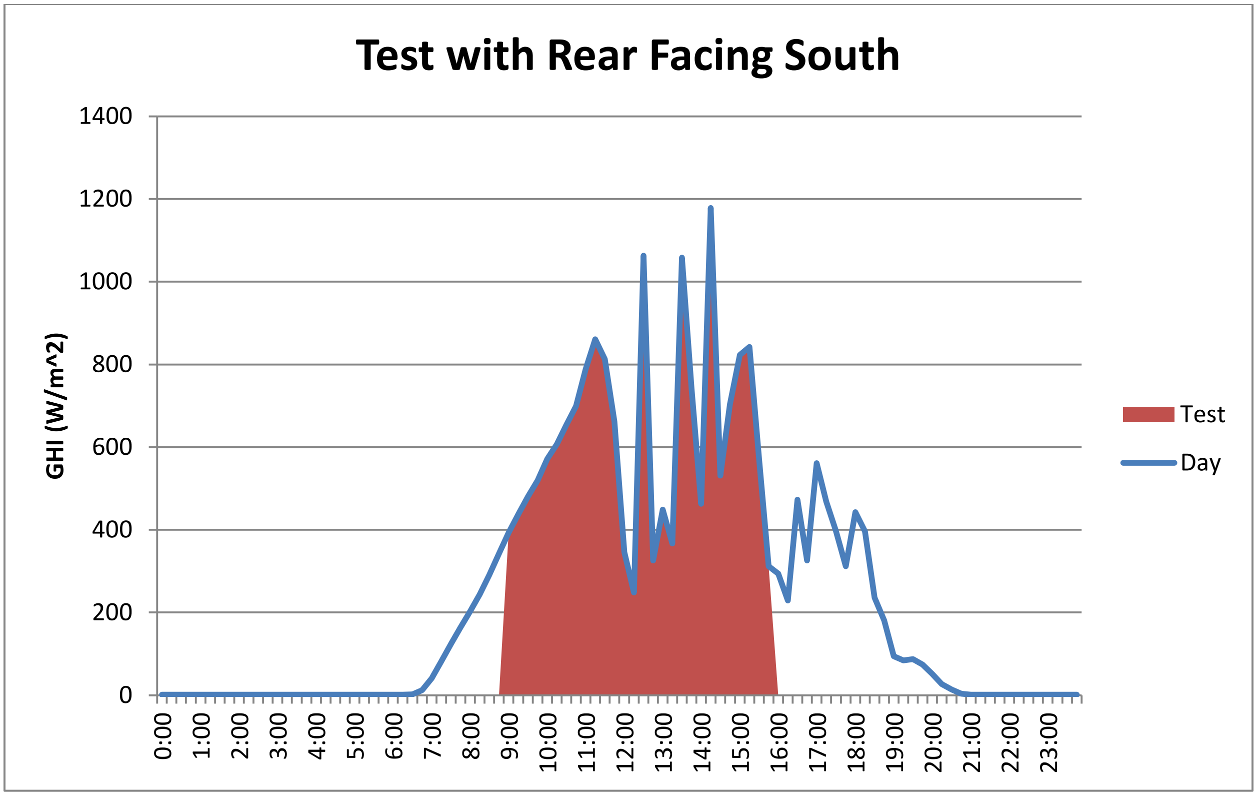

Figure 83. GHI Available During Test with Respect to GHI Available over Entire Day for Rear of Vehicle Facing South

The percentage of the daily insolation available during the test period was determined by comparing the GHI that was available during the test period to the GHI that was available over the entire day. For the test day shown in Figure 83, 74% of the daily insolation was captured during the test period. As discussed in Chapter 5, the energy that could be expected of the PV panel over the entire day is then equal to the actual energy collected by the panel over the test period divided by the percentage of the daily insolation available during the test period.

APPENDIX C: PRELIMINARY TRACKING LENS – STATIC CAR RESULTS

Table 15. Necessary Fresnel Lens Area for Tracking Lens – Static Vehicle Concept when Neglecting Incidence Angle Losses

	Fresnel Lens Array Size (m^2)	
	July	January
Phoenix, AZ	7.0	10.7
Columbia, SC	8.2	22.2
Seattle, WA	8.7	81.2

When the losses incurred due the incidence angle of the concentrated light on the PV material are neglected, the necessary lens area to reach the daily energy goal of 7.6 kWh is largely understated.

REFERENCES

Adinolfi, G., Arsie, I., Di Martino, R., Giustiniani, A., Petrone, G., Rizzo, G., Sorrentino, M. (2008). A Prototype of Hybrid Solar Vehicle: Simulations and On-Board Measurements. International Symposium on Advanced Vehicle Control.

Amara, S., et al. (2011). "Concentration Heating System with Optical Fiber Supply." Energy Procedia **6**(0): 805-814.

Arnaoutakis, G. E., et al. (2013). "Coupling of sunlight into optical fibres and spectral dependence for solar energy applications." Solar Energy **93**(0): 235-243.

Badescu, V. (2008). Modeling Solar Radiation at the Earth's Surface: Recent Advances, Springer.

Baig, H., et al. (2012). "Non-uniform illumination in concentrating solar cells." Renewable and Sustainable Energy Reviews **16**(8): 5890-5909.

Barlev, D., et al. (2011). "Innovation in concentrated solar power." Solar Energy Materials and Solar Cells **95**(10): 2703-2725.

Bauer, S., et al. (2014). "Thermal and energy battery management optimization in electric vehicles using Pontryagin's maximum principle." Journal of Power Sources **246**(0): 808-818.

Bogdan, S. (2014). "Energy-harvesting linear MR damper: prototyping and testing." Smart Materials and Structures **23**(3): 035021.

Boston, D. (2014). Analysis of Charging and Driving Behvior of Plug-in Electric Vehicles Through Telmatics Controller Data. School of Mechanical Engineering, Georgia Institute of Technology. **M.S.M.E.**

Braun, J. E. and J. C. Mitchell (1983). "Solar geometry for fixed and tracking surfaces." Solar Energy **31**(5): 439-444.

Buie, D. and A. G. Monger (2004). "The effect of circumsolar radiation on a solar concentrating system." Solar Energy **76**(1–3): 181-185.

Cariou, J. M., et al. (1985). "Theoretical limits of optical fibre solar furnaces." Solar Energy **34**(4–5): 329-339.

Challenge, W. S. (2014). "Overview." Retrieved 7/28/2014, from http://www.worldsolarchallenge.org/about_wsc_2015/overview.

Chao, C. and L. Wei-Hsin (2012). "A self-sensing magnetorheological damper with power generation." Smart Materials and Structures **21**(2): 025014.

Chávez-Urbiola, E. A., et al. (2012). "Solar hybrid systems with thermoelectric generators." Solar Energy **86**(1): 369-378.

Chen, C.-Y., et al. (2006). "Feasibility study on bioreactor strategies for enhanced photohydrogen production from Rhodopseudomonas palustris WP3-5 using optical-fiber-assisted illumination systems." International Journal of Hydrogen Energy **31**(15): 2345-2355.

Chen, C.-Y., et al. (2006). "Hydrogen production by indigenous photosynthetic bacterium Rhodopseudomonas palustris WP3–5 using optical fiber-illuminating photobioreactors." Biochemical Engineering Journal **32**(1): 33-42.

Chen, C.-Y., et al. (2008). "Phototrophic hydrogen production in photobioreactors coupled with solar-energy-excited optical fibers." International Journal of Hydrogen Energy **33**(23): 6886-6895.

Choi, S. B., et al. (2009). "Vibration control of an electrorheological fluid-based suspension system with an energy regenerative mechanism." Proceedings of the Institution of Mechanical Engineers, Part D: Journal of Automobile Engineering **223**(4): 459-469.

Chow, T. T. (2010). "A review on photovoltaic/thermal hybrid solar technology." Applied Energy **87**(2): 365-379.

Chuan, L. and W. T. Peter (2013). "Fabrication and testing of an energy-harvesting hydraulic damper." Smart Materials and Structures **22**(6): 065024.

Clifford, M. J. and D. Eastwood (2004). "Design of a novel passive solar tracker." Solar Energy **77**(3): 269-280.

Coraggio, G., Rizzo, G., Pisanti, C., and Senatore, A. (2011). Energy Management and Control of a Moving Solar Roof for a Vehicle. 10th International Conference on Engines & Vehicles.

Davis, A. and F. Kühnlenz (2007). "Optical Design using Fresnel Lenses." Optik & Photonik **2**(4): 52-55.

de Podesta, M. (2002). Understanding the Properties of Matter, Taylor & Francis.

Demain, C., et al. (2013). "Evaluation of different models to estimate the global solar radiation on inclined surfaces." Renewable Energy **50**(0): 710-721.

Dib, W., et al. (2014). "Optimal energy management for an electric vehicle in eco-driving applications." Control Engineering Practice **29**(0): 299-307.

DOE (2014). "Solar Foundational Program to Advance Cell Efficiency Round 2." from http://energy.gov/eere/sunshot/solar-foundational-program-advance-cell-efficiency-round-2.

Duvall, M., Knipping, E., Alexander, M. (2007). Environmental Assessment of Plug-in Hybrid Electric Vehicles, Volume 1: Nationwide Greenhouse Gas Emissions, EPRI, Palo Alto, CA. **1**.

EPA (2013, 2/6/2013). "Dynamometer Drive Schedules." 2014, from http://www.epa.gov/nvfel/testing/dynamometer.htm.

Fang, Z., et al. (2013). "Experimental Study of Damping and Energy Regeneration Characteristics of a Hydraulic Electromagnetic Shock Absorber." Advances in Mechanical Engineering **2013**: 9.

Faria, R., et al. (2012). "A sustainability assessment of electric vehicles as a personal mobility system." Energy Conversion and Management **61**(0): 19-30.

Firat, C. and A. Beyene (2012). "Comparison of direct and indirect PV power output using filters, lens, and fiber transport." Energy **41**(1): 271-277.

Florian Ruesch, S. B. (2008). Langzeitalterungsuntersuchung an Abdeckungsmaterialien fuer Thermische Sonnenkollektoren - Ergebnisse einer 20 Jaehrigen Freibewitterungsstudie, Schweizerische Eidgenossenschaft.

Ford (2014, 1/2/2014). "Let the Sun IN: Ford C-Max Solar Energi Concept Goes off the Grid, Gives Glimpse of Clean Vehicle Future." Retrieved 6/11/2014, from http://corporate.ford.com/news-center/press-releases-detail/let-the-sun-in--ford-c-max-solar-energi-concept.

G. Coraggio, C. P., G. Rizzo, A. Senatore (2010). Model Based Control of a Moving Solar Roof for a Solar Vehicle. 10th International Symposium on Advanced Vehicle Control Loughborough, UK Loughborough University Department of Aeronautical & Automotive Engineering & Transport Studies.

Giannouli, M. and P. Yianoulis (2012). "Study on the incorporation of photovoltaic systems as an auxiliary power source for hybrid and electric vehicles." Solar Energy **86**(1): 441-451.

Gunerhan, H. and A. Hepbasli (2007). "Determination of the optimum tilt angle of solar collectors for building applications." Building and Environment **42**(2): 779-783.

Guo, C.-L., et al. (2011). "Enhancement of photo-hydrogen production in a biofilm photobioreactor using optical fiber with additional rough surface." Bioresource Technology **102**(18): 8507-8513.

Han, H. and J. Tai Kim (2010). "Application of high-density daylight for indoor illumination." Energy **35**(6): 2654-2666.

Han, H. J., et al. (2013). "Fiber optic solar lighting: Functional competitiveness and potential." Solar Energy **94**(0): 86-101.

Hannan, M. A., et al. (2012). "Multi-sources model and control algorithm of an energy management system for light electric vehicles." Energy Conversion and Management **62**(0): 123-130.

He, H., et al. (2012). "Comparison study on the battery models used for the energy management of batteries in electric vehicles." Energy Conversion and Management **64**(0): 113-121.

He, K., et al. (2009). "Design and investigation of a novel concentrator used in solar fiber lamp." Solar Energy **83**(11): 2086-2091.

Hou, C., et al. (2014). "Approximate Pontryagin's minimum principle applied to the energy management of plug-in hybrid electric vehicles." Applied Energy **115**(0): 174-189.

Huang, B. J. and F. S. Sun (2007). "Feasibility study of one axis three positions tracking solar PV with low concentration ratio reflector." Energy Conversion and Management **48**(4): 1273-1280.

Huang, K. D., et al. (2005). "Intelligent solar-powered automobile-ventilation system." Applied Energy **80**(2): 141-154.

Kalogirou, S. A. (2014). Chapter 9 - Photovoltaic Systems. Solar Energy Engineering (Second Edition). S. A. Kalogirou. Boston, Academic Press**:** 481-540.

Kandilli, C. and K. Ulgen (2009). "Review and modelling the systems of transmission concentrated solar energy via optical fibres." Renewable and Sustainable Energy Reviews **13**(1): 67-84.

Kandilli, C., et al. (2008). "Exergetic assessment of transmission concentrated solar energy systems via optical fibres for building applications." Energy and Buildings **40**(8): 1505-1512.

Kang-Min, C., et al. (2007). "Feasibility study of an MR damper-based smart passive control system employing an electromagnetic induction device." Smart Materials and Structures **16**(6): 2323.

Keshri, R., et al. (2014). "Integration of a Photovoltaic Panel with an Electric City Car." Electric Power Components and Systems **42**(5): 481-495.

Khattab, N. M. and E. T. El Shenawy (2006). "Optimal operation of thermoelectric cooler driven by solar thermoelectric generator." Energy Conversion and Management **47**(4): 407-426.

Khayyam, H. and A. Bab-Hadiashar (2014). "Adaptive intelligent energy management system of plug-in hybrid electric vehicle." Energy **69**(0): 319-335.

Kraemer, D., et al. (2012). "Modeling and optimization of solar thermoelectric generators for terrestrial applications." Solar Energy **86**(5): 1338-1350.

Kraemer, D., et al. (2011). "High-performance flat-panel solar thermoelectric generators with high thermal concentration." Nat Mater **10**(7): 532-538.

Kribus, A., et al. (2000). "Optical fibers and solar power generation." Solar Energy **68**(5): 405-416.

Kurtz, S. (2012). Opportunities and Challenges for Development of a Mature Concentrating Photovoltaic Power Industry, National Renewable Energy Laboratory.

Lasich, J. B. (2006). Cooling circuit for receiver of solar radiation, Google Patents.

Letendre, S. (2007). Vehicle Integrated PV: Exploring the Potential. 23rd Electric Vehicle Symposium, Anaheim, CA.

Levant (2013). "Why Levant?". 2014, from http://www.levantpower.com/.

Li, C., et al. (2014). "Integration of shock absorption and energy harvesting using a hydraulic rectifier." Journal of Sound and Vibration **333**(17): 3904-3916.

Liang, D., et al. (1998). "Fiber-optic solar energy transmission and concentration." Solar Energy Materials and Solar Cells **54**(1–4): 323-331.

Liao, Q., et al. (2014). "High-performance biofilm photobioreactor based on a GeO2–SiO2–chitosan-medium-coated hollow optical fiber." International Journal of Hydrogen Energy **39**(19): 10016-10027.

Lipman, T. E. and M. A. Delucchi (2010). CHAPTER FIVE - Expected Greenhouse Gas Emission Reductions by Battery, Fuel Cell, and Plug-In Hybrid Electric Vehicles. Electric and Hybrid Vehicles. G. Pistoia. Amsterdam, Elsevier**:** 113-158.

Mayhoub, M. S. (2014). "Innovative daylighting systems' challenges: A critical study." Energy and Buildings **80**(0): 394-405.

Mezrhab, A. and M. Bouzidi (2006). "Computation of thermal comfort inside a passenger car compartment." Applied Thermal Engineering **26**(14–15): 1697-1704.

Miller, D. C., Kempe, M.D., Kennedy, C.E., Kurtz, S.R. (2009). Analysis of Transmitted Optical Spectrum Enabling Accelerated Testing of CPV Designs. Society of Photographic Instrumentation Engineers 2009 Solar Energy and Technology Conference. San Diego, California, National Renewable Energy Laboratory.

Miller, D. C. and S. R. Kurtz (2011). "Durability of Fresnel lenses: A review specific to the concentrating photovoltaic application." Solar Energy Materials and Solar Cells **95**(8): 2037-2068.

Morcos, V. H. (1994). "Optimum tilt angle and orientation for solar collectors in Assiut, Egypt." Renewable Energy **4**(3): 291-298.

Nakamura, T., Smith, B. (2011). Solar Thermal System for Lunar ISRU Applications: Development and Field Operation at Mauna Kea, HI, American Institute of Aeronautics and Astronautics.

NAP (2010). Transitions to Alternative Transportation Technologies--Plug-in Hybrid Electric Vehicles, The National Academies Press.

Neubauer, J., et al. (2013). "Sensitivity of plug-in hybrid electric vehicle economics to drive patterns, electric range, energy management, and charge strategies." Journal of Power Sources **236**(0): 357-364.

NREL (1992). Solar Radiation Data Manual for Flat-Plate and Concentrating Collectors.

Nüesch, T., et al. (2014). "Optimal energy management for a diesel hybrid electric vehicle considering transient PM and quasi-static NOx emissions." Control Engineering Practice **29**(0): 266-276.

NuonSolarTeam (2014). "Nuna7." Retrieved 6/9/2014, from http://www.nuonsolarteam.nl/nuna/?lang=en#body-copy.

Oh, S. J., et al. (2013). "Computational analysis on the enhancement of daylight penetration into dimly lit spaces: Light tube vs. fiber optic dish concentrator." Building and Environment **59**(0): 261-274.

P.J. Verlinden, A. T., D.D. Smith, K. McIntosh, R.M. Swanson, G. Ganakas, J.B Lasich (2001). Will we have a 20%-efficient (PTC) photovoltaic system? 17th European Photovoltaic Solar Energy Conference.

Payri, F., et al. (2014). "A stochastic method for the energy management in hybrid electric vehicles." Control Engineering Practice **29**(0): 257-265.

Prakash, G. and H. P. Garg (2000). Solar Energy: Fundamentals and Applications, Tata McGraw-Hill Publishing Company.

Rainhart, L. G. and W. P. Schimmel Jr (1975). "Effect of outdoor aging on acrylic sheet." Solar Energy **17**(4): 259-264.

Rizzo, G., Pisanti, C., Coraggio, G., (2010). Applications of Solar Energy to Cars: Perspectives and Problems. SAE-NA.

Rizzo, G., Pisanti, C., Coraggio, G., (2013). Design, Development, and Control of a Self-Tracking Photovoltaic Roof for a Road Vehicle. 11th International Conference on Engines & Vehicles.

Rockendorf, G., et al. (1999). "PV-hybrid and thermoelectric collectors." Solar Energy **67**(4–6): 227-237.

Royne, A., et al. (2005). "Cooling of photovoltaic cells under concentrated illumination: a critical review." Solar Energy Materials and Solar Cells **86**(4): 451-483.

Samaras, C. and K. Meisterling (2008). "Life Cycle Assessment of Greenhouse Gas Emissions from Plug-in Hybrid Vehicles: Implications for Policy." Environmental Science & Technology **42**(9): 3170-3176.

Sapia, C. (2013). "Daylighting in buildings: Developments of sunlight addressing by optical fiber." Solar Energy **89**(0): 113-121.

Sciarretta, A., et al. (2014). "A control benchmark on the energy management of a plug-in hybrid electric vehicle." Control Engineering Practice **29**(0): 287-298.

Shams-Zahraei, M., et al. (2012). "Integrated thermal and energy management of plug-in hybrid electric vehicles." Journal of Power Sources **216**(0): 237-248.

Singh, G. K. (2013). "Solar power generation by PV (photovoltaic) technology: A review." Energy **53**(0): 1-13.

Singh, K. B., et al. (2012). "Piezoelectric vibration energy harvesting system with an adaptive frequency tuning mechanism for intelligent tires." Mechatronics **22**(7): 970-988.

Sousa, T., et al. (2014). "A hybrid simulated annealing approach to handle energy resource management considering an intensive use of electric vehicles." Energy **67**(0): 81-96.

Stanciu, C. and D. Stanciu (2014). "Optimum tilt angle for flat plate collectors all over the World – A declination dependence formula and comparisons of three solar radiation models." Energy Conversion and Management **81**(0): 133-143.

Tang, R. and T. Wu (2004). "Optimal tilt-angles for solar collectors used in China." Applied Energy **79**(3): 239-248.

Torres, J. L., et al. (2014). "Energy management strategy for plug-in hybrid electric vehicles. A comparative study." Applied Energy **113**(0): 816-824.

Tribioli, L., et al. (2014). "A Real Time Energy Management Strategy for Plug-in Hybrid Electric Vehicles based on Optimal Control Theory." Energy Procedia **45**(0): 949-958.

Trovão, J. P., et al. (2013). "A multi-level energy management system for multi-source electric vehicles – An integrated rule-based meta-heuristic approach." Applied Energy **105**(0): 304-318.

U.S.E.I.A. (2013, May 9, 2013). "What is the U.S. Electricity Generation by Energy Source." Retrieved 6/11/2014, from http://www.eia.gov/tools/faqs/faq.cfm?id=427&t=3.

Ullah, I. and S. Shin (2014). "Highly concentrated optical fiber-based daylighting systems for multi-floor office buildings." Energy and Buildings **72**(0): 246-261.

Verlinden, P., et al. (1991). Single-wafer integrated 140 W silicon concentrator module. Photovoltaic Specialists Conference, 1991., Conference Record of the Twenty Second IEEE.

Wang, C., et al. (2010). "Daylighting can be fluorescent: Development of a fiber solar concentrator and test for its indoor illumination." Energy and Buildings **42**(5): 717-727.

Wang, N., et al. (2011). "A novel high-performance photovoltaic-thermoelectric hybrid device." Energy & Environmental Science **4**(9): 3676-3679.

Weksler, M., Shwartz, J. (1988). "Solar-Pumped Solid-State Lasers." IEEE Journal of Quantum Electronics **24**(6).

Wilcox, S., Marion, W. (2008). Users Manual for TMY3 Data Sets, National Renewable Energy Laboratory.

Xie, W. T., et al. (2011). "Concentrated solar energy applications using Fresnel lenses: A review." Renewable and Sustainable Energy Reviews **15**(6): 2588-2606.

Xue, S., et al. (2013). "A novel photobioreactor structure using optical fibers as inner light source to fulfill flashing light effects of microalgae." Bioresource Technology **138**(0): 141-147.

Zhang, C., et al. (2014). "Effects of mass transfer and light intensity on substrate biological degradation by immobilized photosynthetic bacteria within an annular fiber-illuminating biofilm reactor." Journal of Photochemistry and Photobiology B: Biology **131**(0): 113-119.

Zhang, G., et al. (2012). "Design of active and energy-regenerative controllers for DC-motor-based suspension." Mechatronics **22**(8): 1124-1134.

Zhongjie, L., et al. (2013). "Energy-harvesting shock absorber with a mechanical motion rectifier." Smart Materials and Structures **22**(2): 025008.

Zhu, X., et al. (2012). "A feasibility study on unsaturated flow bioreactor using optical fiber illumination for photo-hydrogen production." International Journal of Hydrogen Energy **37**(20): 15666-15671.

Zik, O., et al. (1999). "The TROF (tower reflector with optical fibers): a new degree of freedom for solar energy systems." Solar Energy **67**(1–3): 13-22.